CFD based optimization of the aerodynamics of a low-fuel-consumption vehicle

Diploma thesis

by

Christoph Simon Feichtinger

Submitted to

Graz University of Technology
Faculty for Mechanical Engineering and Economics

for receiving the academic degree

Diplomingenieur

Supervised by

Ao.Univ.-Prof. Dipl.-Ing. Dr.techn. Helfried Steiner - Institute of Fluid Mechanics and Heat Transfer, TU Graz
Ass.Prof. Dipl.-Ing. Dr.techn. Walter Meile - Institute of Fluid Mechanics and Heat Transfer, TU Graz
Dipl.-Ing. (FH) Gernot Herschold Pließnig - qpunkt GmbH

Graz, November 2010

Beschluss der Curricula-Kommission für Bachelor-, Master- und Diplomstudien vom 10.11.2008
Genehmigung des Senates am 1.12.2008

Englische Fassung:

STATUTORY DECLARATION

I declare that I have authored this thesis independently, that I have not used other than the declared sources / resources, and that I have explicitly marked all material which has been quoted either literally or by content from the used sources:

………………………… ……………………………………………..
date (signature)

Deutsche Fassung:

EIDESSTATTLICHE ERKLÄRUNG

Ich erkläre an Eides statt, dass ich die vorliegende Arbeit selbstständig verfasst, andere als die angegebenen Quellen/Hilfsmittel nicht benutzt, und die den benutzten Quellen wörtlich und inhaltlich entnommene Stellen als solche kenntlich gemacht habe.

Graz, am ………………………… ……………………………………………..
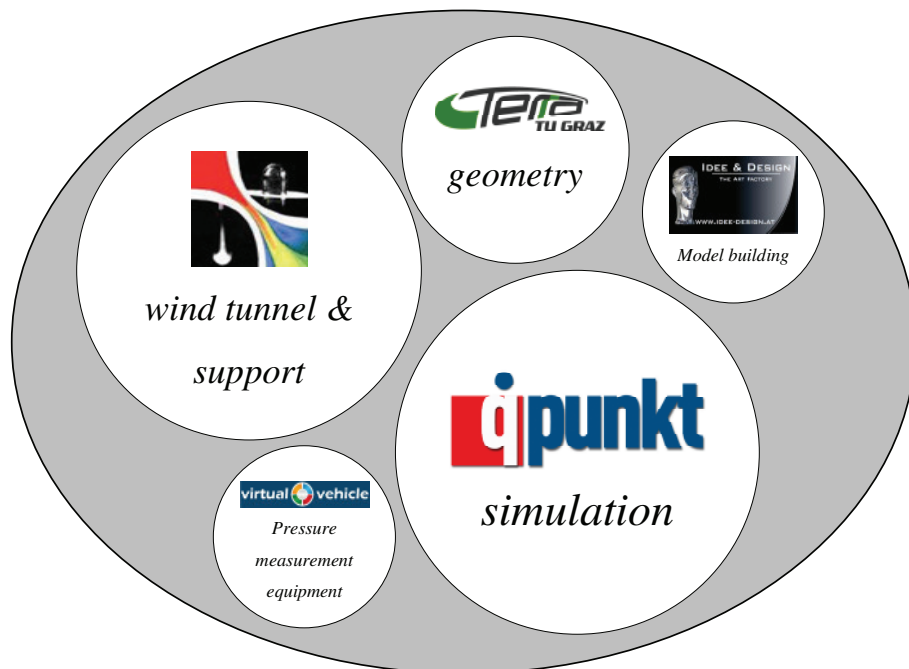(Unterschrift)

To my parents, mentors and friends

involved companies and institutions

Abstract

The present diploma thesis investigates the predictive capability of modern CFD methods for simulating the flow around low drag bodies. The considered test body was the TERA Fennek low-fuel-consumption vehicle developed by the Team Eco Racing Austria from Graz University of Technology.

The first part of the work was devoted to wind tunnel experiments to provide data for comparison against the numerical results. After the design and installation of the experimental setup in the wind tunnel of the Institute of Fluid Mechanics and Heat Transfer of the TU Graz, a series of measurements was carried out for varying the magnitude as well as the angle of the incident velocity. The measured force and moment coefficients showed in general a strong dependence on the incident flow angle as the effect of flow separation becomes significant on the downwind side of the test body.

In the numerical simulations two turbulence models were tested. The steady RANS model SST-k-ω was applied to all considered cases with varying the incident flow angle. The hybrid unstationary approach of a Detached Eddy Simulation (DES) was applied only to the cases with zero and the maximum considered flow angles, $\alpha=0°$, and $\alpha=25°$, respectively, due to the high computational costs of this method. The predictions of the SST-k-ω agree fairly well with the experiments for the lower incident flow angles. The sharp increase in the experimentally measured total drag for α going beyond $10°$ was also well reproduced by the simulations. Notable deviations occur, however, for the highest considered value $\alpha=25°$. The DES produces for $\alpha=0°$ essentially the same results as the SST-k-ω. For $\alpha=25°$, the DES describes more realistically the unsteady motion in the separated wake flow region, which leads to improved predictions for the pressure distribution on the downwind side of the body. The predictions for the total force and moment coefficients show still a notable disagreement to the experiments, so that the high computational costs of DES can be hardly justified.

The usefulness of CFD for a detailed aerodynamic flow analysis is finally demonstrated for the considered geometry. The CFD-based analysis can identify the most critical parts of the contour, which may be very helpful for a further aerodynamical shape optimization.

Kurzfassung

Die vorliegende Diplomarbeit beschäftigt sich mit der Evaluierung von CFD Methoden zur Berechnung von Körpern mit geringem Strömungswiderstand. Als Versuchskörper dazu diente das Fahrzeug des Team Eco Racing Austria der Technischen Universität Graz aus dem Jahre 2010.

Der erste Teil der Diplomarbeit beschäftigt sich mit Windkanalmessungen, um Daten für den Vergleich mit den numerischen Ergebnissen zu bekommen. Die Messungen wurden im Windkanal am Institut für Strömungslehre und Wärmeübertragung der TU Graz durchgeführt. In umfangreichen Messserien wurden die auf den Testkörper wirkenden Kräfte und Momente, sowie der an bestimmten Punkten der Körperoberfläche herrschende statische Druck bei unterschiedlichen Strömungsgeschwindigkeiten und Anströmwinkeln gemessen. Die gemessenen Kräfte und Momente zeigen generell eine starke Abhängigkeit vom Anströmwinkel, was auf den starken Einfluss der bei höheren Anstellwinkeln auf der Leeseite des Körpers auftretenden Strömungsablösungen zurückzuführen ist.

Für die Durchführung der numerischen Simulation wurden zwei verschiedene Modelle zur Turbulenzmodellierung gewählt. Das stationäre RANS Model SST-k-ω wurde für alle untersuchten Testfälle verwendet. Das instationäre Hybrid-Modell „Detached Eddy Simulation" (DES) wurde hingegen aufgrund dessen enorm hohen Rechenaufwandes nur für Geradanströmung, sowie für den größten untersuchten Anstellwinkel $\alpha=25°$ verwendet. Die Ergebnisse der SST-k-ω Simulation stimmen für kleine Anstellwinkel sehr gut mit den Messungen überein. Insbesondere wird der starke Anstieg des Widerstandsbeiwertes für Anstellwinkel größer 10° vom SST-k-ω Modell gut abgebildet. Erst für den größten untersuchten Anstellwinkel von $\alpha=25°$ weichen die Ergebnisse der SST-k-ω Simulation stark von den Messwerten ab. Die für diesen grundsätzlich herausfordernsten Fall ebenso durchgeführte instationäre DES Simulation konnte die abgelöste Strömung im hinteren Bereich des Testkörpers für diesen Anstellwinkel erwartungsgemäß realistischer abbilden, wie aus dem Vergleich mit den lokal gemessenen Druckbeiwerten hervorging. Die vorhergesagten absoluten Kraft- und Momentenbeiwerte weichen jedoch auch bei der DES Simulation beträchtlich von den Messungen ab, weshalb die Zweckmäßigkeit einer teuren und aufwändigen DES Simulation in Frage gestellt werden muss.

Der Nutzen einer CFD Simulation für eine detaillierte Analyse der Aerodynamik eines betrachteten Körpers wird im abschließenden Teil der Arbeit anhand der untersuchten Geometrie aufgezeigt. Mittels CFD Methoden ist es insbesondere möglich, jene kritischen Gebiete und Schwachstellen am Strömungskörper ausfindig zu machen, wo der Großteil des Luftwiderstandes generiert wird. Auf Grundlage dieser Detektion von Schwachstellen können Maßnahmen abgeleitet werden, die zu einer aerodynamischen Verbesserung der Körperform beitragen.

Table of Contents

List of Symbols

Latin symbols:

a_1	Model constant	[-]
A	Lift force	[N]
A_D	Cross section at the nozzle outlet	[m²]
A_{DVK}	Cross section of the nozzle pre chamber of the wind tunnel	[m²]
A_f	Surrounding of a computational cell	[m²]
$A_{proj.}$	Frontal area of the vehicle	[m²]
c_A	Lift force coefficient	[-]
c_f	Skin friction coefficient	[-]
c_g	Yaw moment coefficient	[-]
c_n	Pitch moment coefficient	[-]
c_p	Pressure coefficient	[-]
c_r	Roll moment coefficient	[-]
c_S	Side force coefficient	[-]
c_W	Drag force coefficient	[-]
C_{DES}	Calibration constant	[-]
CFL	Courant-Friedrich-Levy number	[-]
C_μ	Model constant	[-]
dF	Infinitesimal surface element	[m²]
D_ω^+	Positive portion of the cross diffusion term	[N/m⁴]
E_k	Dissipation of turbulent kinetic energy	[N/m²s]
$\tilde{E}_k$	Modified term of dissipation of turbulent kinetic energy	[N/m²s]
E_ω	Dissipation of turbulent dissipation	[N/m⁴]
f	Eddy separation frequency	[1/s]
f_i	Body force	[m/s²]
F_{DES}	Model constant	[-]
$F_w, F_{av}, F_{ar}, F_{al}, F_{sv}, F_{sh}$	Measured forces of the wind tunnel balance	[N]
F_1, F_2	Blending functions	[-]
g	Acceleration of gravity	[m/s²]

h	Effective depth	[m]
k	Turbulent kinetic energy	[m²/s²]
k_s	Roughness height	[m]
k_s^+	Non-dimensional roughness height	[-]
l	Characteristic length for the calculation of the Strouhal number	[m]
L	Vehicle length	[m]
$\mathcal{L}$	Length scale	[m]
$\mathcal{L}_t$	Turbulent length scale	[m]
M_g	Yaw moment	[Nm]
M_n	Pitch moment	[Nm]
M_r	Roll moment	[Nm]
n_v	Number of time steps for Detached Eddy Simulation	[#]
p	Static pressure of the fluid	[Pa]
p_∞	Ambient pressure	[Pa]
$\overline{p}$	Averaged pressure	[Pa]
p'	Fluctuating component of pressure	[Pa]
$\tilde{P}_k$	Production of turbulent kinetic energy	[N/m²s]
$\tilde{P}_\omega$	Production of ω	[N/m²s]
Q	Second invariant of velocity gradient	[1/s²]
R	Ideal gas constant	[kJ/kgK]
Re	Reynolds number	[-]
S	Side force	[N]
S_{ij}	Strain tensor	[1/s]
S_{kk}	Divergence of velocity	[1/s]
Sr	Strouhal number	[-]
t	Time	[s]
T	Temperature of the fluid	[K]
Tu	Turbulence intensity	[%]
u, v, w	x, y, z-components of velocity	[m/s]
u_∞	Free-stream velocity	[m/s]
$\overline{u}, \overline{v}, \overline{w}$	x, y, z-components of averaged velocity	[m/s]
u', v', w'	x, y, z-components of fluctuating velocity	[m/s]

u^*	Wall friction velocity	[m/s]
$\mathcal{U}$	Velocity scale	[m/s]
$\mathcal{U}_{turb}$	Turbulent velocity scale	[m/s]
V	Volume of a computational cell	[m³]
W	Drag force	[N]
W_D	Pressure drag	[N]
W_R	Viscous drag	[N]
y	Distance from the wall	[m]
y^+	Non-dimensional distance from the wall	[-]

Greek symbols:

α	Incident flow angle	[°]
α^*	Damping coefficient for turbulent viscosity	[-]
α_∞^*	Model constant	[-]
α_0^*	Model constant	[-]
β_i	Model constant	[-]
Γ_k	Effective diffusivities for turbulent kinetic energy	[Ns/m²]
Γ_ω	Effective diffusivities for turbulent dissipation	[Ns/m²]
δ_{ij}	Kronecker delta	[-]
Δ	Maximum local grid spacing	[m]
Δ_{mesh}	Mesh size of the anti turbulence screen in the wind tunnel	[m]
ε	Energy dissipation	[m²/s³]
κ	Contraction ratio of the wind tunnel nozzle	[-]
$\tilde{\kappa}$	Nozzle factor of the wind tunnel	[-]
λ	Slenderness ratio	[-]
μ	Dynamic viscosity	[Ns/m²]
μ_t	Turbulent dynamic viscosity	[Ns/m²]
ν	Kinematic viscosity	[m²/s]
ν_t	Turbulent kinematic viscosity	[m²/s]
ρ	Density of fluid	[kg/m³]

σ_k	Turbulent Prandtl number for turbulent kinetic energy diffusion	[-]
$\sigma_{k,1}$, $\sigma_{k,2}$	Model constant	[-]
$\sigma_{\omega,1}$, $\sigma_{\omega,2}$	Model constant	[-]
σ_ω	Turbulent Prandtl number for turbulent dissipation diffusion	[-]
τ	Shear stress	[Pa]
τ_{ij}	Stress tensor	[Pa]
τ_{ij}^t	Turbulent stress tensor	[Pa]
τ_v	Period of vortex shedding	[s]
τ_w	Wall shear stress	[Pa]
φ	Angle between the surface normal direction and the direction of the free stream velocity	[°]
ω	Turbulent dissipation	[1/s]
ω_w	Turbulent dissipation on the wall	[1/s]
ω^+	Asymptotic value of turbulent dissipation in the sublayer	[1/s]
ω_w^+	Asymptotic value of turbulent dissipation on the wall	[1/s]

1. Introduction

The diploma thesis starts with the background and the motivation to the enforcement of the work, some theoretical background of the aerodynamics of the test body and the objectives resulting of the work.

1.1. Background and motivation

The present situation in the field of global transportation calls for a marked reduction of fuel consumption. A team of students at the Graz University of Technology took this requirement as a motivation to construct a low consumption vehicle. The TERA Fennek (TERA TU Graz 2010[1]), which is shown on the photograph in Figure 1, was born. The TERA Fennek was designed to participate at the Shell Eco Marathon, which is an energy saving competition among more than 200 student teams coming from all over the world. One of the most important issues for a low consumption vehicle is, aside from the rolling resistance, the aerodynamic drag. The motivation to the present work was to gain a comprehensive insight into the special aerodynamics of the low drag body of the TERA Fennek.

Figure 1: The TERA Fennek

With the help of modern CFD methods, the design and development process could be accelerated considerably. The optimization of shape details, or basic aerodynamic studies on different body geometries can be made within a short time and with acceptable effort. The aerodynamic performance of such models can be easily assessed using CFD methods. The CFD predictions may still contain considerable errors, even though the numerical models are getting more and more accurate. An appropriate method for the evaluation of CFD results is the comparison of the computed forces, moments, or the pressure distribution on the vehicle surface against experimental data which are obtained from wind tunnel measurements. Similar to CFD studies, wind tunnel experiments can investigate well defined test

---

[1] http://www.ecoracing.tugraz.at

conditions. However, an aerodynamical optimization of the body shape carried out in the wind tunnel is much more expensive and complex than using computational methods. Nonetheless, to get real values of the acting forces and moments, a wind tunnel test is still indispensable. One major challenge of this diploma thesis work is the highly streamlined shape of the test body having basically no sharp edges. This particular feature is in contrast to most other generic test cases for automotive aerodynamics like the Ahmed or the SAE body, where the flow separation is basically enforced downstream of backward facing edges. Already these "simpler" cases are a great challenge to numerical simulations, as it was demonstrated in many benchmark tests carried out by various academic and industrial research institutions (Ahmed 1984, Drage 2008)

1.2. Aerodynamics of the test body

One of the main concerns of the automotive external aerodynamics is the drag representing the air resistance force which opposes the motion of the vehicle. This resistance is mostly described in terms of the non-dimensional drag coefficient

$$c_W = \frac{W}{\dfrac{\rho}{2} u_\infty{}^2 A_{proj.}} \tag{1.1}$$

relating the drag force W to the stagnation pressure $\rho u_\infty^2/2$ and the frontal projection area of the vehicle $A_{proj.}$ (see Figure 4). The total drag is composed of the pressure drag and the viscous drag. Figure 2 shows the pressure p acting always normal to the wall boundary and the wall shear stress τ_W acting in the tangential plane of the wall boundary. The total drag of a profile or a body is obtained as the sum of the projections of both drag forces into the direction of the oncoming flow velocity u_∞ written as

$$W = W_D + W_R \tag{1.2}$$

with
$$W_D = \oint p\cos\varphi\, dF, \quad W_R = \oint \tau_W \sin\varphi\, dF. \tag{1.3}$$

Figure 2: decomposition into pressure drag and viscous drag

dF denotes an infinitesimal surface element, φ is the angle between the surface normal direction and the direction of the free stream velocity u_∞.

The contribution of each component strongly depends on the shape of the considered body and the body's orientation with relative to the direction of the free stream velocity. Figure 3 exemplarily shows the contributions of the pressure drag and the viscous drag for five different types of bodies.
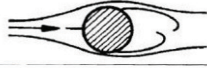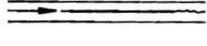
	body	pressure drag	viscous drag
1		100%	0%
2		90%	10%
3		60%	40%
4		10%	90%
5		0%	100%

Figure 3: contributions of the pressure drag and the viscous drag for different bodies (Hucho 2002)

As seen from Figure 4, the presently considered test body could be classified between the ellipsoidal (3) and the airfoil body (4) shown in Figure 3, because the basic shape of the test body essentially resembles the geometry of an airfoil. Deviations from a perfect airfoil geometry are mainly due to the casings of the wheels, where the flow along the main body is disturbed, increasing the pressure drag.
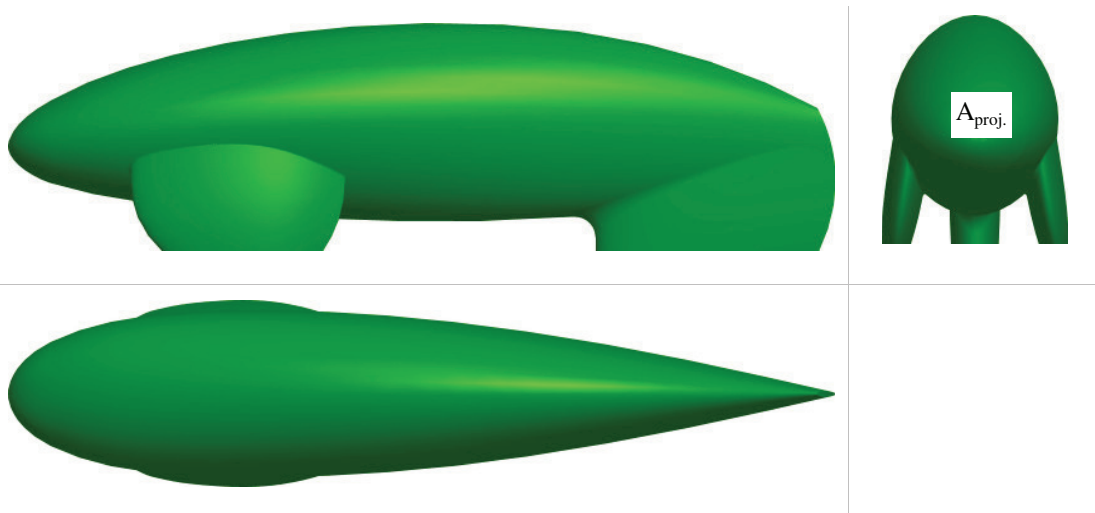
Figure 4: views of the test body

The so called slenderness ratio, which is defined as the ratio between the maximum height and the maximum streamwise length of an ellipsoidal or airfoil like body has a significant influence on the drag coefficient. Figure 5 shows the variation of the drag coefficient of an ellipsoid with the slenderness ratio at two different Reynolds numbers. A first rough estimate of the expected drag coefficient for the

presently considered body can be obtained by applying the data of the ellipsoid shown in Figure 5 to the geometry of the Fennek vehicle. For an assumed Reynolds number

$$\text{Re} = \frac{u_\infty L}{\nu} = \frac{20 \cdot 1,445}{1,46 \cdot 10^{-5}} \sim 2 \cdot 10^6 \,, \tag{1.4}$$

and the given slenderness ratio

$$\lambda = \frac{L}{d} = \frac{1,445}{0,8} = 1,8 \,, \tag{1.5}$$

the drag coefficient would be $c_W = 0,06$, and the contributions of the pressure drag and the viscous drag would be nearly the same.
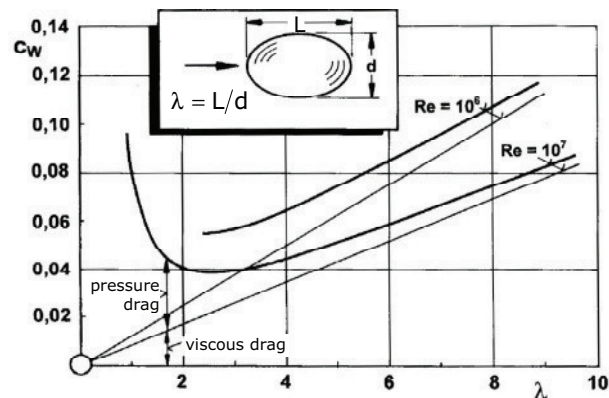
Figure 5: drag coefficient for an ellipsoid, viscous contributions denoted by thin straight lines (Hucho 2002)

A further interesting fact which is clearly illustrated in Figure 5 is that the higher the slenderness ratio, the more influence has the viscous wall friction compared to the pressure drag. The viscous drag is generated in the boundary layer. The boundary layer basically represents the thin near wall layer, where the velocity varies from the free stream velocity to zero at the surface. The boundary layer thickness is generally defined by the point, where the local velocity reaches 99% of the free stream velocity. The boundary layer displacement thickness is a characteristic length scale for the deflection of the streamlines due to the deceleration of the flow near the wall. Figure 6 shows the boundary layer on a flat plate with the corresponding velocity profiles. The gradient of the velocity with respect to y at the surface (y=0) determines the wall shear stress. The integration of the wall shear stress along the surface gives the total viscous drag.
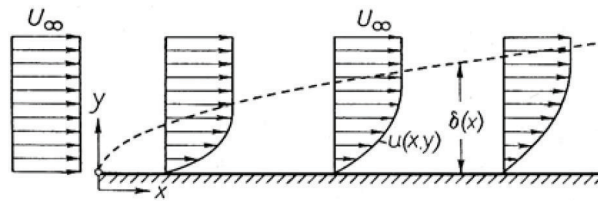
Figure 6: boundary layer on a flat plate

If the free stream is free of turbulent fluctuating motion, the oncoming flow is laminar, and the boundary layer is laminar at the beginning of the wall surface as shown in Figure 7 a. Due to the fact that no surface is perfectly smooth, there arise always small disturbances, which are growing downstream so that the flow in the boundary layer finally changes from laminar to turbulent after a critical downstream path length x_u.
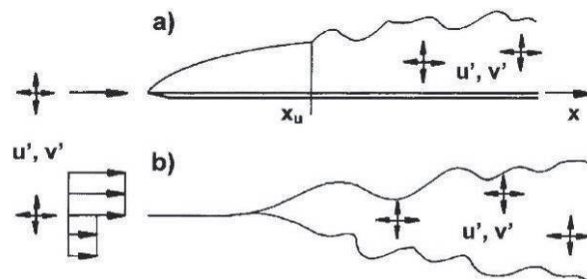
Figure 7: transition from a laminar to turbulent boundary layer, near wall and free shear layer (Ashley 1965)

Figure 8 shows the influence of the free stream turbulence on the point of transition for a slender and a bulky profile. The slender profile shown in subfigures a and c exhibits a transition from laminar to turbulent boundary layer, which remains always attached to the contour without any effects of separation. Due to the perturbation of the turbulent free stream motion the point of transition from laminar to turbulent is located further upstream for supercritical incident flow than for sub-critical incident flow. The flow along a bulky profile, which exhibits a wake region with separated flow is shown in subfigures b and d. In the sub-critical case the boundary layer may already separate upstream of the transition point, and, as shown in subfigure b, the detached flow becomes turbulent and reattaches due to the higher momentum available in the turbulent regime to counteract the retarding pressure and viscous forces. The turbulent boundary layer finally separates further downstream. For the supercritical incident flow the transition occurs already in the attached boundary layer on the upwind side. Due to the high content of kinetic energy, the turbulent boundary layer remains attached in a considerable part of the region with adverse pressure gradient. Therefore, the separation occurs further downstream as compared to the sub-critical case, which leads to a smaller wake region.

	sub critical flow	supercritical flow
attached flow (slender profile)	a) transition point, turbulent boundary layer, laminar boundary layer	c) transition point, turbulent boundary layer, laminar boundary layer
detached flow (bulky profile)	b) turbulent boundary layer, separation, separation and reattachement, laminar boundary layer, wake	d) separation, turbulent boundary layer, laminar boundary layer, wake

Figure 8: characterisation of a flow field

The design of the vehicle followed largely the principles of airplane design. Therefore all parts are basically shaped as airfoils. As a result of this design principle, a venturi nozzle like geometry was obtained between the two front wheel casings (see Figure 9), which is tainted with losses. The main challenge of the design of the front wheel casings was to keep the expansion ratio of the diffusor part of the venturi nozzle geometry as small as possible to achieve high diffusor efficiency. At the same time the streamwise length of the wheel casings had to be kept as small as possible.

Figure 9: Venturi nozzle geometry between front wheel casings

The design of the front wheel casings has also a strong influence on the incident flow of the rear wheel casing. The rear edges of the wheel casings (red marked areas in Figure 10) of the vehicle is the final point of investigation. Due to construction and manufacturing conditions the rear edges are not perfectly sharp. They are more like the trailing edge of a plate with a certain thickness, which causes the flow to separate at the rear edge producing a small wake region downstream. This also contributes to the pressure drag of the test body.
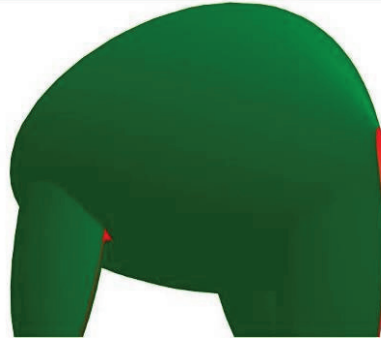
Figure 10: rear edges of the wheel casings

1.3. Objectives

The present thesis work has basically two major goals. First, the aerodynamics of the low consumption vehicle TERA Fennek shall be investigated experimentally in the wind tunnel. The measurements shall be carried out with a model downsized by 1:2 varying the angle of the oncoming flow direction. The measured flow forces obtained for different flow angles shall provide a rich data base for analyzing the aerodynamic performance of the test body. The measurements shall also be highly useful to evaluate the computational results obtained from numerical simulations of the flow around the test body which connects to the second goal of this work. In a series of numerical simulations it shall be shown, how accurately modern commercial CFD software, using advanced, meanwhile well established, turbulence models, can describe the here considered highly challenging flow. Finally, the data obtained in the measurements and the simulation shall help to further improve the shape of the TERA Fennek vehicle in the future.

2. Wind tunnel experiments

This section deals with the theoretical background, some technical and practical aspects of the wind tunnel experiments. This includes the physical principles of the applied measurement techniques as well as the design and construction of the model. The experimental setup, the measurement procedures, and the obtained experimental results will be described at the end of the section.

2.1. Wind tunnel

The wind tunnel is the classical test rig for air flow experiments. In contrast to most real life conditions, the test body stands still and the fluid moves along the test body. The fluid is generally driven by a blower to obtain a certain flow velocity. For aerodynamic measurements of road vehicles, this implies that the reference system of the test body has changed, because the fluid is moving and the test body stands still, while in reality the test body is moving. The wind tunnel design should always guarantee well controlled test conditions in the test section to ensure reliable results.
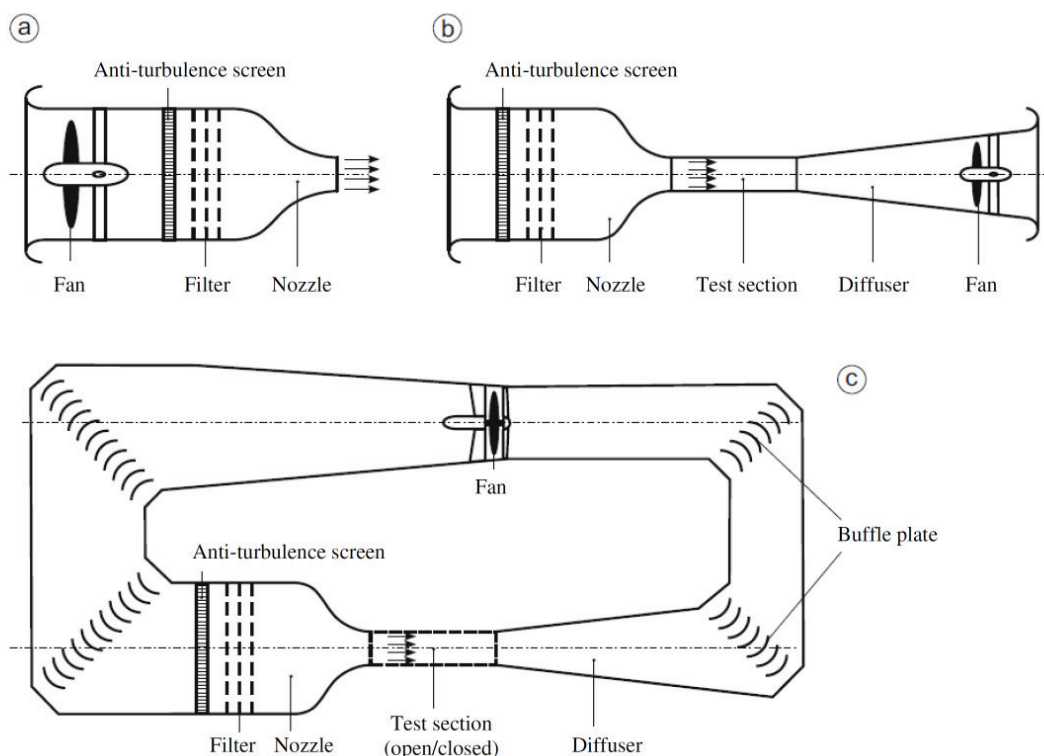
Figure 11: wind tunnel types (Nitsche 2006)

There are several approaches to design a wind tunnel. Figure 11 shows three different types of wind tunnels and their basic elements. Subfigure a shows an open jet channel, subfigure b an Eiffel channel, and subfigure c a closed loop facility often also called a Göttingen type wind tunnel.

The wind tunnel at the Institute of Fluid Mechanics and Heat Transfer is a Göttingen type tunnel with an open test section. There is the possibility to close the test section with panels. To reduce the influence of the tunnel walls on the flow around the test body, the present measurements were carried out with an open test section. Figure 12 schematically shows the influence of the side walls in a closed test section on the streamlines surrounding the test body.
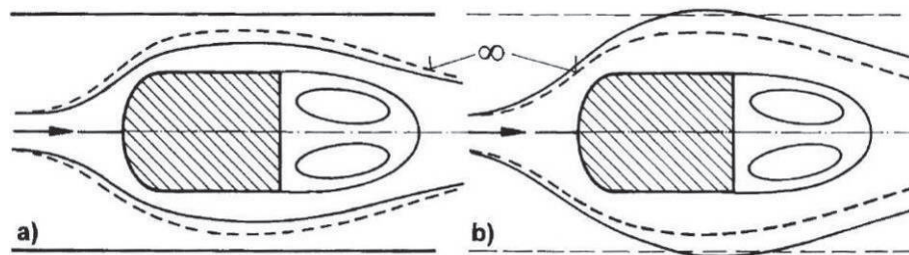
Figure 12: influence of the side walls (Hucho 2002)

The anti-turbulence screen shown in Figure 11 helps to retain uniform flow conditions downstream of the buffle plates. Several filters downstream of the anti-turbulence screen shall further dampen any existing irregularities in the flow. The flow is accelerated downstream by a nozzle, and emanates as a free stream at the nozzle outlet. The acceleration of the flow in the nozzle depends on the ratio between the cross-sectional area at nozzle inlet and the nozzle outlet. This ratio is called the contraction ratio. The contraction also reduces the turbulence at the nozzle outlet. At the outlet of the nozzle, where the outgoing free stream meets the surrounding air, eddies are generated. These eddies disturb the outer part of the free stream passing the test section. In order to reduce the impact of these eddies, so called Seiferth wings are mounted (Hucho 2005). Figure 13 shows the Seiferth wings at the nozzle outlet of the wind tunnel at the Institute of Fluid Mechanics and Heat Transfer.
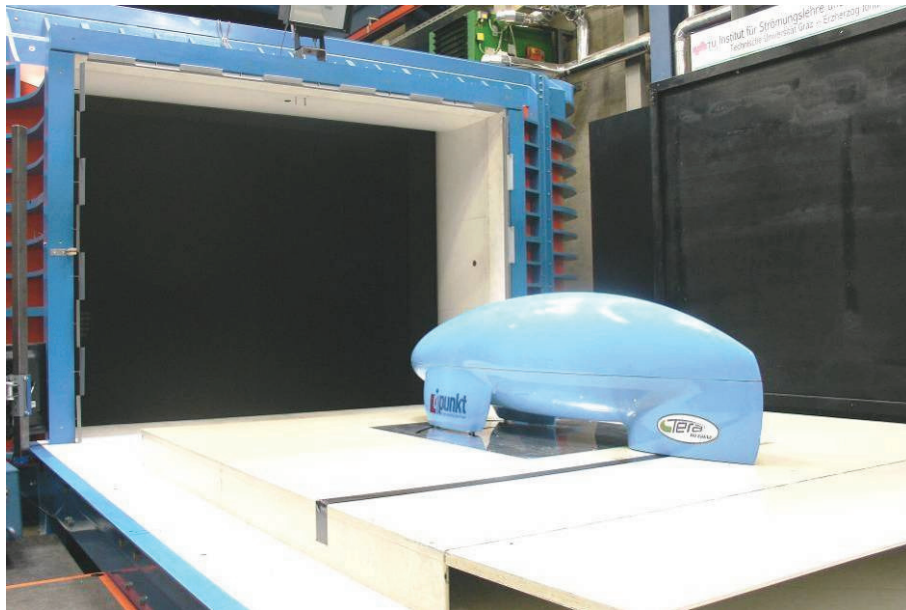
Figure 13: Seiferth wings at the nozzle outlet (Institute of Fluid Mechanics and Heat Transfer, TU Graz)

For measurements in wind tunnels the turbulence intensity at the nozzle exit plays a significant role, in particular for the comparability of the measurements with computational results. The turbulence intensity is basically influenced by the mesh size of the anti-turbulence screen. Downstream of the filters the turbulence of the flow can be regarded as isotropic. This means that the time averaged squares of the velocity fluctuations are the same in all three coordinate directions:

$$\overline{u^{'2}} = \overline{v^{'2}} = \overline{w^{'2}} \ . \tag{2.1}$$

The turbulence intensity of the wind tunnel is defined as

$$Tu = \frac{1}{u_\infty}\sqrt{\frac{1}{3}\left(\overline{u^{'2}} + \overline{v^{'2}} + \overline{w^{'2}}\right)} \tag{2.2}$$

obtained at the nozzle exit. As such it represents the "free stream" turbulence intensity. Figure 14 shows the influence of the free stream turbulence intensity on the critical Reynolds number of the flow around a NACA airfoil. The critical Reynolds number refers here to the free stream velocity, where a transition from laminar to turbulent occurs in the boundary layer of the considered airfoil.
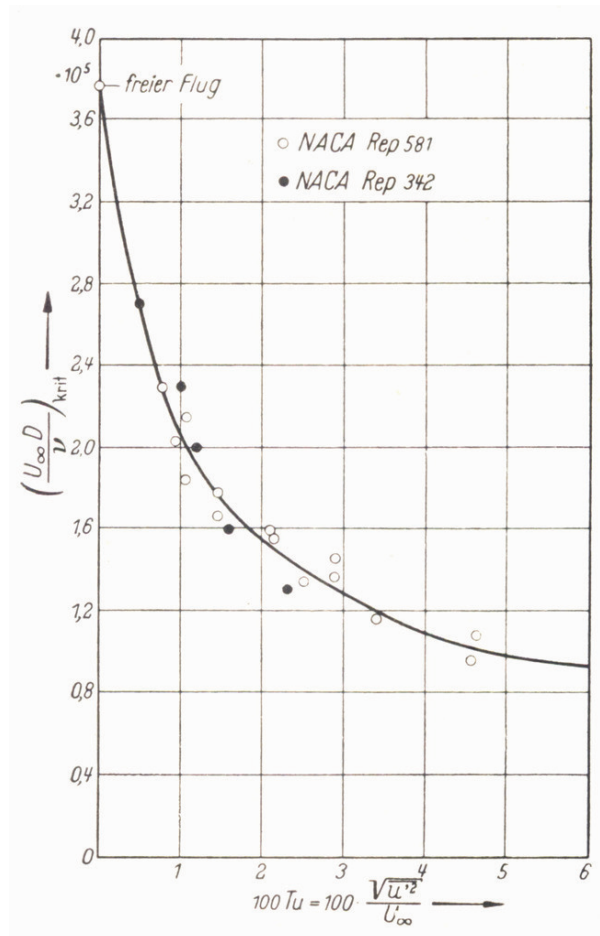
Figure 14: influence of the turbulence intensity on the critical Reynolds number (Schlichtling 2001)

The critical Reynolds Number evidently strongly decreases for higher turbulence intensities. Especially for the flow around low drag bodies, the turbulence intensity has a strong impact, because a transition from laminar to turbulent strongly increases the viscous drag, which represents major part of the total drag in the case of low drag geometries.

2.2. Methodology of measurements

2.2.1. Force measurements

The measurements of the forces and moments acting on the test body are carried out using a multi-component balance. As shown in Figure 15 the coordinate system, of the balance is cartesian, whose x-axis is aligned with the direction of the free stream velocity. The origin of the coordinate system is located on the rotational axis of the test section. The multi-component balance in the wind tunnel of the Institute of Fluid Mechanics and Heat Transfer is mounted "wind fixed". This means that the forces and moments acting on the test body have to be transformed in the case of non-zero incident flow angles

(Hucho 2005). In total, six forces are measured using six force transmitters. Based on a simple force and moment balance the drag, lift and side forces, as well as the yaw, roll, and pitch moments can be computed from the six measured forces (F_W, F_{av}, F_{ar}, F_{al}, F_{sv}, F_{sh}), as shown in Eqs. (2.3) - (2.8).
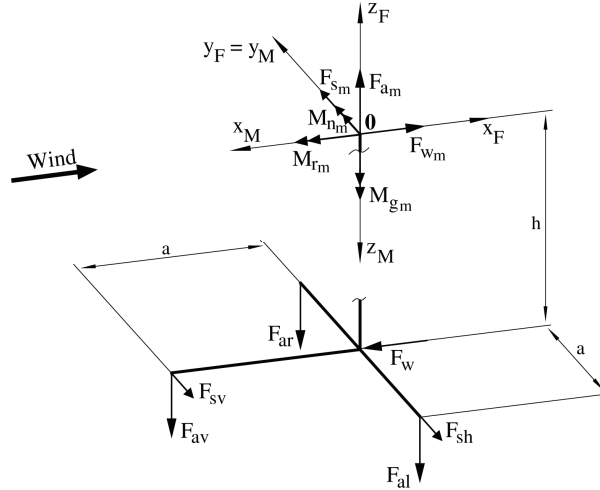
Figure 15: coordinate system of the balance and the six measured forces; forces and moments acting on the test body are denoted by subscript m

drag	$W = F_W$	(2.3)
lift	$A = F_{av} + F_{ar} + F_{al}$	(2.4)
side force	$S = F_{sv} + F_{sh}$	(2.5)
yaw moment	$M_n = F_{av}a - F_W h$	(2.6)
roll moment	$M_r = (F_{al} - F_{ar})a - (F_{sh} + F_{sv})h$	(2.7)
pitch moment	$M_g = F_{sv}a$	(2.8)

2.2.2. Measurement of the free stream velocity

The measurement of the nozzle exit velocity representing the free stream velocity u_∞ is based on the measurement of local static pressures using pressure sensors. For the measurement of the free stream velocity in wind tunnels, two methods are available: the nozzle method and the plenum method. The latter is applied in the wind tunnel at the Institute of Fluid Mechanics and Heat Transfer. In the plenum method the pressure difference between the nozzle inlet and the environment is used to determine the free stream velocity u_∞ entering the test section. Figure 16 shows the principle of the plenum method.
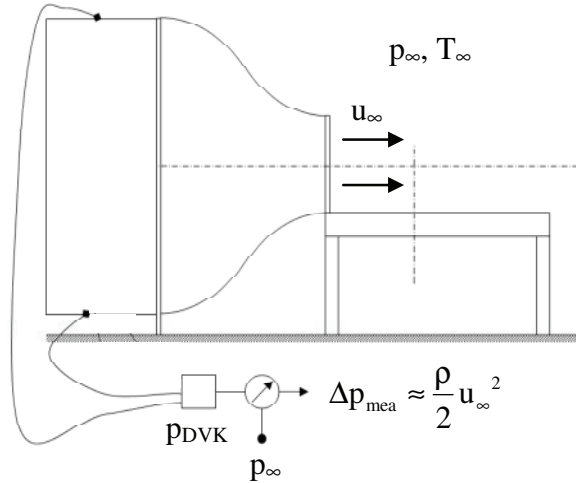
Figure 16: plenum method for measurement of free stream velocity

Substituting the measured static pressure difference $\Delta p_{mea} = p_{DVK} - p_\infty$ into the Bernoulli equation and incorporating the continuity equation finally yields the free stream velocity as shown in Eqs. (2.9) - (2.12).

Bernoulli equation:

$$p_{DVK} + \frac{\rho}{2} u_{DVK}{}^2 = p_\infty + \frac{\rho}{2} u_\infty{}^2 \qquad (2.9)$$

Continuity equation:

$$A_{DVK} u_{DVK} = A_D u_\infty \qquad (2.10)$$

Pressure difference:

$$\Delta p_{mea} = p_{DVK} - p_\infty = \frac{\rho}{2} u_\infty{}^2 \left[1 - \left(\frac{A_D}{A_{DVK}} \right)^2 \right] \qquad (2.11)$$

Contraction ratio:

$$\kappa = \frac{A_{DVK}}{A_D} = 5,58 \qquad (2.12)$$

The inverse of the contraction ratio occurring in Eq. (2.11) is negligible. The calibration of this measurement method introduces a nozzle factor $\tilde{\kappa}$ instead. The nozzle factor is defined as the ratio between the measured dynamic pressure $\left(\frac{\rho}{2} u_\infty^2 \right)_{mea}$ and the measured pressure difference Δp_{mea}. The free stream velocity is then computed from

$$u_\infty = \sqrt{\frac{2}{\rho} \tilde{\kappa} \Delta p_{mea}} \ . \qquad (2.13)$$

In consideration of the fact that the air can be assumed as a perfect gas, the density can be calculated using the equation of state of perfect gas written as

$$\frac{p}{\rho} = RT \, . \tag{2.14}$$

Substituting Eq. (2.14) into Eq. (2.13), the free stream velocity is obtained as

$$u_\infty = \sqrt{2RT_\infty \left(\frac{p_{DVK}}{p_\infty} - 1 \right) \tilde{\kappa}} \, . \tag{2.15}$$

2.2.3. Pressure measurements

To measure the static pressure distribution on the surface of the test body, it is necessary to drill holes into the surface. The theoretical background of this measurement method gives us Bernoulli's equation. The Bernoulli equation says that the total pressure is constant, such that

$$p_{tot} = p + \frac{\rho}{2} u^2 + \rho g h = const. \tag{2.16}$$

involving the dynamic pressure $\qquad\qquad p_{dyn} = \frac{\rho}{2} u^2 \, , \tag{2.17}$

and the hydrostatic pressure $\qquad\qquad p_{hydrostat} = \rho g h \, . \tag{2.18}$

The hydrostatic pressure has no influence in our case. Thus, only the static and the dynamic pressure are relevant. Since the velocity is zero at the wall, there is only static pressure at the wall, which can be obtained directly as the pressure measured inside the pressure hole (see Figure 17).
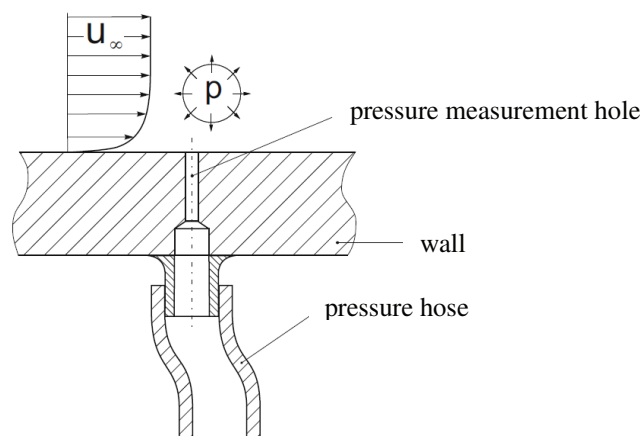
Figure 17: pressure measurement hole in the wall (Nitsche 2006)

The static pressure is the normal force per unit area of the test body. The surface integral of the differential pressure force projected into the streamwise direction finally gives the total pressure drag of the body as given by Eq. (1.3). For the evaluation of the results of the pressure measurements, it is useful to use the non-dimensional pressure coefficient c_p

$$c_p = \frac{p - p_\infty}{\frac{\rho}{2} u_\infty^2} . \tag{2.19}$$

2.3. Construction of the test body

The model was made of polyurethane foam using a five axis milling machine. The grooves caused by the milling machine were smoothened by hand. The model was split into two parts, so that the measurement equipment could be easily mounted inside each part. Figure 18 shows the moulded body after the smoothening.

Figure 18: moulded body

After the smoothening of the surface in several steps with different grinding papers, the model was painted blue in the paint shop. The painting has two advantages. The first advantage is that the paint coating increases the durability of the surface of the model, because the polyurethane foam is not robust enough to endure the permanent handling during the measuring process. The second advantage is, that it provides a very smooth surface. Figure 20 and Figure 19 show the painted body with the bore holes and the process of marking the exact positions of the pressure measurement probes.

Figure 19: marking of the positions of the holes for the pressure measurements

Figure 20: painted body with bore holes for the pressure measurements

After the pressure measurement holes were marked and drilled, the prepared pressure probes could be fixed in the holes with epoxy glue. For the preparation of the probes, the required drilling depth for each hole was determined from the CAD model. Depending on this depth, the probes, which are basically thin capillary tubes, were clipped to the required length and then fixed appropriately in the bore holes using positioning bushes. The probes have an inner diameter of 0.5 mm. The outer diameter is 5 mm. Figure 21 shows the pressure probes and the positioning bushes.

Figure 21: pressure measurement sensors

The exact shape of the bore holes is very important. Figure 22 shows the errors of the drag coefficient, in percent referring to the value of the perfect reference hole, which occur due to deviations in the geometry and orientation of the bore hole.
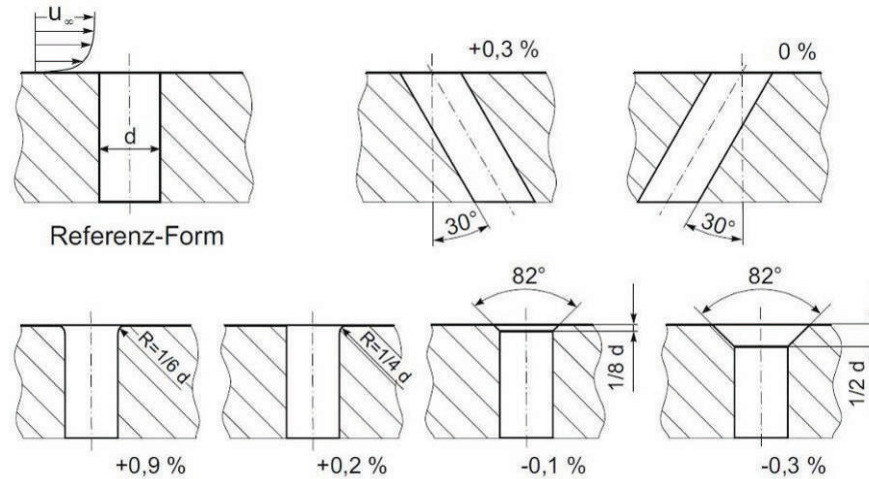
Figure 22: measurement errors due to deviations of the geometry of the pressure holes from the desired reference shape (Nitsche 2006)

The exact positions of the measurement points are shown in Figure 23 through Figure 27. The individual points are basically assembled along virtual lines along the surface. The positions of these lines can be seen from the frontal view of the model in Figure 28.
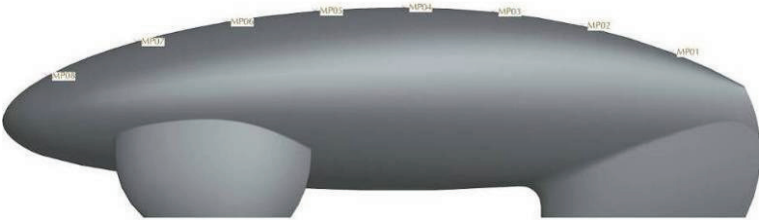
Figure 23: measurement points 1-8 (line a)

Figure 24: measurement points 9-23 (line b), and 44-58 (line c) on the back side

Figure 25: measurement points 24-28 (line d), and 39-43 (line e) on the back side
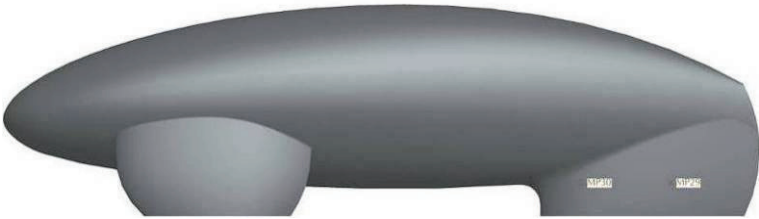
Figure 26: measurement points 29-30 (line f), and 37-38 (line g) on the back side
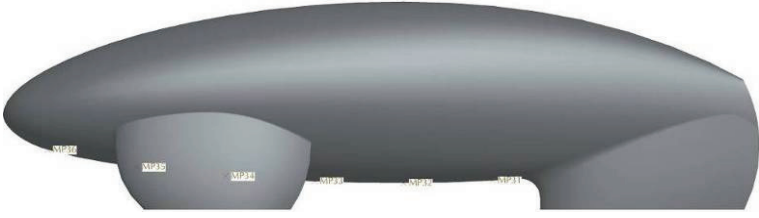
Figure 27: measurement points 31-36 (line h)

The pressure has to be measured on both sides of the test body, because different angles of the oncoming free stream velocity are to be considered.
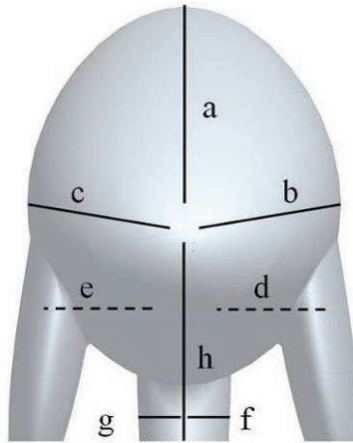
Figure 28: virtual lines connecting the positions of the pressure measurement points, frontal view of the test body.

2.4. Experimental setup

Figure 29 shows the test section and the sections up- and downstream of it.
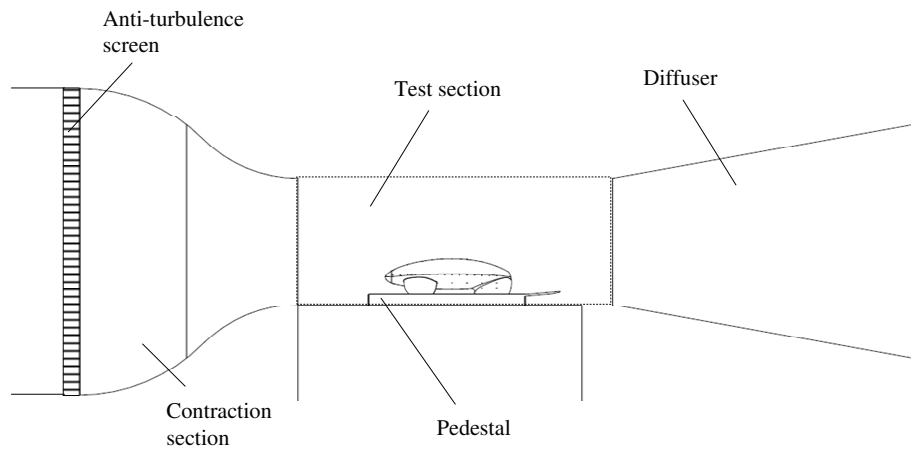
Figure 29: wind tunnel test section

The main technical data of the wind tunnel are given in Table 1.

Table 1: technical specifications of the wind tunnel

Type	Göttingen type with open test section
Driving power of the blowers	150 kW
Maximum wind speed	41,5 m/s
Nozzle cross section	2,0 x 1,46 m²
Contraction ratio of the nozzle	5,58
Length of the test section	3,5 m
Turbulence intensity at the nozzle exit	0,13 %

The turbulence intensity is a parameter for the magnitude of the velocity fluctuation averaged over all three coordinate dimensions. Figure 30 shows the turbulence intensity of the wind tunnel at the Institute of Fluid Mechanics and Heat Transfer measured in a previous work (Bair 1989). The measurements were carried out at the centre of the nozzle outlet for varying flow velocities u_∞. The averaged turbulence intensity is denoted by the red line in Figure 30, and it has a value of Tu=0,13%.
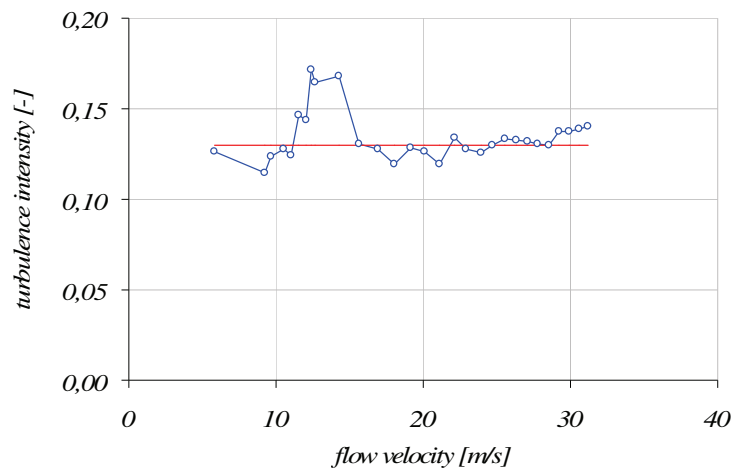
Figure 30: turbulence intensity at the centre of the nozzle outlet plane (Bair 1989).

2.4.1. Pedestal

To ensure that the influence of the wall boundary layer, which develops on the bottom plane in the region upstream of the test body, is as small as possible, the test body is placed on an open pedestal, which represents essentially a flat square channel with a flap at the upper rear edge. The pedestal is about 100 millimetres high, so that the leading edge of its upper wall is in the free stream region. As the pedestal is an obstacle for the oncoming flow, the streamlines are not parallel to the bottom of the test section, and the air flow passes the pedestal in such a way, that the stagnation point is not exactly located at the

leading upper edge. To control the exact position of the stagnation point, a device for measuring pressure differences was mounted near the leading edge. The angle of the flap was varied until the difference of the pressures measured on the upper and the lower side of the top wall of the pedestal became zero. The pressure difference was measured using a u-tube pressure gauge, as shown in Figure 31.
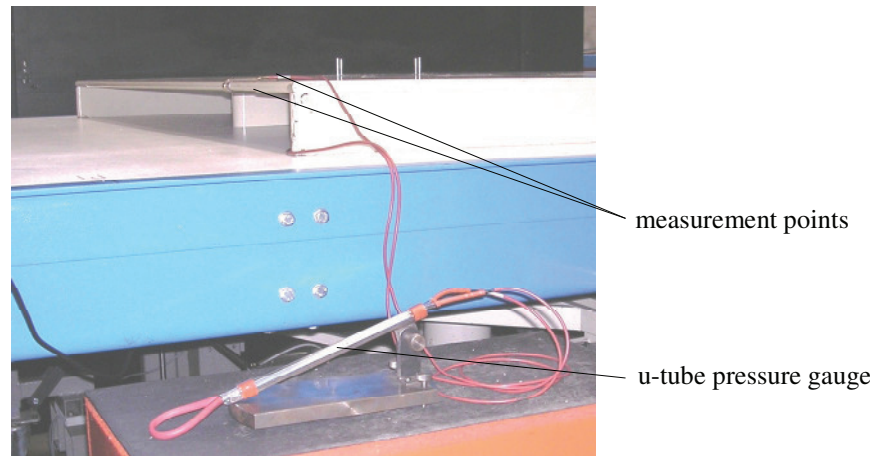
Figure 31: open pedestal in the test section

2.4.2. Mounting of the test body

The connection between the multi-component balance and the test body is a steel pipe with a mounting plate at the top end. The test body was mounted with four adapters which are fixed on the plate.
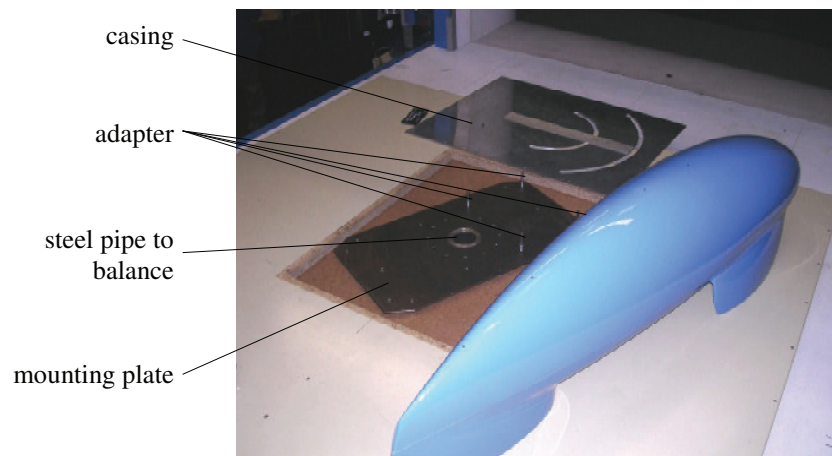
Figure 32: mounting plate with adapters and casing

The casing of the mounting plate has concentric circular cuts, so that the model could be turned relative to the direction of the oncoming free stream velocity within an angular range of -25° to +25°. In the front wheel casings of the model, four short aluminium tubes, whose inner diameter fits exactly with the

adapters on the mounting plate, were built in. The free gaps between the casing and the bottom surface were closed with a tape.

2.4.3. Pressure measurement equipment

The modules containing the pressure measurement sensors were mounted inside the wind tunnel model. Figure 33 shows the sensor modules (modules S1, S2, S3, S4), which are connected through hoses with the individual probes. Four modules were used providing in total 41 access points. Because of the limited pressure measurement range of some sensors, only 36 access points were finally used.
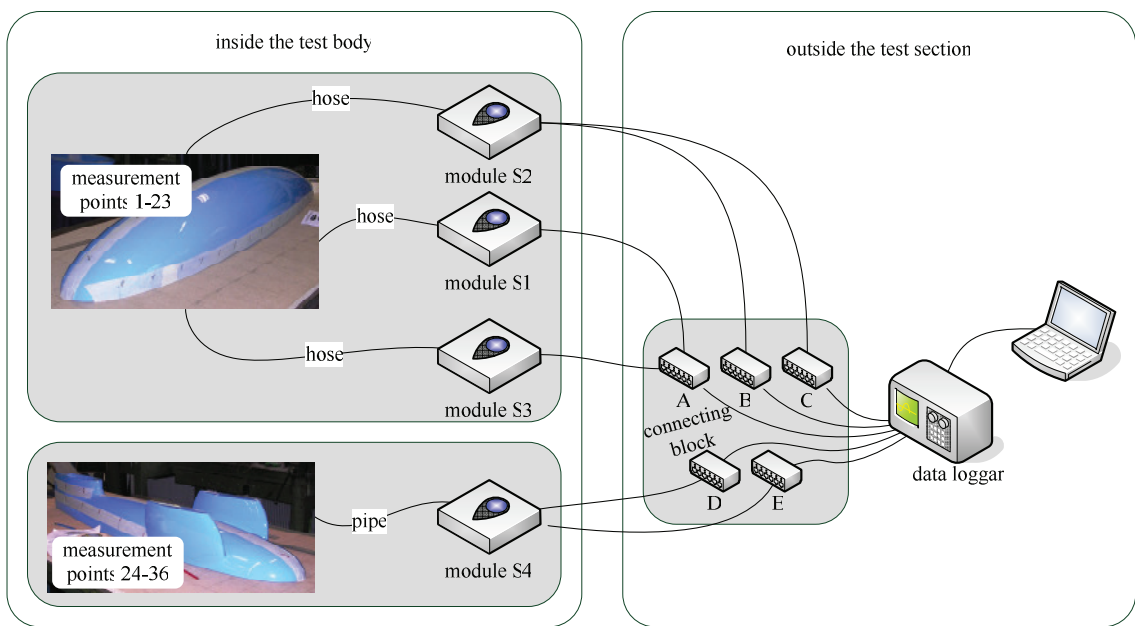
Figure 33: pressure measurement chain

Table 2 to Table 5 show the installed pressure sensor modules with the correponding technical data and the measurement points which are connected to the modules

Table 2: module S1
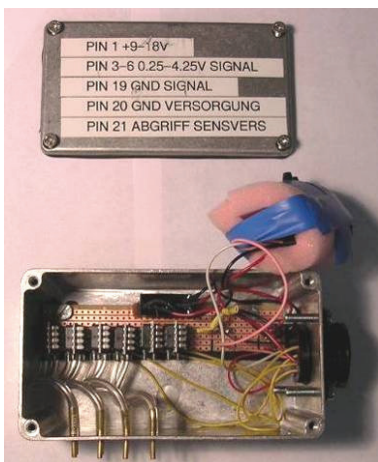
sensortype	HCLA12x5…U (Sensortechnics 2010)
number of sensors	4
operating pressure range	-1250 … 1250 Pa
output signal	250 … 4250 mV
supply voltage	9 … 18 V
non-linearity and hysteresis	±0.05 %FSS
measurement points	mp01 – mp04

Table 3: module S2
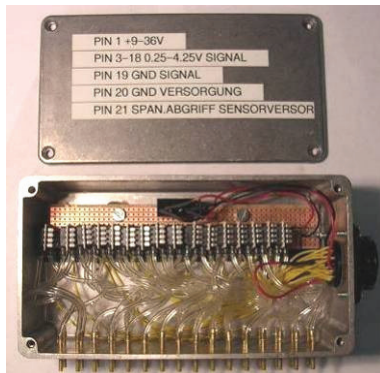
sensortype	HCLA12x5…U (Sensortechnics 2010)
number of sensors	12
operating pressure range	-1250 … 1250 Pa
output signal	250 … 4250 mV
supply voltage	9 … 18 V
non-linearity and hysteresis	±0.05 %FSS
measurement points	mp05 – mp07, mp09 – mp21

Table 4: module S3
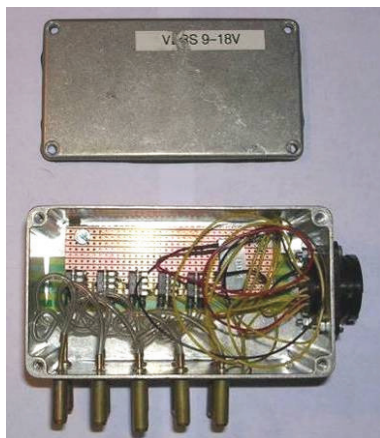
sensortype	HCLA02x5…U (Sensortechnics 2010)
number of sensors	5
operating pressure range	0 … 250 Pa
output signal	250 … 4250 mV
supply voltage	9 … 18 V
non-linearity and hysteresis	±0.05 %FSS
measurement points	mp08, mp22, mp23

Table 5: module S4
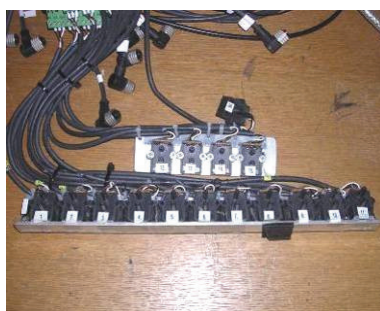
sensortype	1 MBAR-D-4V-MIL (Natec 2010)
number of sensors	16
operating pressure range	0 … 249 Pa
output signal	0 … 4 V
supply voltage	4,5 … 5,5 V
non-linearity and hysteresis	0,05 %fs
measurement points	mp24 – mp36

For the connection of the sensor units with the data logger, a channel was carved in the pedestal. Figure 34 shows the cable channel and the sensor for the reference pressure.
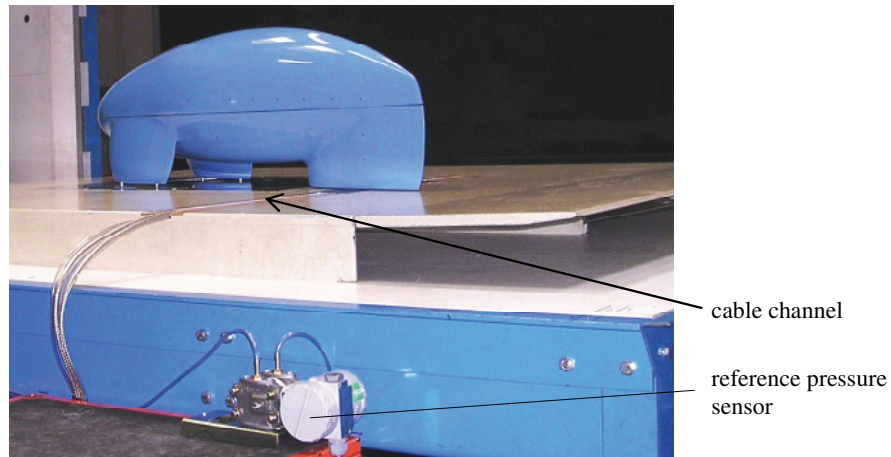
Figure 34: cable channel and reference pressure sensor

The data logger records the voltage signals sent by the individual pressure sensors with a sampling rate $5000s^{-1}$. Using the Software DEWESoft (DEWESoft 2010), the voltage signals are converted into pressure values. Figure 35 shows the whole pressure measurement equipment mounted inside the test body.
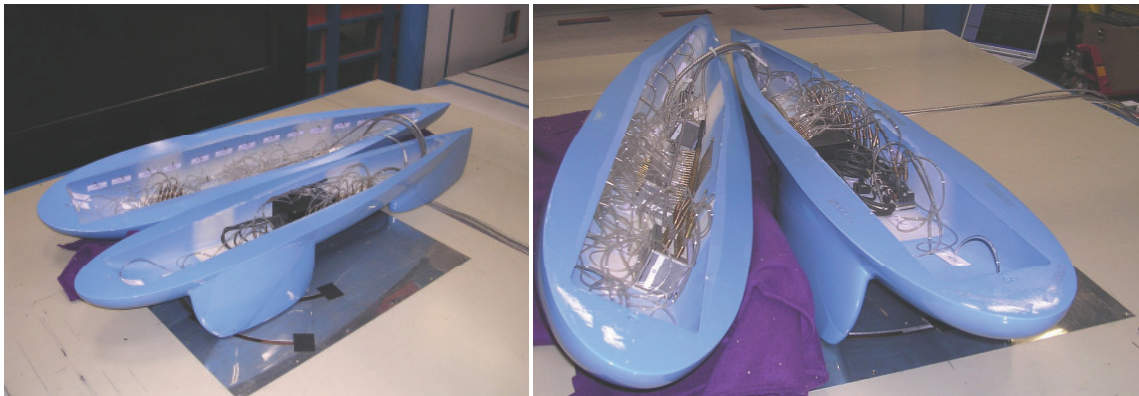
Figure 35: pressure measurement equipment mounted inside the test body

Due to the fact that the wind tunnel at the Institute of Fluid Mechanics and Heat Transfer has a test section length of 3,5 meters and a cross section of 2,92 square meters, it was decided to use a downsized model on a scale of 1:2 for the wind tunnel testing. Figure 36 shows the scaled and the real size model positioned in the wind tunnel test section. The nose and the rear end of the full size model would be unacceptable close to the nozzle upstream and the diffusor downstream, respectively. Additionally, the blockage ratio, which is the percentage of model's projection surface into the streamwise direction relative to the cross-sectional area of the nozzle, would exceed the acceptable limit of 10% for the full size model in the cases with higher incident flow angles.

Figure 36: scaled and real size model in the test section

To obtain comparable results between the real situation and the wind tunnel tests, Reynolds similarity has to be satisfied. This requires the Reynolds number to be the same for the flow around the real vehicle and the model in the wind tunnel, so that

$$\text{Re}_1 = \text{Re}_2 \text{, or} \tag{2.20}$$

$$\frac{u_{\infty 1} L_1}{\nu_1} = \frac{u_{\infty 2} L_2}{\nu_2} \tag{2.21}$$

Using a model of a scale 1:2 as shown in Figure 37, the ratio of the characteristic length scales is $L_1/L_2=1/2$. With $\nu_1=\nu_2$ this implies that the free stream velocity has to be twice as high in the wind tunnel experiments

$$\frac{u_{\infty 1}}{u_{\infty 2}} = \frac{L_2}{L_1} = 2 \,. \tag{2.22}$$
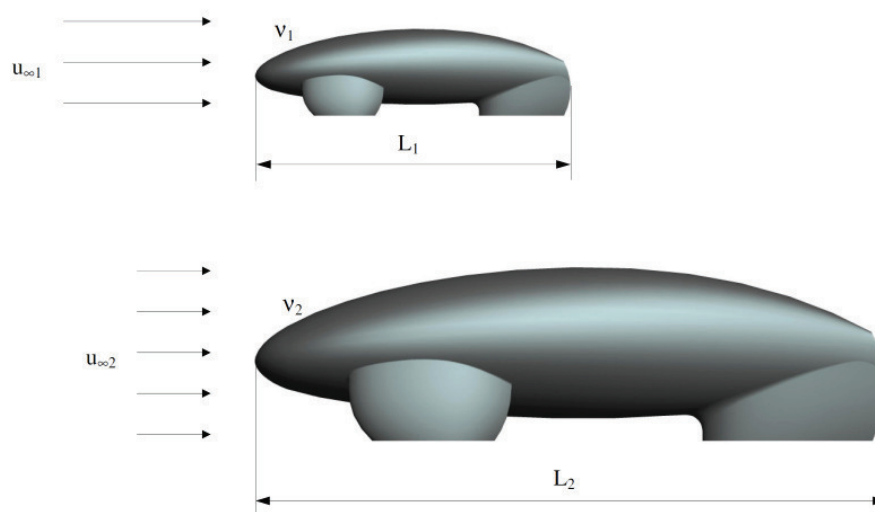
Figure 37: wind tunnel model and full size vehicle, Reynolds similarity

2.4.4. Measurement procedures

The measurements of the aerodynamic forces have to ensure that the connecting bar with the balance is the only mechanical connection of the test body with the surrounding structure. This requirement can not be fully met in the measurements of the pressure, where the wires connecting the pressure sensor modules with the data logger exit the model at the bottom of the rear wheel casing. This additional mechanical connection with the surroundings may introduce undesired spurious forces and moments at the downstream end of the model. Therefore, it was decided to carry out two separate test series, one series for the force measurements, and one for the pressure measurements. In order to provide a rich data base for a comprehensive comparison against numerical results covering highly complex flow configurations with significant separation, the angle of the incident free stream velocity, α, was varied in steps of 2,5° within the range +25° and -25° in the experiments. For each incident flow angle three velocities were considered, u_∞=10/20/30 m/s, which corresponds to Reynolds numbers $Re = 1 \cdot 10^6 / 2 \cdot 10^6 / 3 \cdot 10^6$.

The different incident flow angles were realized by rotating the model relative to the streamwise axis of the test section. Figure 38 shows the apparatus for adjusting the flow angle.

Figure 38: angular adjustment

The velocity of the incident flow is controlled via the rotational speed of the blowers of the wind tunnel.

Each measurement campaign was started with a thermal preconditioning of the facilities to ensure that the temperatures in the test section and the surroundings are the same so that the density is uniform. For each angular position of the test body relative to the incident flow the aerodynamic forces were measured imposing the three considered free stream velocities and zero velocity for reference purpose. The measurement time for each of these cycles was 30 seconds. The raw data measured by the balance were post-processed by the wind tunnel software to provide the time averaged flow forces and moments acting on the test body.

The procedure for the handling of the wind tunnel made for the pressure measurements was essentially the same as that for the force measurement. Due to the limited availability of pressure sensors only one side of the wind tunnel model was fitted with pressure sensors. Therefore a pressure measurement for negative and positive incident angles is necessary to get a pressure measurement all over the test body. Figure 39 shows the procedure for the data acquisition of the measured pressure for the single measurement points on the test body surface. The green marked area in Figure 39 show the area were the pressure probes were mounted. For each incident flow angle two measurements were made. So there are at least four measured values for the upper and the lower measurement points (see lines a and line h in Figure 28). For the other measurement points only two measurements are available to make an average value. Figure 39 shows the schema for the calculation of the values for the single measurement points from the raw measurement data and additional the positions of the pressure measurement lines. Further information of the positions of the pressure lines shows Figure 23 through Figure 28.
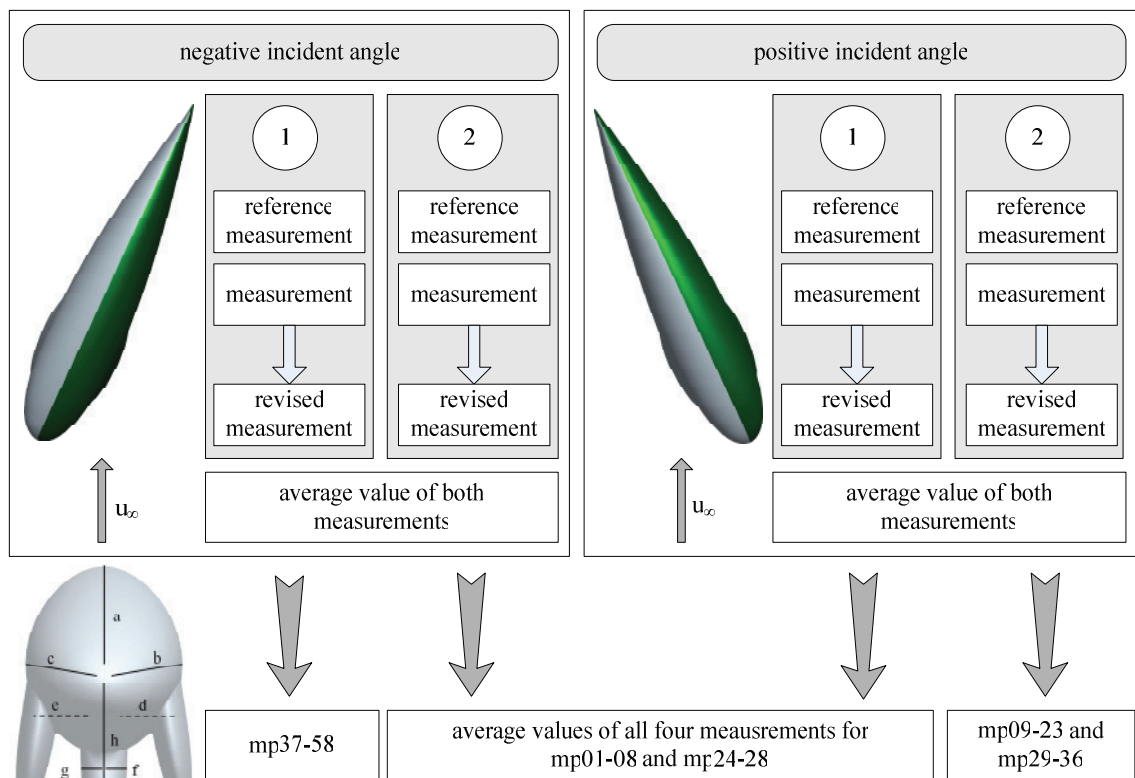
Figure 39: data acquisition procedure

2.5. *Experimental results*

Knowing the measured aerodynamic forces and moments acting on the test body, the individual non-dimensional forces and moments are computed as follows:

drag coefficient
$$c_W = \frac{W}{\frac{\rho}{2} u_\infty^2 A_{proj.}}$$
(2.23)

lift coefficient
$$c_A = \frac{A}{\frac{\rho}{2} u_\infty^2 A_{proj.}}$$
(2.24)

side force coefficient
$$c_S = \frac{S}{\frac{\rho}{2} u_\infty^2 A_{proj.}}$$
(2.25)

roll moment coefficient
$$c_r = \frac{M_r}{\frac{\rho}{2} u_\infty^2 A_{proj.} L}$$
(2.26)

pitch moment coefficient
$$c_n = \frac{M_n}{\frac{\rho}{2} u_\infty^2 A_{proj.} L}$$
(2.27)

yaw moment coefficient
$$c_g = \frac{M_g}{\frac{\rho}{2} u_\infty^2 A_{proj.} L}$$
(2.28)

They involve the projected area into the principal axis of the test body $A_{proj.} = 0,0973m^2$, and the length of the test body $L = 1,445m$, as geometrical reference quantities. These reference values are kept the same for all angles of incident flow. The coefficients experimentally obtained for the individual incident flow angles are shown in Figure 40 through Figure 46.

The measurements of the drag coefficient shown in Figure 40 are essentially symmetric for the positive and negative incident flow angles, as it is expected. Another interesting feature is the vanishing influence of the Reynolds number for higher incident flow angles. This indicates that the Reynolds number mainly affects the viscous drag, which is the dominant drag component in the cases with small incident flow angels α.
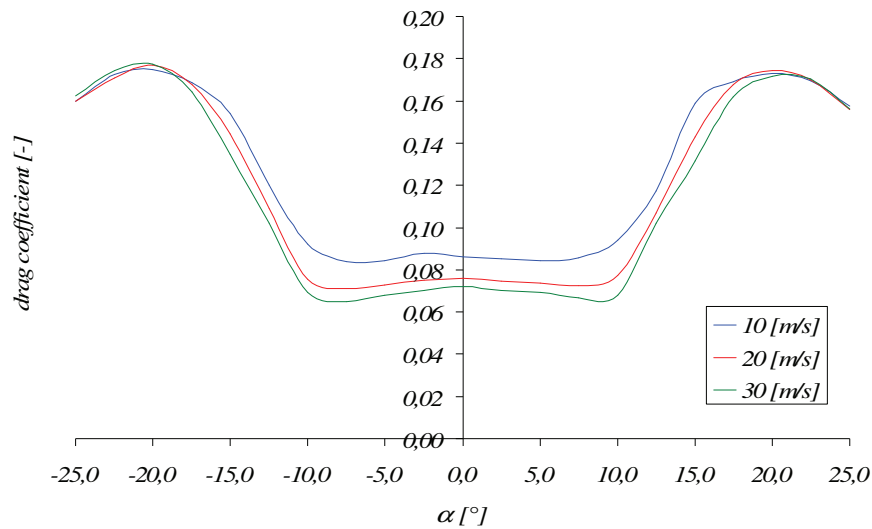
Figure 40: drag coefficient vs. incident flow angle α

The marked increase of the drag coefficient for $\alpha > 10°$ can be explained by looking at the frontal view of the test body for different incident flow angles, as shown in Figure 41. Within $10° \leq \alpha \leq 25°$ the area projected into the direction of the oncoming flow evidently increases by a factor more than two, as seen from the subfigure on the right side. This fast increase of the projected area is well in line with the increase of the drag observed in Figure 40 for $\alpha > 10°$. It is also visible, that beyond 20°, an open gap appears between the casing of the front and that of the rear wheel which may facilitate the flow passage on the lower side of the body.
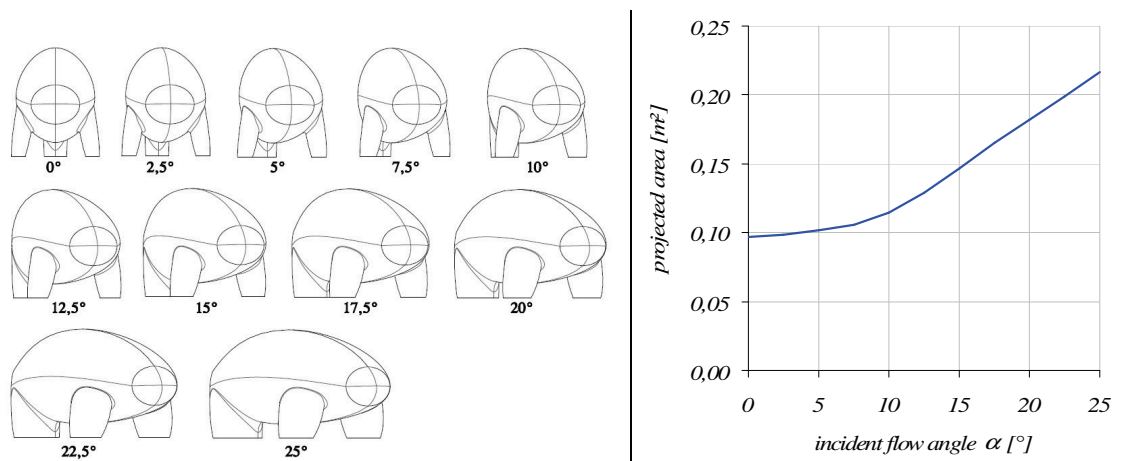
Figure 41: front view for different incident flow angles and projected area

The lift coefficient (see Figure 42) shows the same dependence of the Reynolds number like the drag coefficient. A very interesting fact is that the absolute value for incident flow angle of 25 degrees is about six times the value for zero incident flow. In contrast, the drag coefficient increases by a factor of two.
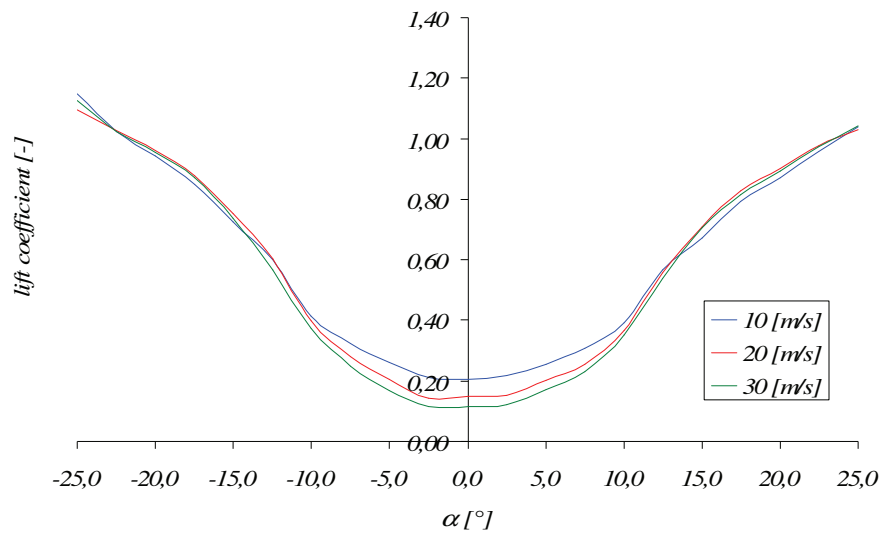
Figure 42: lift coefficient vs. incident flow angle α

The variations of the side force coefficient with α shown in Figure 43 are skew-symmetric as expected, and there is nearly no influence of the Reynolds number visible. This indicates that the side force is mostly due to pressure drag. The growth of the side force follows again the increase of the projected area for varying incident flow angles (see Figure 41), but, unlike the drag coefficient, with a less abrupt change around $\alpha \approx 10°$.
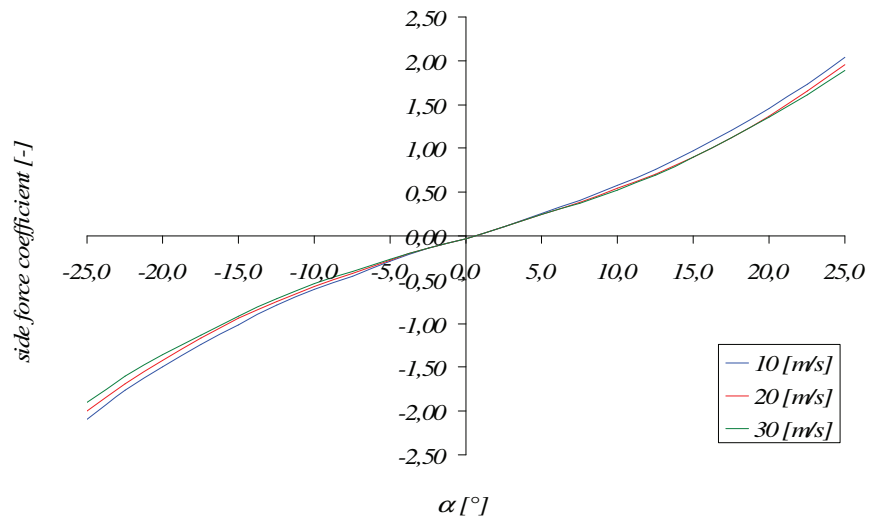
Figure 43: side force coefficient vs. incident flow angle α

The measured variations of the yaw moment with α shown in Figure 44 are skew-symmetric as expected. They show no influence of the Reynolds number for small incident angles, but a somewhat greater influence for higher incident flow angles. The increase of the yaw moment induces a higher acting side force on the rear wheel casing for higher incident flow angles with the maximum level for α=15°.
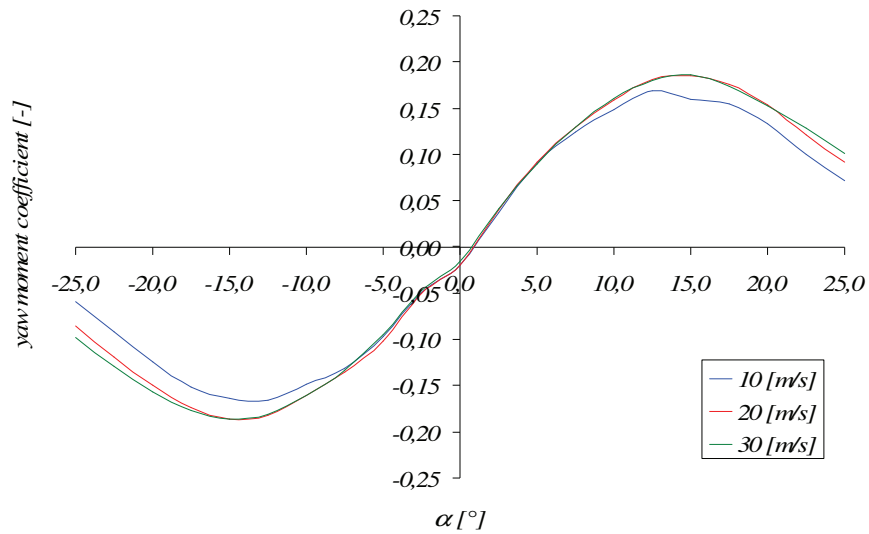
Figure 44: yaw moment coefficient vs. incident flow angle α

The pitch moment shown in Figure 45 gives information on the streamwise position of the resulting lift force. For small incident flow angles the position of the resulting lift force is close to the front wheels leading to large positive pitch moments. For higher incident flow angles the position of the resulting lift force is evidently shifted downstream, as indicated by the decreasing pitch momentum, which finally becomes negative around α=15°. The pitch moment shows a comparatively strong influence of the Reynolds number due to its dependence on the drag force.
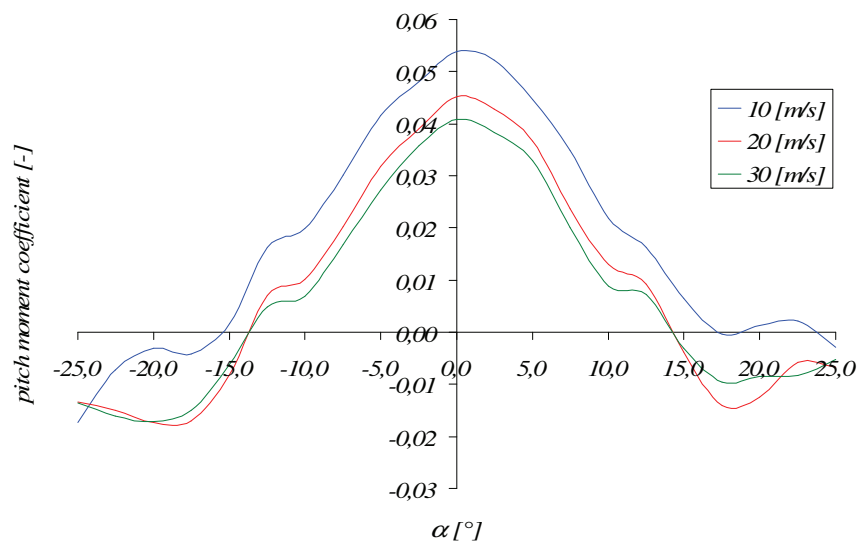
Figure 45: pitch moment coefficient vs. incident flow angle α

The variations of the measured roll moment with α (see Figure 46) show the same skew-symmetric trend lines as the side force coefficients pointing out their strong correlations with each other.
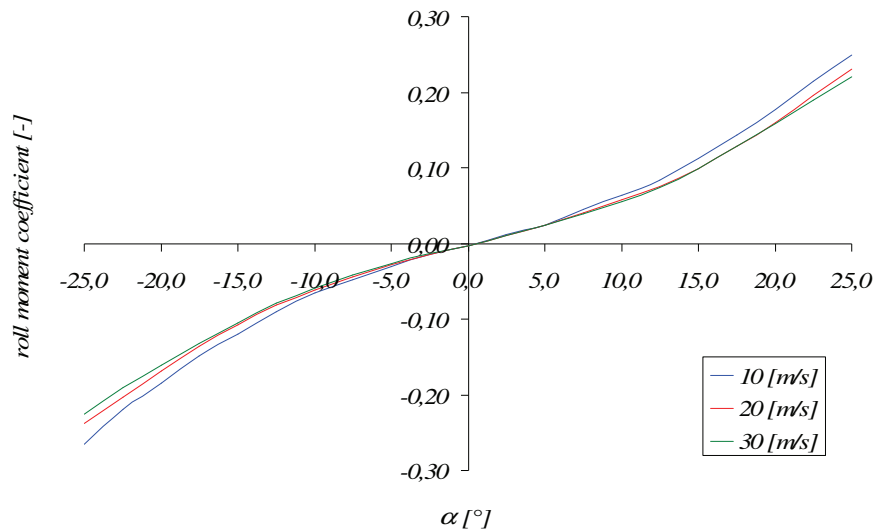
Figure 46: roll moment coefficient vs. incident flow angle α

The marked increase in the lift coefficient observed in Figure 42 is also reflected by the measurements of the static pressure at distinct points on the surface of the body. As already shown in the previous subsection 2.3, the measurement points are located along virtual lines along the surface. The positions of these lines are shown here again in Figure 47.
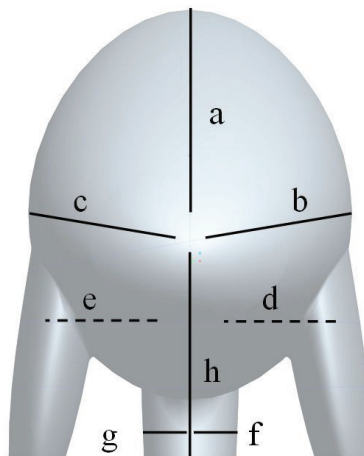
Figure 47: virtual lines connecting the positions of the pressure measurement points, frontal view of the test body

Figure 48 and Figure 49 displays the variations of the local pressure coefficient along the upper and lower meridional lines a and h for two different flow angles α. While the pressure distribution on the lower side (line h) remains essentially the same for both angles, the pressure on the upper downstream side (line a) remains on a much lower level for higher incident flow angle pointing at a significant flow separation on the downwind side of the body. The higher difference of the pressure on the upper and the lower side effectively leads to the higher lift forces for $\alpha=12,5°$.
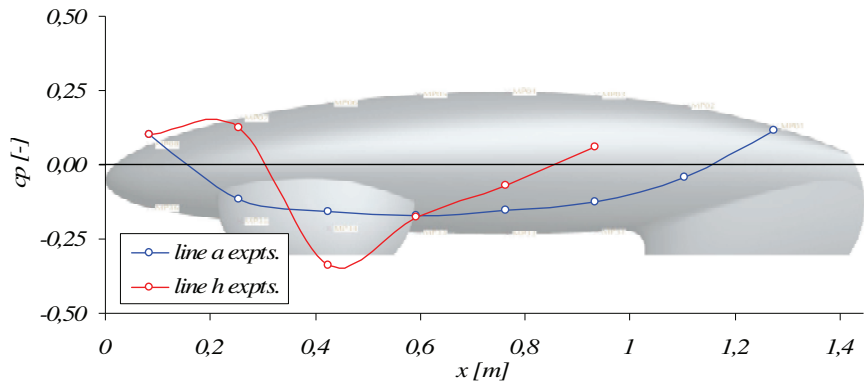
Figure 48: pressure coefficients along lines a and h for zero incident flow angle
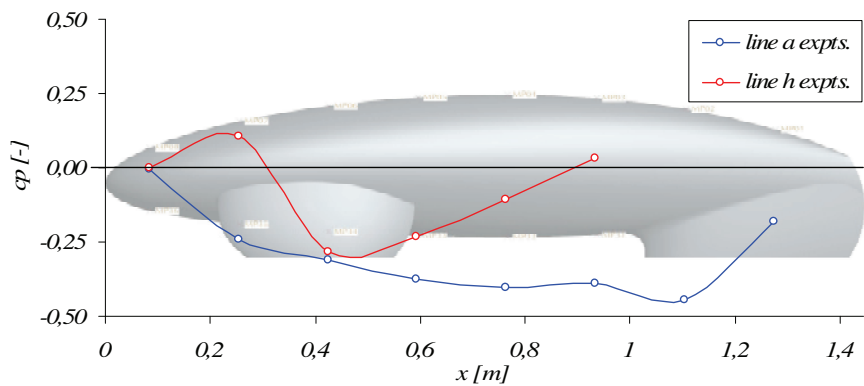
Figure 49: pressure coefficients along lines a and h for $\alpha=12,5°$ incident flow angle

A further example for the results of the local pressure measurements is shown in Figure 50 and Figure 51. The shown coefficients were measured along the equatorial lines b and c. For symmetric flow conditions associated with $\alpha=0°$, the measurement on both sides coincide, as it has to be expected. For $\alpha=12,5°$ the data obtained the upwind and the downwind side differ significantly as the flow separates in the wake region. This pressure difference is the main reason for the significant side forces discussed in Figure 43.
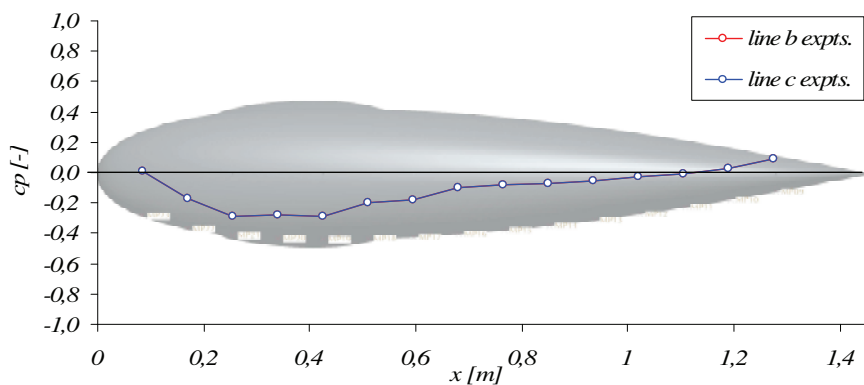
Figure 50: pressure coefficients along lines b and c for zero incident flow angle
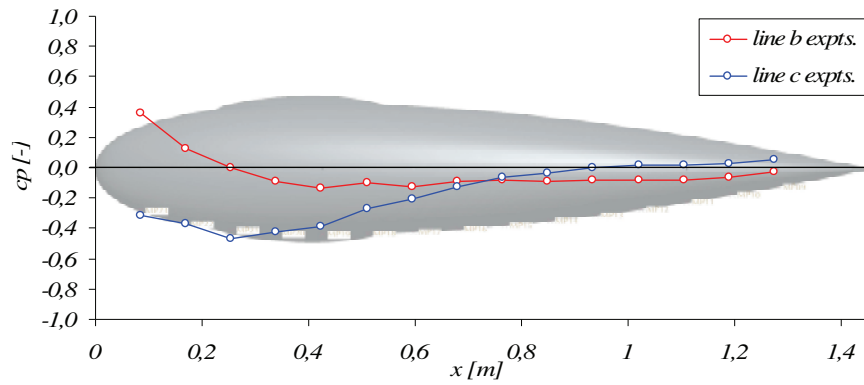
Figure 51: pressure coefficients along lines b and c for α=12,5° incident flow angle

A comprehensive survey of all measured pressure data for all flow angles is given in the appendix.

Figure 52 shows photographs of a wind tunnel test run, where the flow was visualized using a smoke lance. The upper two pictures refer to zero incident flow angle, where the flow follows the smooth contour very well. For the case of a non-zero incident flow angle, as it is shown in the lower two pictures, the flow field exhibits a separation zone on the lee side of the test body resulting in a larger wake area.
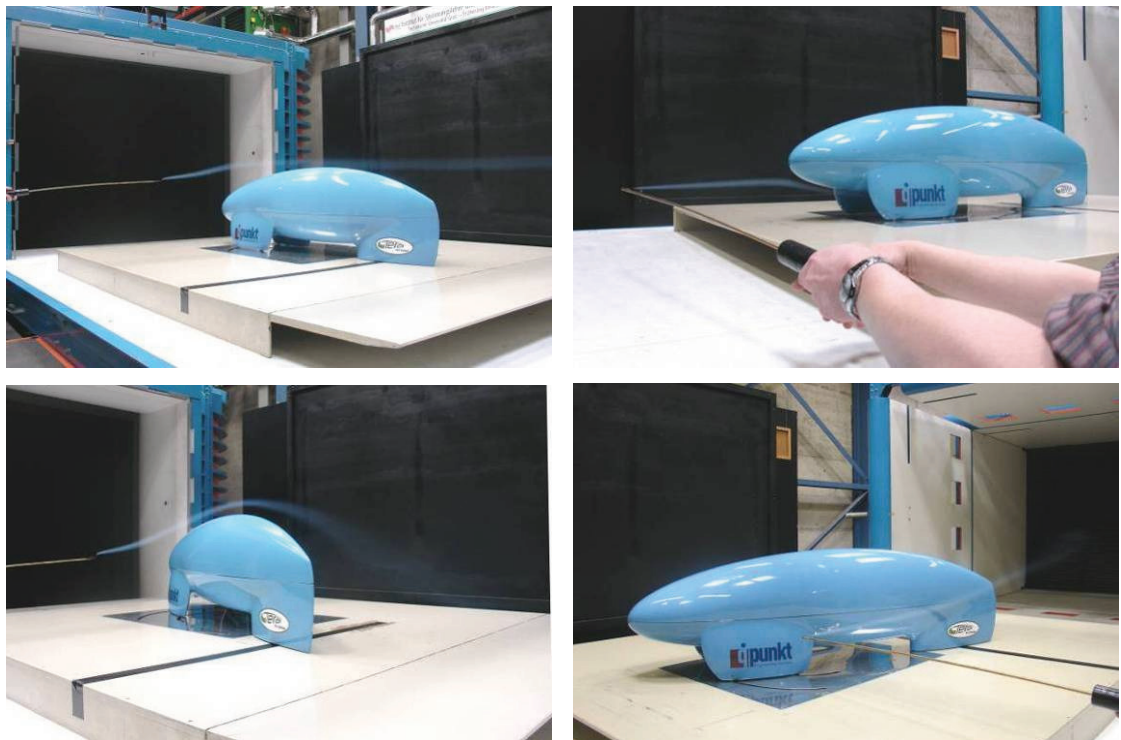
Figure 52: flow visualization using a smoke lance during the wind tunnel test runs for incident flow angles α=0° (upper subfigures), and α>0° (lower subfigures).

3.   Numerical Simulations

This section is devoted to the computational part of the present work. All simulations were carried out using the commercial software ANSYS FLUENT 6.3.26. The conservation equations governing the considered problem, their numerical solution, and the applied turbulence models will be out hired in the following subsections. A description of the boundary conditions, which have to be chosen to match the real conditions in the wind tunnel experiments as closely as possible, is presented as well.

3.1. Basic equations of fluid mechanics

The basic equations of fluid motion describe the conservation of mass, momentum and energy. Assuming isothermal flow, the conservation of energy can be disregarded, so that the flow is only governed by the differential balance equations of mass and momentum, generally termed Navier-Stokes equations.

Conservation of mass

The conservation principle follows the axiom:

"Mass cannot neither be generated nor destroyed."

This implies that the temporal change of mass inside a given volume has to be balanced by the mass fluxes across its surface. The corresponding balance equation reads in index notation

$$\frac{\partial \rho}{\partial t} + \frac{\partial}{\partial x_j}\left(\rho u_i u_j\right) = 0\,, \tag{3.1}$$

where ρ is the density, and u_i represents the component of the velocity vector into the direction x_i.

Conservation of momentum

The conservation of momentum basically represents Newton's second law stating the axiom:

"The time rate of change of the momentum of a body is equal to the sum of all applied surface and body forces."

The corresponding differential conservation equation reads

$$\frac{\partial(\rho u_i)}{\partial t} + \frac{\partial}{\partial x_j}(\rho u_i u_j) = -\frac{\partial p}{\partial x_i} + \rho f_i + \frac{\partial \tau_{ij}}{\partial x_j}, \tag{3.2}$$

where f_i is the body force per unit mass into the direction x_i, and τ_{ij} is the viscous stress tensor. The viscous stresses are induced by the deformation of the fluid elements in motion. In contrast to the static pressure p, they vanish, if the fluid is at test. Assuming a Newtonian fluid with constant dynamic viscosity μ, the viscous stress term is related the rate of deformation through

$$\tau_{ij} = 2\mu S_{ij} - \frac{2}{3}\mu\delta_{ij}S_{kk}. \tag{3.3}$$

The strain tensor occurring in Eq. (3.3) reads

$$S_{ij} = \frac{1}{2}\left(\frac{\partial u_i}{\partial x_j} + \frac{\partial u_j}{\partial x_i}\right) \tag{3.4}$$

Its trace represents the divergence of the velocity

$$S_{kk} = \frac{\partial u_k}{\partial x_k} = \frac{\partial u_1}{\partial x_1} + \frac{\partial u_2}{\partial x_2} + \frac{\partial u_3}{\partial x_3}, \tag{3.5}$$

which is zero in the present case of incompressible flow with constant density.

3.2. Turbulent flow regime

The flow field becomes unstable, once the inertial forces exceed a critical level relative to the level of the viscous forces, and a transition from laminar to turbulent flow occurs. The Reynolds number which is defined as the ratio of the inertial to the viscous forces is the determining non-dimensional parameter for this transition.

$$Re = \frac{u \cdot L}{\nu} \tag{3.6}$$

Accordingly, the considered flow field has to be regarded as turbulent, if the Reynolds number is beyond a critical value Re_{crit}. This is the case in the presently investigated aerodynamic flow.

In comparison to laminar flow the turbulent motion is highly irregular involving significant fluctuations in time and space. A direct numerical simulation of this unsteady three dimensional motion on all relevant scales is computationally too costly for the high Reynolds numbers typically met in aerodynamical flow. Due to this restriction, a statistical approach is mostly used. It is based on the so called Reynolds

decomposition, which splits the instantaneous flow variables into an averaged and a fluctuating component written as

$$u = \overline{u} + u', \ v = \overline{v} + v', \ w = \overline{w} + w', \ p = \overline{p} + p'. \tag{3.7}$$

The temporal fluctuations of the velocity components around their averages at a given point in a turbulent flow field are exemplarily shown in Figure 53.
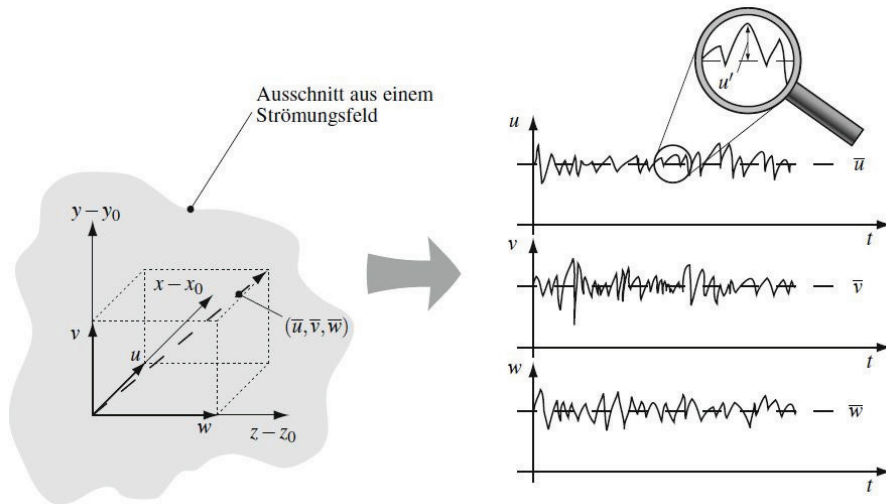
Figure 53: velocity components at a given point in a turbulent flow field (Herwig 2008)

Introducing the Reynolds decomposition, Eq. (3.7), into the Navier-Stokes equations gives the Reynolds Averaged Navier-Stokes (RANS) equations. For incompressible flow with constant density the RANS equations are written as

$$\frac{\partial}{\partial t}\left(\rho \overline{u_i}\right) + \frac{\partial}{\partial x_j}\left(\rho \overline{u_i u_j}\right) = -\frac{\partial \overline{p}}{\partial x_i} + \frac{\partial}{\partial x_j}\left[\mu \frac{\partial \overline{u_i}}{\partial x_j} - \rho \overline{u'_i u'_j}\right]. \tag{3.8}$$

In these equations six additional terms appear, the Reynolds stresses

$$\overline{u'_i u'_j} = \begin{pmatrix} \overline{u'^2} & \overline{u'v'} & \overline{u'w'} \\ \overline{u'v'} & \overline{v'^2} & \overline{v'w'} \\ \overline{u'w'} & \overline{v'w'} & \overline{w'^2} \end{pmatrix}. \tag{3.9}$$

To solve the RANS system of equations, turbulence models are necessary to provide the unclosed Reynolds stresses $\overline{u'_i u'_j}$.

3.3. *Turbulence modelling*

As mentioned above, turbulence models are necessary to close the RANS equations. Although a large number of different models has been developed and further refined during the last decades, there exists no model which has been proven as superior to all the others. As seen from Figure 54, two basic concepts of turbulence models can be distinguished: The Large Eddy Simulation method (LES), and the statistical model generally termed RANS models. The model-free approach of direct numerical simulation also shown in the chart, which resolves directly all relevant scales of turbulent motion, has to be discarded due to its prohibitively high computational costs.
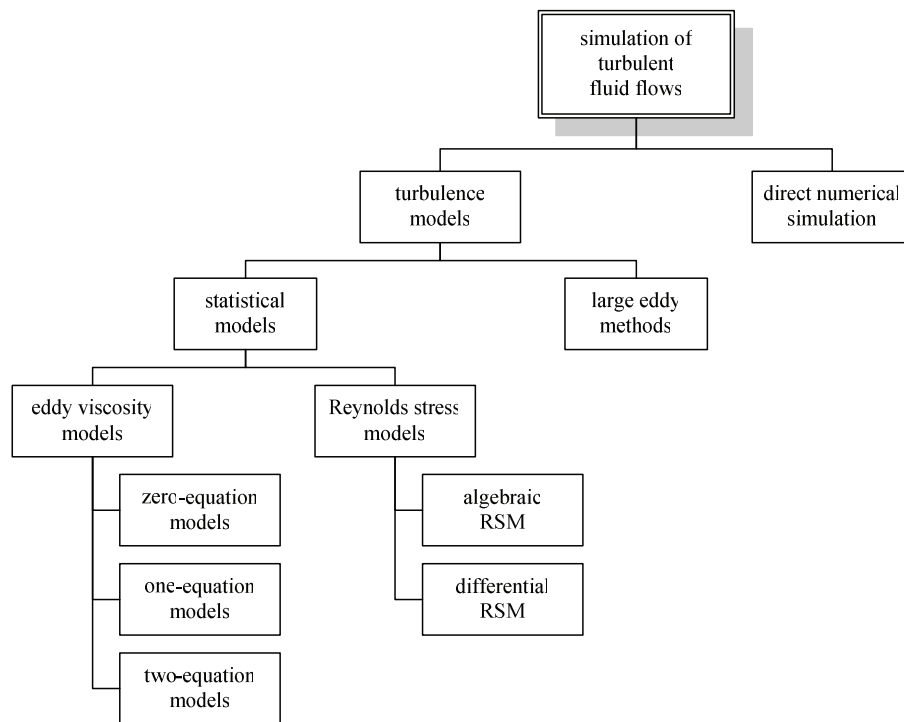
Figure 54: classification of turbulence models (Lücke 1997)

The statistical models can be further divided into two main groups: The eddy viscosity/diffusivity models (EVM), and the second moment closure models (SMC). The eddy viscosity models are based on the Boussinesq (1877) assumption that the turbulent stress tensor can be expressed in analogy to the molecular viscous stress of strain. The turbulent stress tensor can be accordingly written as

$$\tau_{ij}^t = -\rho \overline{u'_i u'_j} = -\frac{2}{3}\rho k \delta_{ij} + 2\mu_t \left(S_{ij} - \frac{1}{3}S_{kk}\delta_{ij} \right) \tag{3.10}$$

involving the eddy viscosity μ_t and the turbulent kinetic energy $k = \dfrac{\overline{u'_k u'_k}}{2}$. The second moment closure models solve a separate equation for each turbulent flux component. They are therefore more complex

and computationally more expensive than the eddy viscosity models. The modelling of the eddy viscosity models follows in principle the kinetic theory of gases, which states that the molecular viscosity of a fluid is proportional to the product of the molecular free path and the average speed of the molecules. In analogy to this molecular concept, the turbulent viscosity can be written as the product of the characteristic turbulent length scale and the velocity scale, representing the average size and velocity of the momentum transporting eddies. Based on this dimensional reasoning, the turbulent viscosity reads

$$\nu_t = \frac{\mu_t}{\rho} \sim \mathcal{L}\mathcal{U}, \tag{3.11}$$

where $\mathcal{L}$ is the turbulent length scale, and $\mathcal{U}$ is the velocity scale, which have both to be determined. The thus far proposed eddy viscosity models, in essence, differ in calculation of these turbulent scales. The so called zero-equation model calculates the turbulent viscosity only with algebraic correlations. All other eddy viscosity models, solve in general the transport equation for the turbulent kinetic energy k to provide the turbulent velocity scale obtained as

$$\mathcal{U}_{turb} \approx k^{1/2}. \tag{3.12}$$

The prescription of a physically sound wall boundary condition poses no problem for the solution of k. It an be shown that a zero gradient condition is consistent with the no-slip conditions to be satisfied at the wall. The remaining major problem comes with the determination of the turbulent length scale $\mathcal{L}_{turb}$. For the one-equation models, the turbulent length scale is calculated algebraically. A more advanced approach is the introduction of a second equation in addition to the k-equation to compute the turbulent length scale. These two-equation models use all the k-equation for the computation of the turbulent velocity scale, while the turbulent length scale is obtained from a second "scale-providing" differential transport equation. The most popular "scale-providing" quantity is the rate of turbulent energy dissipation, written as

$$\varepsilon = \nu \overline{\left(\frac{\partial u'}{\partial x_k}\right)\left(\frac{\partial u'}{\partial x_k}\right)}. \tag{3.13}$$

The transport equations for k and ε constitute together the k-ε turbulence model (Spalding 1972), where the turbulent length scale is obtained as

$$\mathcal{L}_{turb} = \frac{k^{3/2}}{\varepsilon}. \tag{3.14}$$

For the solution of the k- and ε-fields, free stream values for k and ε, or $\mathcal{L}$, have to be prescribed at the inflow boundary. At the wall the turbulent kinetic energy is zero, while the dissipation rate ε remains non-

zero and is unknown. This poses a severe problem to the k-ε model, and, as a consequence, the k-ε transport equations are not solved down to the wall. The near wall region is covered by wall functions, which provide the boundary conditions in the first near wall layer of computational cells, where the k-ε-equations are solved. The most common wall function is the logarithmic law of the wall.

The k-ε-turbulence model is the most popular turbulence model, which is well established and very well validated. The disadvantages are the poor performance in flows with large extra strains as met in curved boundary layers or unconfined flows. Especially the poor performance in flows with curved boundary layers called for alternative "scale providing" quantities, which allow for a better resolution of the near wall region. The characteristic frequency ω, which is defined as

$$\omega = \frac{\varepsilon}{k}, \tag{3.15}$$

represents such an alternative. Using this quantity the length scale is given by

$$\mathcal{L}_{turb} = \frac{\sqrt{k}}{\omega}. \tag{3.16}$$

The transport equations for k and ω constitute the k-ω turbulence model (Wilcox 1998). As already mentioned for the k-ε turbulence model k becomes zero at the wall, while ε remains non-zero. This implies an infinite characteristic frequency at the wall following from Eq. (3.15). However, this inconvenient singularity can be easily circumvented imposing a large value according to $\omega \sim 1/y^2$ at the first grid point. In contrast to the k-ε model the transport equations for k and ω can be integrated down to the viscous sublayer near the wall. The problem of the k-ω turbulence model is rather the free stream region, where the turbulence kinetic energy is small or even zero. In such a case the obtained solution tends to be very sensitive to the prescription of the, mostly unknown, value for ω at the inflow.

Among the two-equation eddy viscosity models, the k-ε and k-ω models are nowadays the most widely employed approaches in commercial simulations. To overcome the deficits of these two approaches mentioned above a combination of both concepts was developed and successfully applied to many aerodynamic external flow configurations. This so called SST-k-ω model, which was introduced by Menter (1994), was used in all RANS-type simulations of the present work. It is described in more detail in the following subsection.

3.3.1. SST-k-ω model

The SST-k-ω model, introduced by Menter (1994), combines the advantages of the k-ω model in the near wall region with the advantages of the k-ε model in the free stream region, while eliminating the deficits of the k-ω model in the free stream region and the deficits of the k-ε model in the near wall region. The

combination of the two models is realised by using a blending function. In Figure 55 the basic concept of the SST-k-ω model is visualized for the flow around an airfoil.
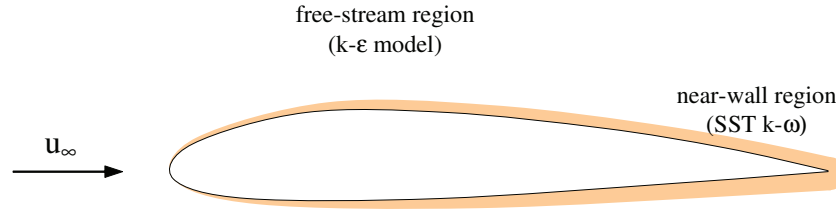
Figure 55: concept of SST-k-ω model

The blending between the two different models requires an appropriate blending function. Especially for complex flow geometries it is often hard to define such a function. A successful blending can sometimes require a lot of empiricism, which limit the general applicability of the blending functions. Many of these empirical functions strongly depend on the wall-distance. Despite this good deal of empiricism, the SST-k-ω model was proven to perform very well in various challenging flow conditions, including flows with adverse pressure gradients and separation.

The SST-k-ω model is a two-equation model, which solves for transport equation of the turbulent kinetic energy k written as

$$\frac{\partial \rho k}{\partial t} + \frac{\partial \left(\rho \overline{u_j} k \right)}{\partial x_j} = \tilde{P}_k - E_k + \frac{\partial}{\partial x_j} \left(\Gamma_k \frac{\partial k}{\partial x_j} \right),$$
(3.17)

and a transport equation for ω written as

$$\frac{\partial \rho \omega}{\partial t} + \frac{\partial \left(\rho \overline{u_j} \omega \right)}{\partial x_j} = \tilde{P}_\omega - E_\omega + \frac{\partial}{\partial x_j} \left(\Gamma_\omega \frac{\partial \omega}{\partial x_j} \right) + 2 \left(1 - F_1 \right) \rho \sigma_{\omega,2} \frac{1}{\omega} \frac{\partial k}{\partial x_j} \frac{\partial \omega}{\partial x_j}.$$
(3.18)

The first three terms on the right side of Eq. (3.17) and Eq. (3.18) represent production, dissipation and diffusion of k and ω, respectively. The last term on the right side of Eq. (3.18) represents a cross-diffusion term. This cross-diffusion term considers the blending between ω and ε dependent on the blending Function F_1. It is noted that the present formulation follows the formulation used by ANSYS FLUENT, where the specific dissipation rate ω is defined a little bit different from Eq. (3.15), being

$$\omega = \frac{\varepsilon}{C_\mu k} \text{ with } C_\mu = 0,09.$$
(3.19)

Γ_k and Γ_ω are the effective diffusivities of k and ω. They are written as

$$\Gamma_k = \mu + \frac{\mu_t}{\sigma_k}, \ \Gamma_\omega = \mu + \frac{\mu_t}{\sigma_\omega}, \quad (3.20)$$

where μ_t is the turbulent viscosity. σ_k and σ_ω are the turbulent Prandtl numbers written as

$$\sigma_k = \frac{1}{F_1/\sigma_{k,1} + (1-F_1)/\sigma_{k,2}}, \ \sigma_\omega = \frac{1}{F_1/\sigma_{\omega,1} + (1-F_1)/\sigma_{\omega,2}}. \quad (3.21)$$

involving the model constants $\sigma_{k,1}$, $\sigma_{k,2}$, $\sigma_{\omega,2}$, $\sigma_{\omega,2}$ given by

$$\sigma_{k,1} = 1,176, \ \sigma_{k,2} = 2,0, \ \sigma_{\omega,1} = 1,0, \ \sigma_{\omega,2} = 1,168.$$

The turbulent viscosity μ_t, representing the transport of momentum by the turbulent fluctuations is computed as follows:

$$\mu_t = \frac{\rho k}{\omega} \frac{1}{\max\left[\frac{1}{\alpha^*}, \frac{SF_2}{a_1\omega}\right]}. \quad (3.22)$$

Therein S is the magnitude of the strain rate, $a_1 = 0,31$ is a model constant, and α^* is a damping coefficient for the turbulent viscosity. It is computed from

$$\alpha^* = \alpha_\infty^* \left(\frac{\alpha_0^* + Re_t/Re_k}{1 + Re_t/Re_k} \right) \quad (3.23)$$

with

$$Re_t = \frac{\rho k}{\mu\omega}, \ Re_k = 6, \ \alpha_0^* = \frac{\beta_i}{3} \text{ and } \beta_i = 0,072. \quad (3.24)$$

The blending functions F_1 and F_2 are defined as follows:

$$F_1 = \tanh\left(\phi_1^4\right) \quad (3.25)$$

$$F_2 = \tanh\left(\phi_2^2\right) \quad (3.26)$$

The arguments ϕ_1 and ϕ_2 are computed from

$$\phi_1 = \min\left[\max\left(\frac{\sqrt{k}}{0,09\omega y}, \frac{500\mu}{\rho y^2 \omega} \right), \frac{4\rho k}{\sigma_{\omega,2} D_\omega^+ y^2} \right],$$ (3.27)

$$\phi_2 = \max\left[2\frac{\sqrt{k}}{0,09\omega y}, \frac{500\mu}{\rho y^2 \omega} \right],$$ (3.28)

where D_ω^+ is the positive portion of the cross diffusion term in Eq. (3.18).

As mentioned already for the k-ω model the inconvenient wall boundary condition $\omega = \infty$ in the first grid point is replaced by a variation for ω. In ANSYS FLUENT the value of ω at the wall is defined as follows

$$\omega_w = \frac{\rho \left(u^* \right)^2}{\mu} \omega^+,$$ (3.29)

where ω^+ is the asymptotic value of ω written in near wall coordinates at the first grid point near the wall. u* is the wall friction velocity, written as

$$u^* = \sqrt{\frac{\tau_w}{\rho}}.$$ (3.30)

If the viscous sublayer is fully resolved which is associated with the non-dimensional wall distance

$$y^+ = \frac{u^* y}{\nu} \approx 1,$$ (3.31)

the asymptotic value of ω^+ in the sublayer is given by

$$\omega^+ = \min\left(\omega_w^+, \frac{6}{\beta_i \left(y^+ \right)^2} \right),$$ (3.32)

where

$$\omega_w^+ = \begin{cases} \left(\frac{50}{k_s^+} \right)^2 & k_s^+ < 25 \\ \frac{100}{k_s^+} & k_s^+ \geq 25 \end{cases},$$ (3.33)

with

$$k_s^+ = \max\left(1.0, \frac{\rho k_s u^*}{\mu}\right) \tag{3.34}$$

involving the roughness height k_s.

3.3.2. Detached Eddy Simulation

The DES model is a hybrid model which combines a RANS type model with the method of Large Eddy Simulation. The basic concept of LES is that it solves directly for instantaneous motion of the large turbulent structures ("large eddies"), while it models the contribution of the small structures generally termed "subgrid scale" eddies. This approach appears to be as a very well suited for the simulation of separated flow, where large vortical structures emerge downstream of the separation point. LES has been proven to describe realistically the formation, convection and interaction of these large highly unstationary structures. In the near wall region the vortical structures become very small, which leads to prohibitively high resolution requirements and hence unbearable computational costs for LES. The hybrid approach of DES circumvents this problem by applying LES only in the free stream region, while it uses a RANS model, here in particular the SST-k-ω model, in the near wall region. The basic idea of DES is exemplarily illustrated in Figure 56 for a flow around an airfoil.
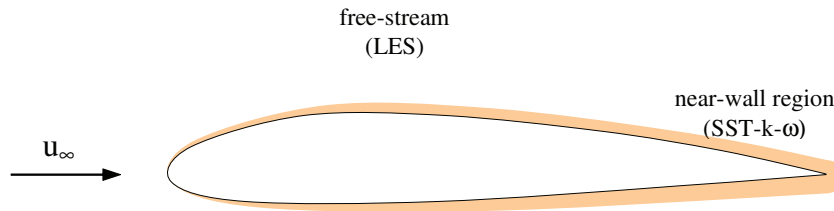
Figure 56: concept of Detached Eddy Simulation

In the presently used SST-k-ω based DES approach, the transition from SST-k-ω to LES is realized by modifying the dissipation of the turbulent kinetic energy in Eq. (3.17).

The modified term reads

$$\tilde{E}_k = \rho C_\mu k \omega F_{DES} \tag{3.35}$$

introducing the parameter

$$F_{DES} = \max\left(\frac{\mathcal{L}_t}{C_{DES}\Delta};1\right). \tag{3.36}$$

The modification is evidently activated dependent on the ratio of the turbulent length scale as defined in the SST-k-ω formulation

$$\mathcal{L}_t = \frac{\sqrt{k}}{C_\mu \omega} \tag{3.37}$$

and the local grid size obtained as $\Delta = \max(\Delta x, \Delta y, \Delta z)$. C_{DES} is a calibration constant set to $C_{DES}=0,61$. Using LES in the free stream region requires a three-dimensional unsteady simulation. This implies that the computational costs for DES are significantly higher to those of SST-k-ω, even if the same grid resolution can be used.

While the SST-k-ω turbulence model was used in all considered simulation cases, the application of DES was strongly restricted by its high computational costs. DES was therefore applied only to the case with zero incident flow angle $\alpha=0$, and a case with a very high angle, $\alpha=25°$, where significant flow separation was expected, and, hence, the DES was supposed to be superior to the SST-k-ω approach.

3.4. Numerical solution

The wind tunnel measurements provided a rich data base, from which the individual test cases were selected. The simulations considered in total six test cases with the free stream velocity $u_\infty=20m/s$, whose incident flow angle was varied from 0° to 25°. The main focus of the evaluation of the numerical results against the experiments was on the prediction of the drag. The spatial discretisation, the meshing strategy, the boundary conditions, and the solver settings, which were applied in the present simulations, shall be outlined in the following.

3.4.1. Discretisation in space

The Navier-Stokes equations, which govern the present aerodynamic flow cannot be solved analytically. Therefore, they have to be solved numerically based on a discretisation of the equations in time and space. The discretisation is associated with the definition of a numerical mesh, which specifies the position of all discrete nodal points, where the solution is computed. We can distinguish between two types of meshes. The first type are the structured meshes, where the grid lines can be regarded as lines of general coordinates. These lines need not to be orthogonal. They can be locally stretched or compressed as shown in Figure 57 a. The second group of meshes are the unstructured meshes. Their grid lines are not associated with general coordinate lines as seen from Figure 57 b. The advantages of unstructured meshes are that they are easier to generate and more flexible with respect to the geometry of the computational

domain. On the other hand, the numerical solution algorithm is in general mathematically more complex for unstructured grids, and strongly skewed grid cells can lead to high numerical errors.
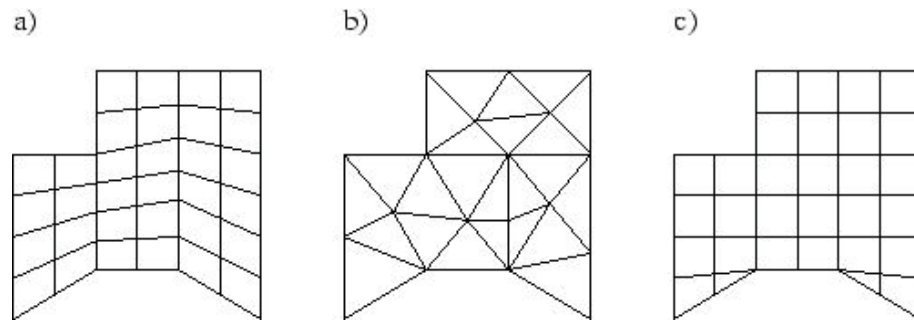
Figure 57: a) structured mesh, b) unstructured mesh, c) hybrid mesh

3.4.2. Grid generation

The first step was the specification of the geometry of the computational domain containing the test body and its surroundings. The surface of the test body representing the most important part of the wall boundaries of the domain was incorporated in terms of a triangulated approximation of the real contour, which had been exported by the CAD Software ProEngineer in stl-format. Based on the dimensions of the test section of the wind tunnel and the experience with previous simulations carried out at the company qpunkt GmbH (Drage 2008), the size of the computational domain was specified. The domain extends 24, 11.2 and 6.4 m into the streamwise, spanwise and vertical direction, respectively. The test vehicle is located 7,5 m downstream of the inlet. In addition, two refinement zones were defined in the near field of the test vehicle to increase locally the spatial resolution. Figure 58 shows the computational domain with the test body.
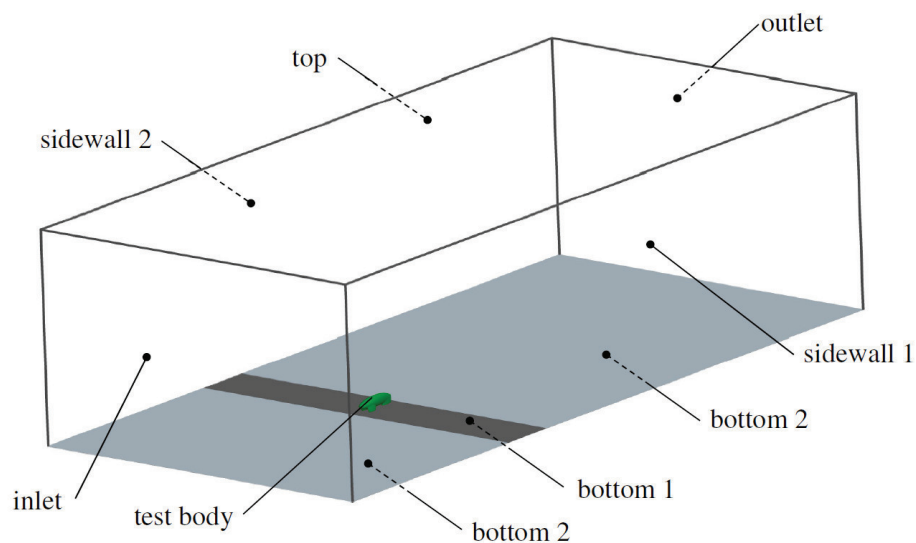
Figure 58: computational domain

The next step was the meshing of the computational domain. The first meshes were defined as coarse as possible heaving only to provide a sufficient resolution of the geometry of the test body. Figure 59 shows the meridional symmetry plane of the first coarse mesh with refinements at the rear end of the test body and without any refinements for the boundary layers. The base cell size of this coarse mesh is 0,15 m, and it consists of 628.216 cells.
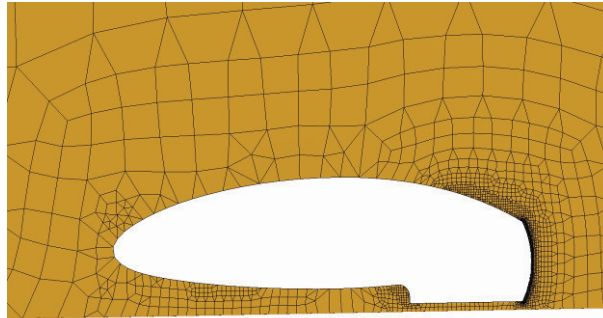
Figure 59: first coarse mesh

The first coarse mesh was then further refined in the region near the surface aiming at a sufficiently high spatial resolution in the wall boundary layer of the test body. Figure 60 shows the meridional symmetry plane of such a refined mesh providing an increased resolution of the wall boundary layers. It consists of 6.452.313 cells. The shown grid has in particular two refinement zones in the near field of the test body and a minimum cell size at the surface 0,001 m.
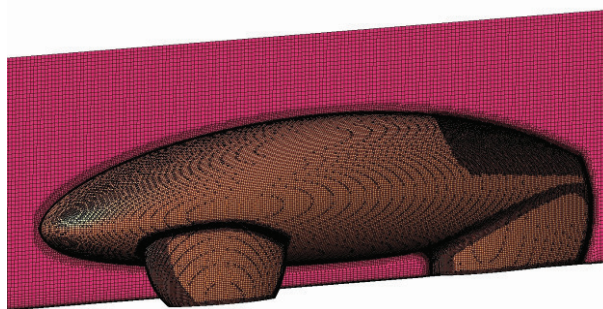
Figure 60: mesh with refinements and boundary layer

Using the SST-k-ω model requires to resolve the viscous sublayer near the wall. Therefore, the mesh in the wall boundary layer had to be further refined to ascertain that the normal distance of the first grid point in the wall coordinates is in the range of $y^+\approx 1$.

The software Spiderview was used as meshing tool. It offers the possibility to divide the boundary layer into several individual sub-layers with different levels of refinement. Figure 61 a exemplarily shows a near wall region which is divided into three sub-layers with different resolution. The so refined boundary layer grid is shown in Figure 61 b.
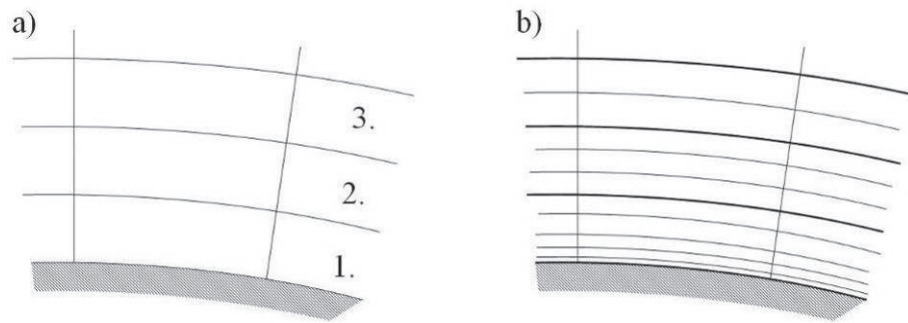
Figure 61: boundary layer grid

The finally used mesh, which satisfied the $y^+\approx1$ - criterion, as required by the near wall boundary conditions of the turbulence model, consists of about 16 million of grid cells. The contours of y^+ at the wall surface will be shown for the case with zero incident angle of the free stream velocity in section 4.

3.4.3. Boundary conditions

As seen from Figure 58, the computational domain exhibits eight boundary surfaces, where appropriate flow conditions have to be assumed. The individual types of boundary conditions, which have been imposed on these surfaces, are summarized in Table 6. A no-slip boundary condition, termed here "stationary wall", was used for the surface of the vehicle and the bottom area beneath denoted as "bottom 1" in Figure 58. The remaining part of the bottom surface denoted as "bottom 2" was prescribed as "moving wall" to avoid the formation of a boundary layer which would develop from the inlet, if a no-slip stationary wall boundary condition were used. A uniform free stream velocity profile is prescribed at the inlet, where α represents the angle of incidence relative to the inlet plane. The pressure was prescribed at the outlet plane. In the case of a free stream velocity with zero angle of incident (α=0), a symmetry boundary condition was applied at the top and both side walls. In the case of non-zero incident flow angle (α≠0) a velocity inlet was prescribed at the sidewall on the upwind side, while a pressure outlet condition was imposed at the sidewall on the downwind side. The specification of the side and top boundary conditions is no trivial task when dealing with external flow problems. For the case α=0°, the effect of using a moving wall boundary condition at the side and top surface as a reasonable alternative to the symmetry condition will be shown in the analysis of the computational results in section 4.1.

Table 6: imposed boundary conditions

boundary	boundary conditions	additional information
surface of test body	stationary wall	no-slip
inlet	velocity inlet	$u = u_\infty \cos(\alpha)$, $v = u_\infty \sin(\alpha)$
outlet	pressure outlet	reference ambient pressure = 0 Pa
sidewall 1 (upwind)	α=0: symmetry	-
	$\alpha\neq$0: velocity inlet	$u = u_\infty \cos(\alpha)$, $v = u_\infty \sin(\alpha)$
sidewall 2 (downwind)	α=0: symmetry	-
	$\alpha\neq$0: pressure outlet	reference ambient pressure = 0 Pa
top	symmetry	-
bottom 1	stationary wall	no-slip
bottom 2	moving wall	$u = u_\infty \cos(\alpha)$, $v = u_\infty \sin(\alpha)$

The presently used turbulence model, the SST-k-ω, requires to impose boundary conditions for k and ω. At the boundaries assigned with moving wall conditions a zero gradient condition is imposed for k and ω. At the stationary wall of the vehicle a zero-gradient condition is used for k, while the value obtained from the near wall function given in Eq. (3.29) is prescribed for ω. At the inflow boundary (velocity inlet), k and ω are prescribed in terms of the turbulence intensity

$$\mathrm{Tu} = \frac{1}{u_\infty} \sqrt{\frac{2}{3} k} \cdot 100 \ [\%] \,, \tag{3.38}$$

and the turbulent length scale

$$\mathcal{L}_t = \frac{\sqrt{k}}{C_\mu \omega} \,. \tag{3.39}$$

The turbulence intensity was prescribed based on hot wire measurements of the flow in the nozzle upstream of the test section carried out by Bair (1989). The turbulence intensity for different velocities u_∞ measured at the centre of the nozzle exit plane were already shown in Figure 30. Based on these data an average value of Tu=0,13% was prescribed. Since no measurements for the turbulent length scale were available, it was estimated using an expression proposed by Batchelor & Townsend (1948) written as

$$\mathcal{L}_t = \frac{\Delta_{mesh}}{9,5} \sqrt{\frac{x}{\Delta_{mesh}} - 10} \,. \tag{3.40}$$

Therein, x is the axial distance between the turbulence grid which is mounted in the plenum upstream of the nozzle and the leading edge of the test body. Δ_{mesh} denotes the mesh size of the turbulence grid in the plenum. With x = 6,7m and Δ_{mesh} = 0,1m, this expression yields $\mathcal{L}_t$= 0,0086m, which was imposed in the present simulations. The prescription of the turbulence quantities Tu and $\mathcal{L}_t$ at the inlet boundary has a significant effect in the computational results, as it will be shown in section 4.1.

3.4.4. Solver Settings

This section briefly describes the solver settings and the truncation criteria dependent on the residual values. Further the reference values for the non-dimensional force and moment coefficients are presented. ANSYS FLUENT offers three different types of solution algorithms. The pressure-based, the density-based implicit and the density-based explicit solver. The pressure-based solver solves the momentum equations first to obtain a prediction for the velocity field. In the second step, the Poisson equation is solved for the pressure, which is used to correct the predicted velocity field so that it satisfies the continuity equation. The density-based Solver solves the continuity, the momentum and energy equations simultaneously, implicitly or explicitly. The density-based solver is appropriate for compressible flows. For low speed aerodynamics like automotive aerodynamics, where the flow is incompressible, the pressure-based solver has to be selected. ANSYS FLUENT provides two methods for the evaluation of the gradients using the nodal values at the discrete grid points, the Green-Gauss, or the Least Squares cell-based gradient evaluation. The Green-Gauss Theorem states that the volumetric integral of the divergence over a given volume is equal to the surface integral of the fluxes across the boundary surfaces of the volume, shown in Figure 62.
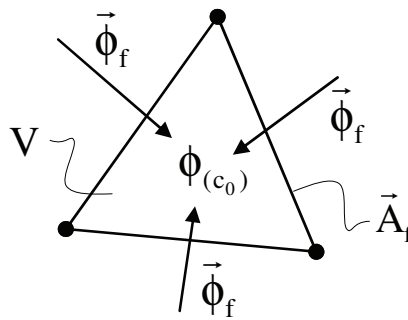
Figure 62: computational cell and face fluxes

Following the Green-Gauss theorem, the gradient of a scalar ϕ at the cell centre c_0 can be calculated from the fluxes across the cell faces written as

$$\left(\nabla\phi\right)_{c_0} = \frac{1}{V}\sum_f \bar{\phi}_f \vec{A}_f ,$$
(3.41)

where $\overline{\phi}_f$ are the averaged face values of ϕ, and V is the volume of the cell. $\overline{\phi}_f$ are calculated node-based or cell-based. The second method for the discrete computation of gradients is the Least Squares method.
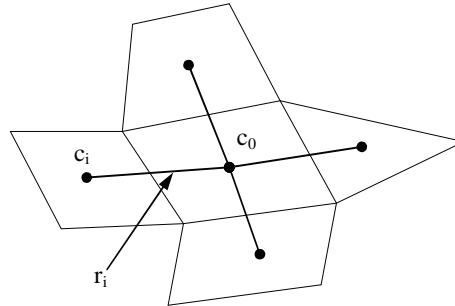
Figure 63: nodes of neighbouring cells

This method calculates the gradient at the cell centre assuming a linearily varying solution, such that

$$\left(\nabla\phi\right)_{c0} \Delta r_i = \left(\phi_{c_i} - \phi_{c_0}\right), \tag{3.42}$$

where ϕ_{c_i} and ϕ_{c_0} represent the nodal values of two neighbouring cells as shown in Figure 63. The Least Squares Method has the same accuracy for irregular, unstructured meshes as the node-based Green-Gauss method, but is less expensive computationally. Table 7 shows the main solver settings used in the present calculations.

Table 7: Solver Settings

Solver	Pressure-based
Formulation	Implicit
Velocity formulation	Absolute
Computation of gradients	Least Squares cell-based

The pressure-velocity coupling represents an important part of the pressure-based solver. It defines the numerical algorithm which provides a linear system of equations for the pressure (Poisson equation) by incorporating the continuity equation into the formulation to enforce the conservation of mass in the flux balances of the individual control volumes. ANSYS FLUENT offers several different algorithms of pressure-velocity coupling, SIMPLER, SIMPLEC, and the PISO method. Table 8 shows the presently selected pressure-velocity coupling as well as the discretisation shemes for the Poisson equation (pressure equation) and the solved transport equations.

Table 8: Solution Controls

Pressure Velocity Coupling	SIMPLE
Equations for:	Flow, Turbulence
Discretisation – Pressure	Standard
Discretisation – Momentum	First Order Upwind
Discretisation – turbulent kinetic Energy	Second Order Upwind
Discretisation – specific Dissipation Rate	Second Order Upwind

The flow field was initialized using the settings of the inlet boundary condition, but with zero velocity. To control the convergence of the solution, drag, lift and pitch moment and the pressures at four selected grid points were monitored. Two monitoring points for the pressure were located on the body surface and two in the wake of the test body. The monitored quantities were checked during the whole simulation to see how the solution converges. Figure 64 shows the typical trend of a monitored quantity. In this example the monitored quantity is the drag coefficient evolving with the number of iterations. The graph shows that the solution has almost converged already after 1000 iterations.
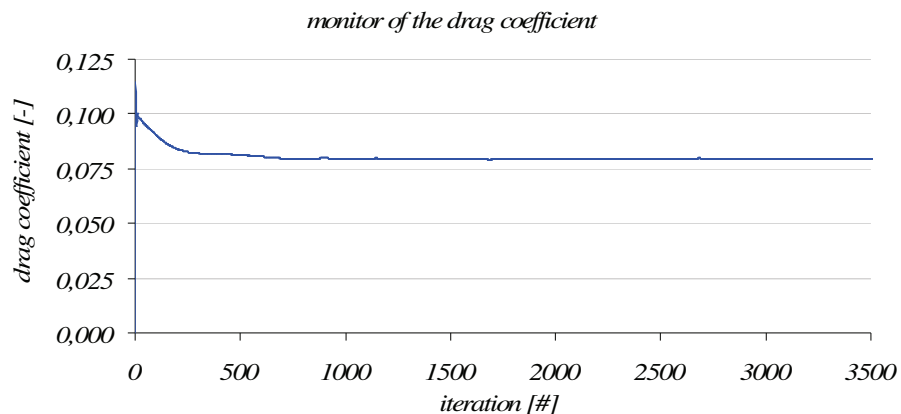
Figure 64: drag coefficient monitor

Unlike the stationary simulation with the SST-k-ω turbulence model, where a steady-state solution is iteratively approached until convergence is reached, the unsteady Detached Eddy Simulation has to integrate the instantaneous solution in time. With the Courant number (Courant 1928) or CFL number the time step could be calculated. The Courant number should be smaller than 1 for a stable simulation. The only remaining manipulable parameter in the definition of the Courant number is the time step, as the free stream velocity and the smallest cell size is given by the boundary conditions and the mesh. The stability criteria for the maximum time step size is given by the Courant-Friedrich-Levy condition

$$CFL = \frac{u_\infty \Delta t}{\Delta x} \overset{!}{\leq} 1 .$$

(3.43)

With the smallest cell size being Δx=1mm and the free stream velocity u_∞=20m/s the maximum time step size is Δt=5e-05s in the present simulations. The whole simulation time could be appreciated with the separation frequency of the eddies, first characterised by Vincent Strouhal (Strouhal 1878). Strouhal found out that the periodic separation of the flow around a body induces a noise with the frequency of the separating eddies. The non-dimensional parameter therefore is the Strouhal number. The total simulation time which is needed to analyze the statistics of the unsteady flow field can be estimated based on the Strouhal number

$$Sr = \frac{fl}{u_\infty},$$
(3.44)

where f is the separation frequency of the vortices shed from the downwind side, and l is the characteristic length of the immersed body. For many practical applications, the Strouhal number has values around 0,2. The determination of the characteristic length of the immersed body for a case with incident flow angle $\alpha>0°$ is shown in Figure 65. Assuming the certain value for the Strouhal number yield the time period $\tau_V = 1/f$ of vortex shedding. The total integration time of DES has to cover at least a couple of these vortex shedding periods τ_V to provide a converged statistics.
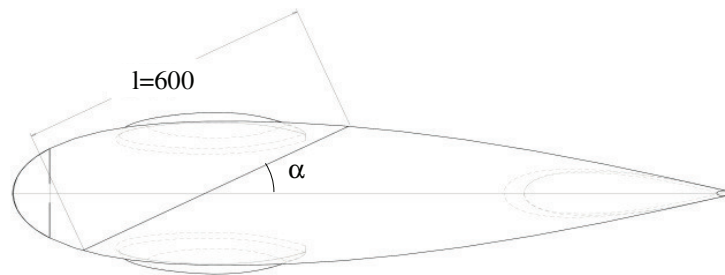
Figure 65: characteristic length for the calculation of the Strouhal number; incident flow angle α=25°.

The reference values which were used to calculate the non-dimensional force, momentum and pressure coefficients are summarized in Table 9.

Table 9: reference values

Projected frontal area of the body $A_{proj.}$ [m²]	0,0974624
Length of the body L [m]	1,445
Density ρ [kg/m³]	1,225
Pressure p_∞ [Pa]	0
Velocity u_∞ [m/s]	20

4. Analysis

As a first task of the analysis of the numerical results, the reliability of the numerical setup was assessed. This included a sensitivity analysis of the spatial resolution to single out a reliable and computationally feasible computational grid. Moreover, the actually imposed inflow and lateral boundary conditions were examined, if they reflect the real flow conditions in the wind tunnel realistically. The numerical setup which yielded the best results for the test case with zero incident flow angle was further used in all other test cases. After a comprehensive comparison of the numerical results obtained for the individual incident flow angles against the corresponding experimental data, the decomposition of the predicted total aerodynamic forces into the pressure and viscous components is discussed in detail. Providing insight into the individual contributions to the total forces the present CFD approach is proven as a powerful tool to analyze and optimize the aerodynamics of the considered vehicle.

4.1. Sensitivity to computational grid and boundary conditions

The sensitivity analysis was carried out for a zero incident flow angle in order to find most appropriate settings for the turbulence parameters at the inflow boundaries, for the far field conditions at the lateral boundaries, as well as a sufficient spatial resolution of the boundary layer near the surface of the vehicle. The SST-k-ω model was used as turbulence model. The different settings were evaluated based on the accuracy of the predictions for the drag coefficient and the lift coefficient. Table 10 lists all examined settings used for the simulations at zero incident flow angle together with the drag and the lift coefficients, which they produced.

Table 10: examined settings for grid resolution, turbulent inflow parameters and lateral boundary conditions, and predicted force coefficients.

case name	number of cells	wall boundary sublayers	turbulence intensity at inflow	turbulent length scale at inflow	lateral far field boundary condition	drag coefficient c_W	lift coefficient c_A
	[#]	[#]	[%]	[m]		[-]	[-]
wind tunnel measurement						0,075830	0,147892
100412	8.263.926	15	1	0,02	moving wall	0,098091	0,188025
100414	13.384.904	15	1	0,02	moving wall	0,095966	0,193526
100511	13.775.869	17	1	0,02	moving wall	0,098090	0,188030
100517	13.775.896	17	0,13	0,03	moving wall	0,079507	0,398711
100531	15.735.777	18	0,13	0,0086	moving wall	0,077162	0,219676
100707	15.735.777	18	0,13	0,0086	symmetry	0,079919	0,169350

The grid quality has next to the turbulence inflow parameters a great impact on the drag coefficient. The SST-k-ω turbulence model requires the wall coordinate of the first grid point near the wall to be about $y^+ \approx 1$. This requirement could only be satisfied by a strongly refined mesh in the boundary layer. The contours in Figure 66 show the difference between the simulation on the coarsest mesh, where wall y^+ values greater than 5 appear in large regions of the coarse grid solution. In contrast, the simulation results obtained with the locally most refined mesh exhibit wall y^+ values always below 1,5. This finally used grid has about 16 Mio cells and 18 refined sub-layers near the wall. A plot of this grid was already shown in Figure 60.

a)   b)
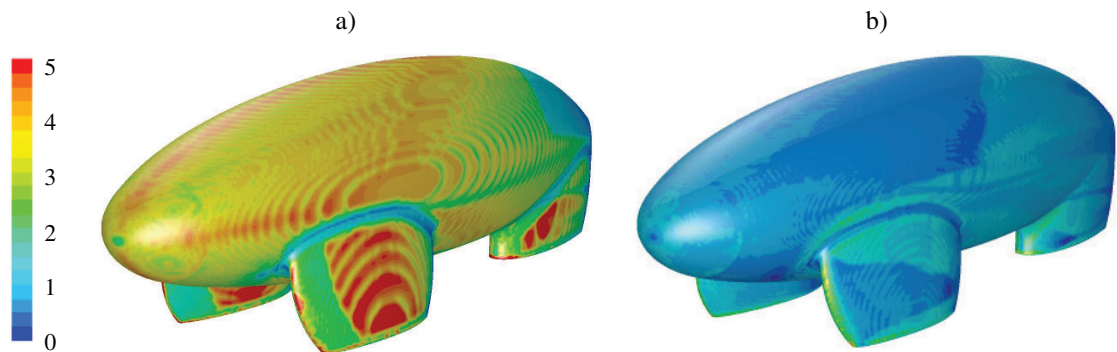
Figure 66: contours of wall y^+ for a) simulation 100412 (coarsest grid) and b) simulation 100707 (finest grid).

As the first grid point near the wall is located well within the viscous sub-layers ($y^+ \approx 1$), it has to be ensured that the characteristic near wall peak of the turbulent kinetic energy is sufficiently resolved. As exemplarily shown in Figure 67, a sufficient number of grid points are nested close to the wall to capture the strong local change in k. The strong variation of k is evidently well resolved on the near wall refined grid which is used in all present simulations.

As seen from Table 10, the prescription of the turbulence intensity and the turbulent length scale at the inflow were also shown to have a significant influence on the predictions. Applying the usual settings for external automobile aerodynamics of 1% turbulence intensity and 0,02m turbulent length scale (used in the standard workflow by the company qpunkt GmbH), the drag coefficient was considerably overpredicted. Changing the turbulence intensity from the firstly adopted standard value Tu = 1% to Tu = 0,13%, which represents the previously measured value at the nozzle of the wind tunnel at the Institute of Fluid Mechanics and Heat Transfer (see also Figure 30), improved significantly the prediction for the drag coefficient. No wind tunnel measurements were available for the turbulent length scale. The firstly assumed turbulent length scale $\mathcal{L}_t = 0,02$m lead to considerably stronger deviations from the experiment than the estimate $\mathcal{L}_t = 0,0086$m obtained from the correlation (3.40) by Batchelor and Townsend (1948).

turbulent kinetic energy distribution at the wall
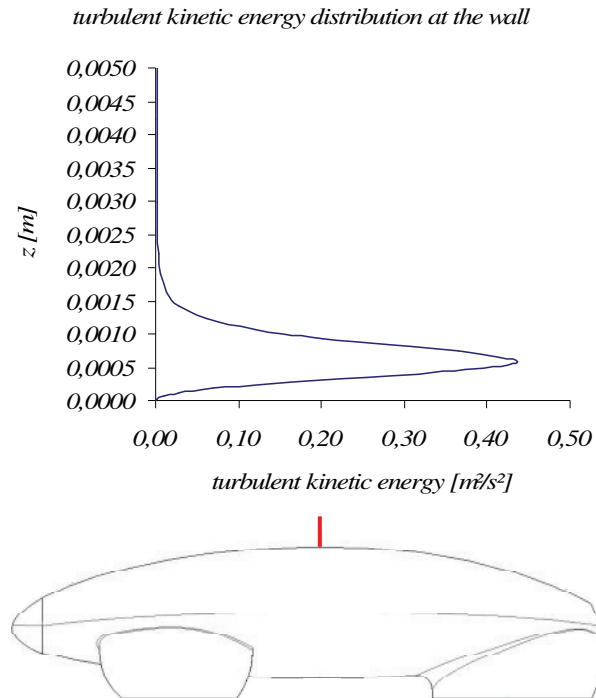
Figure 67: turbulent kinetic energy vs. normal distance to the wall at the position marked by the red line in the lower sketch of the body.

Figures 68 through 70 show contours of the local skin friction coefficients obtained for different settings of turbulence intensity and turbulent length scale. The skin friction coefficient basically represents the non-dimensional local wall shear stress τ_w written as

$$c_f = \frac{\tau_w}{\frac{\rho}{2} u_\infty^{\;2}} \; . \tag{4.1}$$

It becomes evident that the higher turbulence intensity imposed at the inflow produces generally higher values of c_f, which finally leads to a considerable overprediction for the drag coefficient. The turbulent length scale appears to have less influence on the drag. It, however, has a high impact on the predicted lift forces as seen from c_A in Table 10.
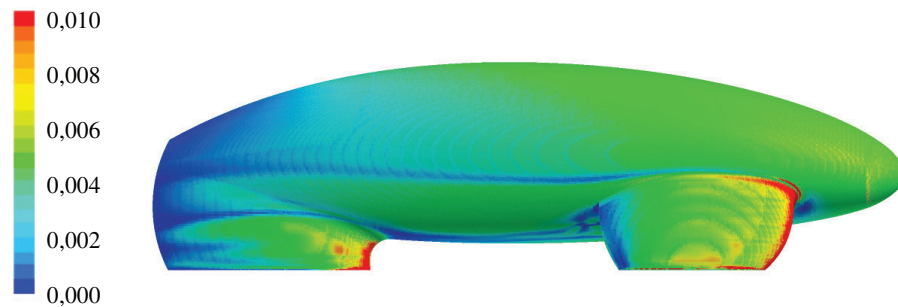
Figure 68: Contours of the skin friction coefficient for Tu = 1% and $\mathcal{L}_t$ = 0,02m (simulation 100412)
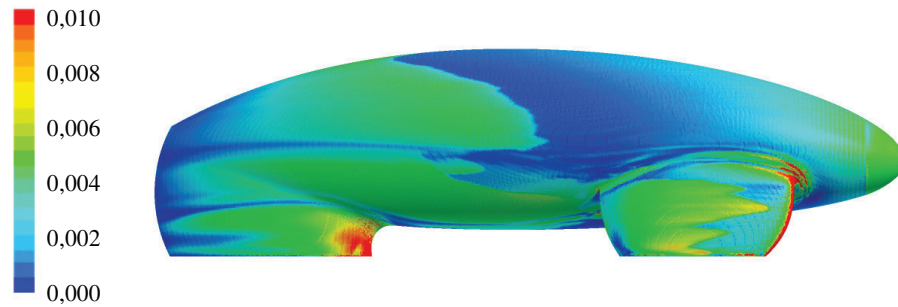
Figure 69: Contours of the skin friction coefficient for Tu = 0,13% and $\mathcal{L}_t$ = 0,03m (simulation 100517)
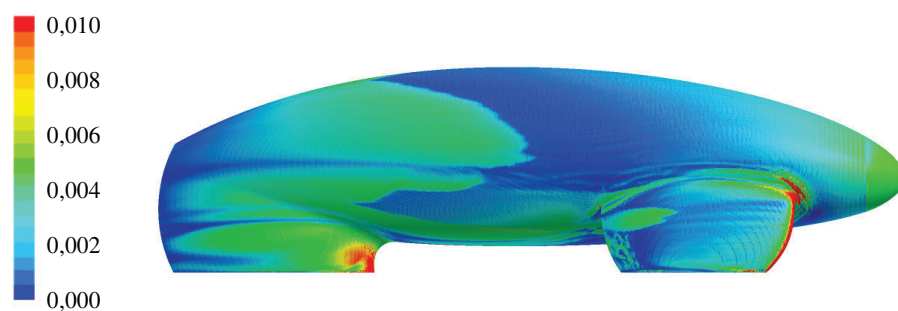
Figure 70: Contours of the skin friction coefficient for Tu = 0,13% and $\mathcal{L}_t$ = 0,0086m (simulation 100531)

Due to the slender airfoil-like geometry of the vehicle, the resulting aerodynamic pressure forces are very small in the case of zero incident flow angle α=0°. Therefore, already small disturbances originating from the lateral far field can have an influence on the pressure induced forces and moments. While the major part of the total drag is due to the action of viscous skin friction, the major part of the total lift force is due to the pressure acting on the surface. Thus, the lift results in principle from the pressure difference between the upper and the lower side of the test body.

Figure 71 exemplarily shows the variation of the pressure coefficient, along the upper and the lower meridian lines on the surface.
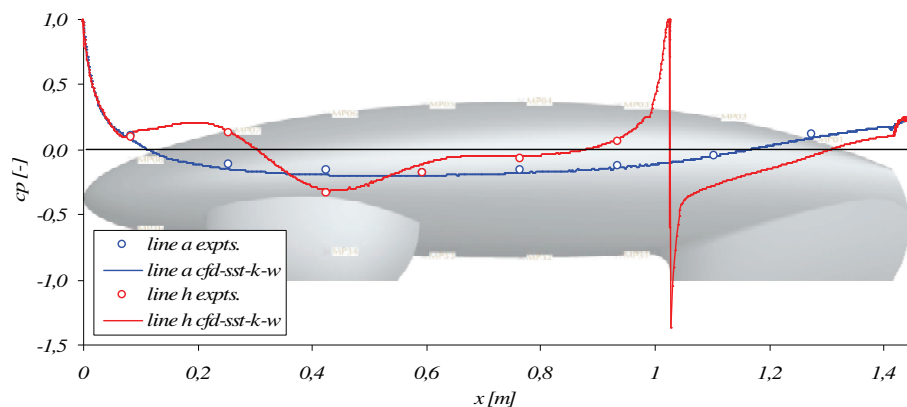
Figure 71: Variation of the pressure coefficient along the upper and the lower part of the test body

The pressure difference predicted by the simulation is evidently somewhat smaller than in the experiments. A closer analysis of these discrepancies unveiled a significant influence of the prescription for the lateral boundary conditions. The upper and lateral far field boundary is constituted by the sidewalls and the top wall of the computational domain. These boundary surfaces were first assumed as walls moving at the incident (free stream) velocity. This moving wall boundary condition basically imposes a zero orthogonal velocity component at the boundary, which forces the streamlines to align with the planar side and top boundary surfaces. This may lead a small unphysical acceleration of the flow near the boundary causing a slight decrease in the static pressure. To avoid such an unphysical change of the pressure in the far field, a symmetry boundary condition was assumed as an alternative.

Figure 72 shows the variation of the pressure coefficient along the upper meridional line (line a in Figure 47) of the test body. Both, the symmetry and the moving wall boundaries show slightly smaller values than the measurements. The pressure coefficients along the lower meridional line (line h in Figure 47) of the body shown in Figure 73, exhibit overpredictions for the moving wall boundaries which lie mostly above the values obtained with the symmetry boundary conditions. Only in the region next to the stagnation point of the rear wheel case, the predictions obtained with the symmetry boundaries are higher. Since the lift coefficient basically depends on the pressure difference between the upper and the lower part of the test body, the difference of the coefficients between the upper and the lower meridional lines is shown in Figure 74. It becomes evident that the pressure difference for the moving wall boundaries is generally greater than the pressure difference for the symmetry boundary conditions. This results in a considerable overprediction for the lift coefficient for the moving wall boundaries, while the prediction obtained with the symmetry boundary conditions shows a smaller deviation from the experiments, as seen from the predicted c_A-values in Table 10 on page 54.
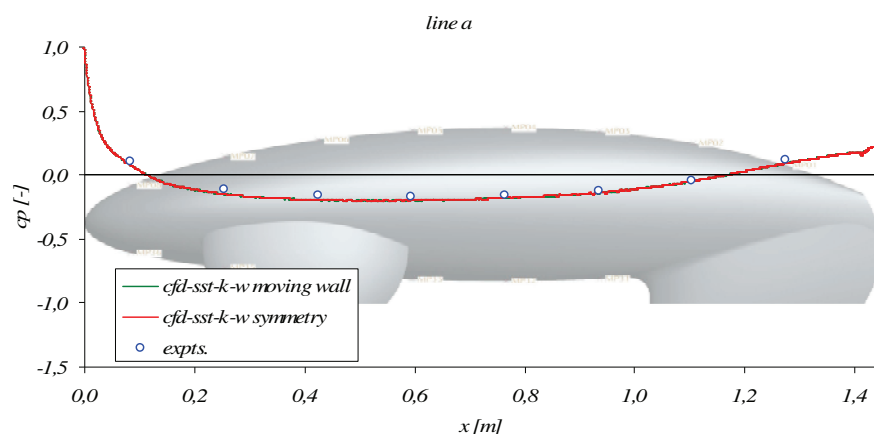
Figure 72: Variation of the pressure coefficient along the upper meridional line of the test body (line a)
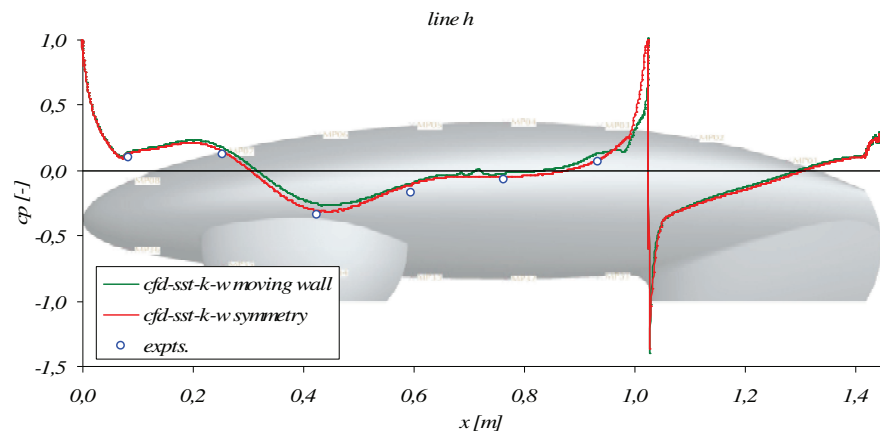
Figure 73: Variation of the pressure coefficient along the lower meridional line of the test body (line h)
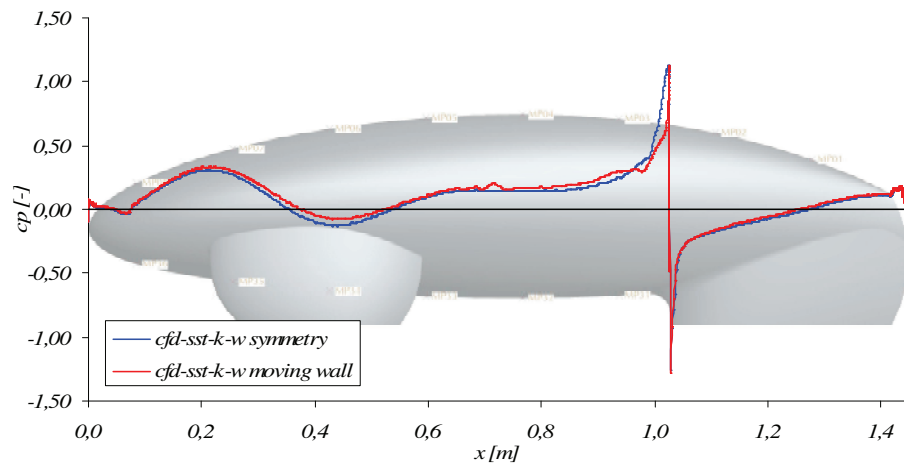
Figure 74: Variation of the pressure coefficient difference between the upper and the lower meridional lines of the test body for moving wall and symmetry boundary conditions.

Based on the analysis discussed above, the computational grid and some very essential settings for the boundary conditions were determined. The size of the chosen grid, the chosen parameters and boundary conditions are summarized in Table 11. The computational setup was kept the same in all simulations.

Table 11: Grid size, turbulent inflow parameters and far field boundary condition

Number of cells [#]	15.735.777
Boundary layer [#]	18
Turbulence intensity [%]	0,13
Turbulent length scale [m]	0,0086
lateral far field boundary condition	Symmetry

4.2. Results for varying incident flow angles

All numerical simulations assumed the same magnitude of incident (free stream) velocity $u_\infty = 20$m/s, which corresponds to a Reynolds number

$$\text{Re} = \frac{u_\infty L}{\nu} = \frac{20 \cdot 1,445}{1,46 \cdot 10^{-5}} = 1,98 \cdot 10^6 .\tag{4.2}$$

The angle of the incident flow was varied within 0° and 25°. The individual simulated cases are listed in Table 12. This section shows the most important results of the numerical simulations. Detailed data for every single numerical simulation are given in the appendix.

Table 12: Numerical simulations for different incident flow angles

case name	incident flow angle [°]	turbulence model
100707	0,0	SST-k-ω
100714	5,0	SST-k-ω
100622	10,0	SST-k-ω
100712	15,0	SST-k-ω
100729	20,0	SST-k-ω
100702	25,0	SST-k-ω
100805	0,0	DES
100812	25,0	DES

The SST-k-ω model was used as a base model for the turbulence, and it was applied for all incident flow angles. A Detached Eddy Simulation (DES) was carried out only for the smallest and the largest flow angles, $\alpha = 0°$ and $\alpha = 25°$, respectively. The main reasons for the restricted application of DES are the very high computational costs of this approach as compared to the RANS-type SST-k-ω approach. It was therefore decided to carry out a DES only for two cases with the minimum and maximum incident flow angle, $\alpha = 0°$ and $\alpha = 25°$, respectively. In the case with $\alpha = 0°$ the effect of flow separation is expected to be very small, so that DES and the SST-k-ω model should essentially yield the same results. In the case with $\alpha = 25°$, where flow separation is supposed to be of great importance, the predictions of the DES should be more accurate. The high computational costs of DES is due to the fact that it solves for the instationary equations of motion. As such the simulation has to cover several periods of vortex shedding to obtain converged statistics. The period of vortex shedding τ_v can be estimated as the inverse of vortex shedding frequency f occurring in the Strouhal number

$$Sr = \frac{fl}{u_\infty}. \tag{4.3}$$

Setting the velocity to $u_\infty = 20m/s$ and the characteristic length scale to $l = 0,6m$, and assuming $Sr = 0,2$ gives

$$\tau_v = \frac{1}{f} = 0,15s. \tag{4.4}$$

The time step size based on the CFL criterion is $\Delta t = 5 \ 10^{-5}s$, so that

$$n_v = \frac{\tau_v}{\Delta t} = 3000 \tag{4.5}$$

time steps are needed for one period of vortex shedding. In the multiprocessing environment (16 CPUs), which was used for the present simulations, the CPU time per time step was approximately $\Delta t_{wall} \approx 1min$. This implies a total computational time of more than five days to cover two periods of vortex shedding, where the initial time span which is needed to reach a statistically steady state, is not even included.

To control the statistical convergence of the unsteady solution, the temporal evolutions of the instantaneous drag, lift and pitch moment coefficients were monitored. The instantaneous pressure obtained at a selected point in the wake region was monitored as well. The evolutions monitored in the DES for $\alpha=25°$ are shown in Figure 75 through Figure 78. The red horizontal lines denotes the time span for averaging the flow statistics.
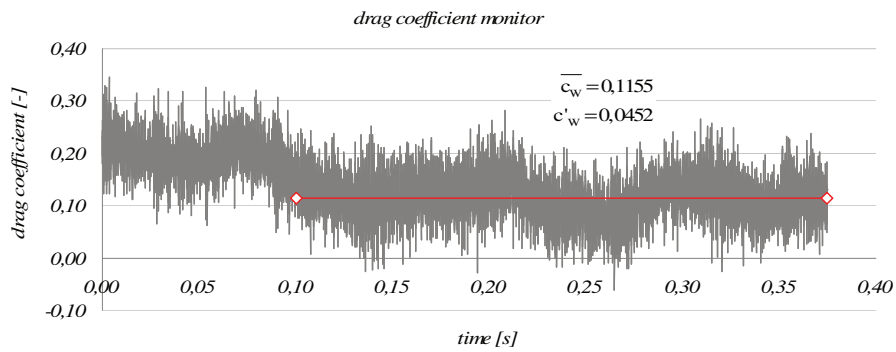
Figure 75: drag coefficient monitor of Detached Eddy Simulation for incident flow angle of 25°
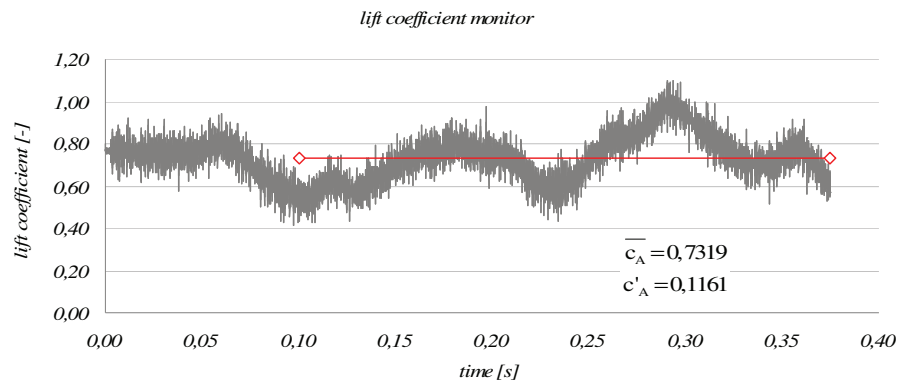
Figure 76: lift coefficient monitor of Detached Eddy Simulation for incident flow angle of 25°
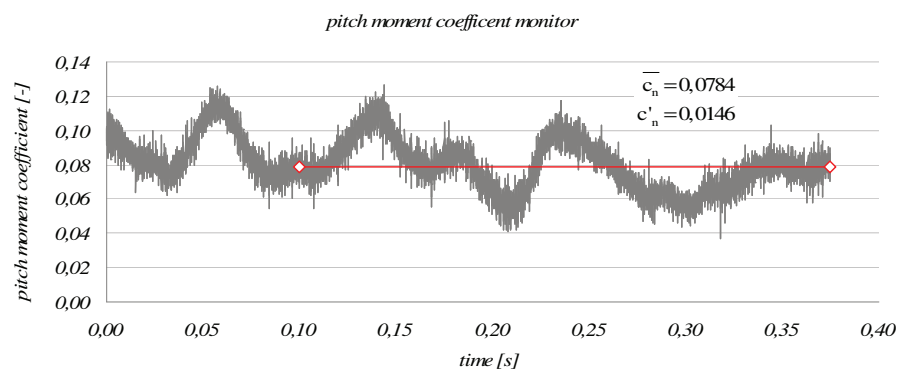
Figure 77: pitch moment coefficient monitor of Detached Eddy Simulation for incident flow angle of 25°
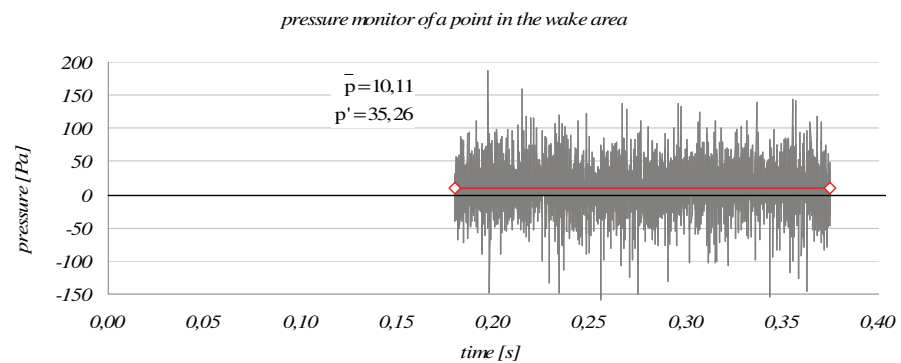
Figure 78: pressure monitor in the wake area of the Detached Eddy Simulation for incident flow angle of 25°

The following discussion of the numerical results for each incident flow angle always starts with a comparison of the predicted variations of the pressure coefficient along the left and the right equatorial lines of the main body (see Figure 28, lines b and c). In addition to this quantitative evaluation, contours of the magnitude of the velocities are displayed on two horizontal planes. On these planes, located at $z = 0,19m$ and $z = 0,05m$, the flow separation expected at the higher incident flow angles shall be well visible. To illustrate the variation of the turbulence intensity in the wake region of the test body, contours

of the turbulent kinetic energy are displayed on different planes across the test body. The predictions of the force and momentum coefficients are compared against the measurements at the end of this section.

Incident flow angle $\alpha = 0°$:

The case with $\alpha=0°$ was served as a reference test case for the evaluation of the used computational settings and the grid quality. The results relevant for this evaluation have already been discussed in the previous subsection 4.1. The following analysis also includes a comparison of the results obtained with SST-k-ω with those of the Detached Eddy Simulation, which was carried out for this test case as well. Figure 79 shows the comparison of the pressure coefficient $c_p = (p - p_\infty)/(\rho u_\infty^2/2)$ obtained along the left equatorial line of the mainbody (see line b in Figure 28). The open triangles denote the time averaged values obtained with DES, the error bars indicate the standard deviations from the mean values. The results of both turbulence models are in good agreement with the experiments except in the region near the front wheel casings, where DES shows somewhat underpredicted c_p-values.
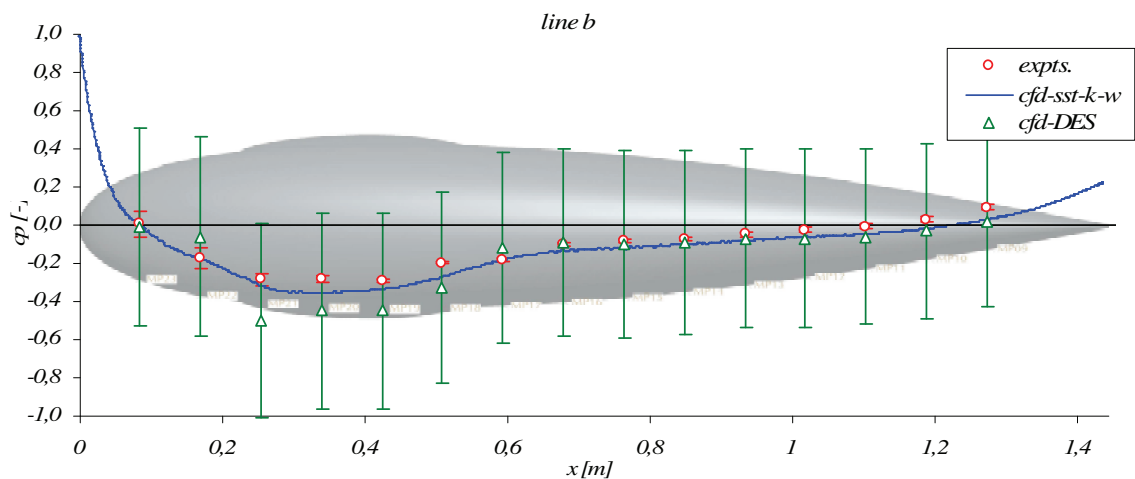
Figure 79: pressure coefficient for zero incident flow angle $\alpha = 0°$ along equatorial line b.

The contours of the turbulent kinetic energy shown in Figure 80 indicate that the SST-k-ω turbulence model produces a little bit more turbulence in the boundary layer than the Detached Eddy Simulation. This effect is especially visible at the upper edges of the front wheel casings, where the SST-k-ω contours exhibit some small amounts of turbulent kinetic energy, while there is nothing visible for the contours of turbulent kinetic energy for the DES simulation. As expected, no separation is observed for the $\alpha = 0°$ flow, neither in the SST-k-ω nor in the DES results.
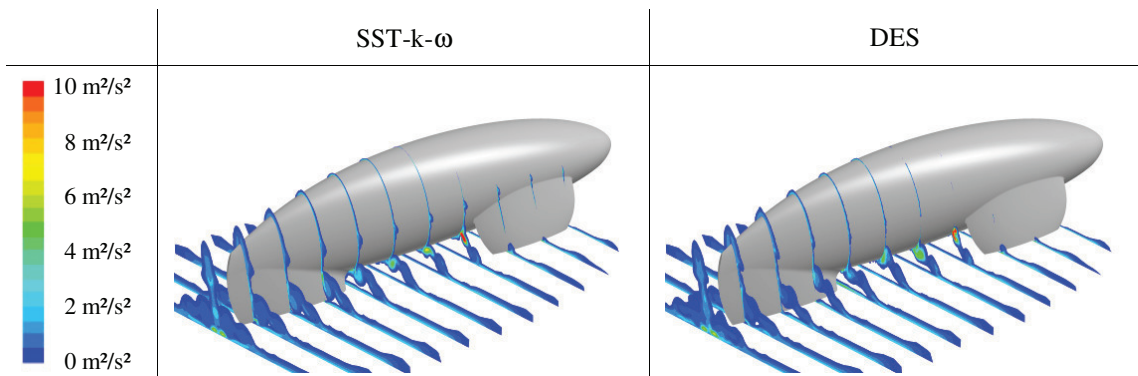
Figure 80: contours of the turbulent kinetic energy in m²/s² for incident flow angle α = 0°

Figure 81 show as a comparison velocity contours at two horizontal cutting planes. As there is no separation for the zero incident flow angle, the structure of the shown time averaged velocity fields do not differ notably.
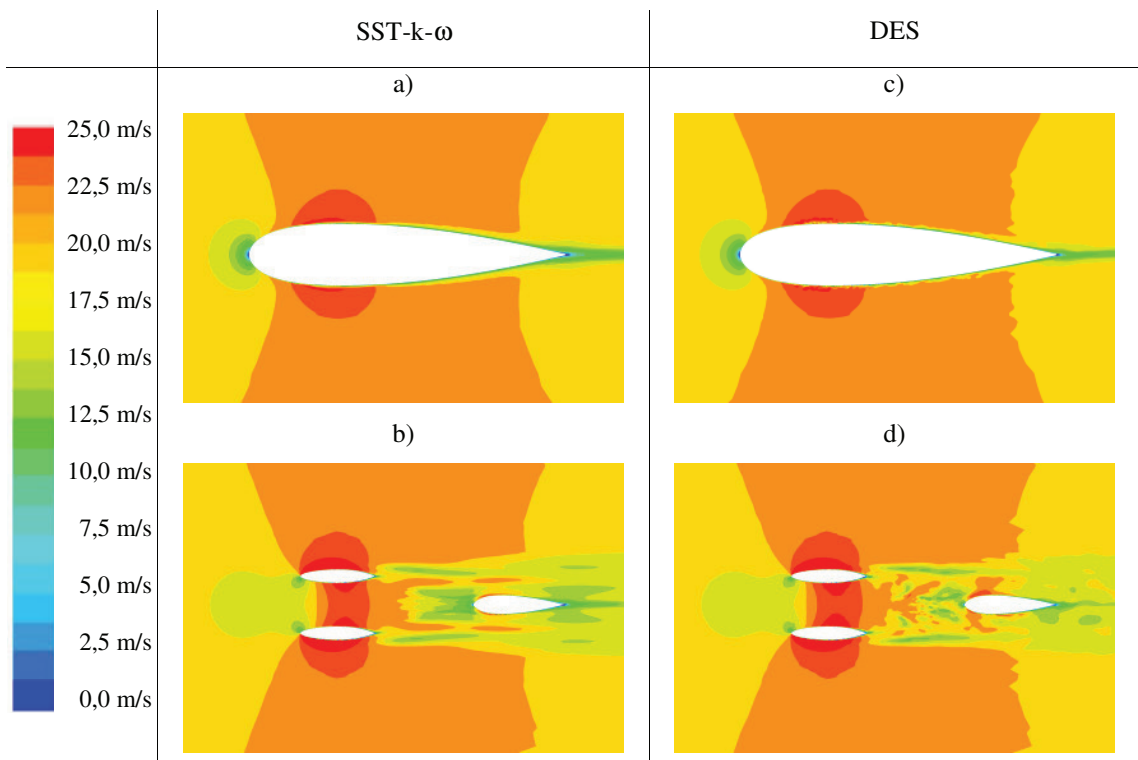
Figure 81: velocity contours in m/s for zero incident flow angle α=0° on horizontal planes a), c) at z=0,19m, and b), d) at z=0,05m, respectively.

Incident flow angle α = 5°:

Figure 82 shows the pressure coefficients on the upwind (line b) and the downwind side (line c) for an incident flow angle of 5°. Alike for α=0°, there is no notable separation occurring in this case as well, and the simulation and measurements are in good agreement.
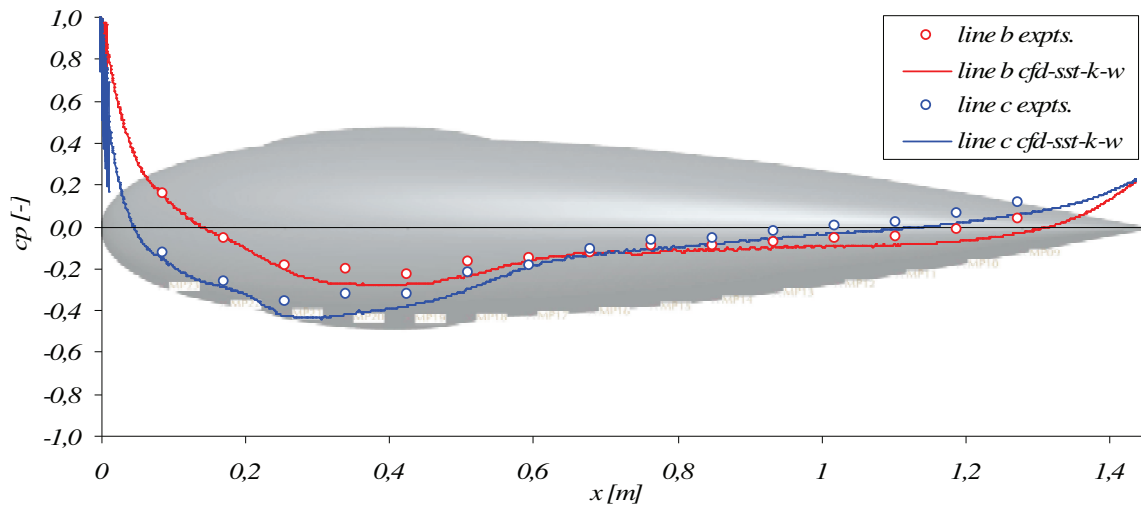
Figure 82: pressure coefficient for α = 5° on upwind (line b) and downwind side (line c).

The contours of velocity magnitude are visualized in Figure 83 on two horizontal planes. It becomes evident that there is no separation for the small incident flow angle of 5 degrees.
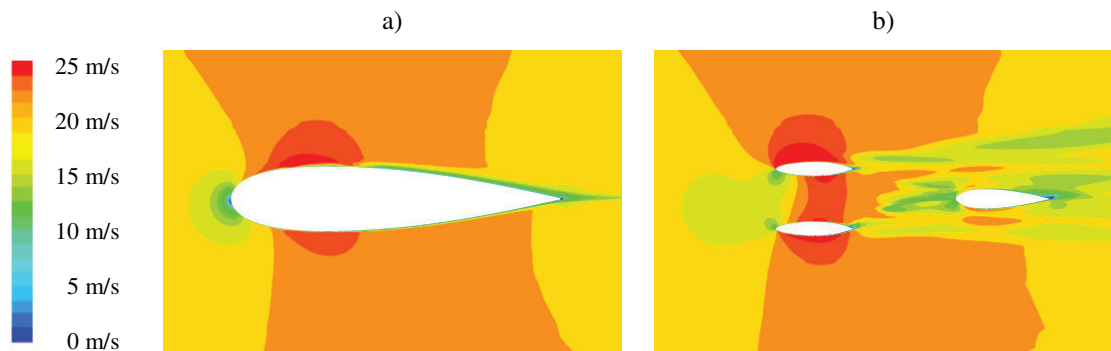
Figure 83: contours of velocity magnitude in m/s for α=5° on horizontal planes, a) at z=0,19m, and b) at z=0,05m.

The contours of the turbulent kinetic energy are plotted in Figure 84 on the upwind and downwind side. As compared to the case with α=0°, the region with notable turbulent kinetic energy has a somewhat larger lateral extension on the downwind side.
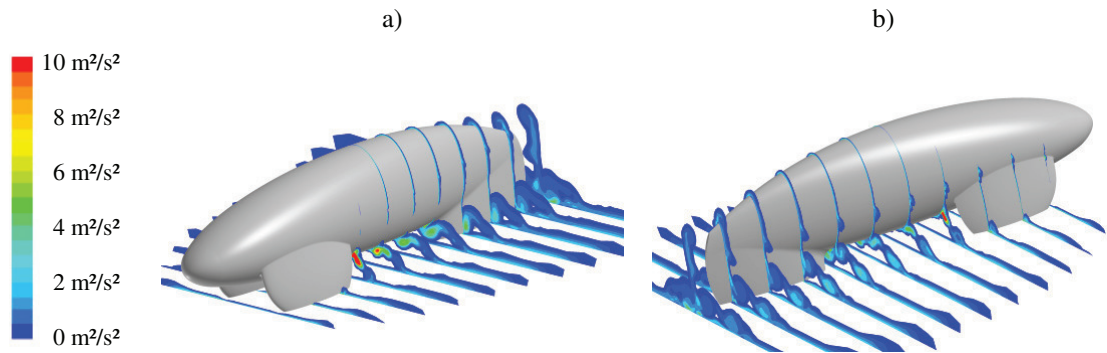
Figure 84: contours of the turbulent kinetic energy in m²/s² for α=5°, a) upwind side, b) downwind side.

Incident flow angle α = 10°:

The pressure coefficients obtained for this case are shown in Figure 85. They agree fairly well with the measurements. The velocity contours shown in Figure 86 surprisingly exhibit smaller disturbances in the surroundings of the rear wheel casing than for α=5°. For α=10° the wake region of the front wheel casing on the upwind side evidently perturbs less the flow field upstream of the rear wheel casing.
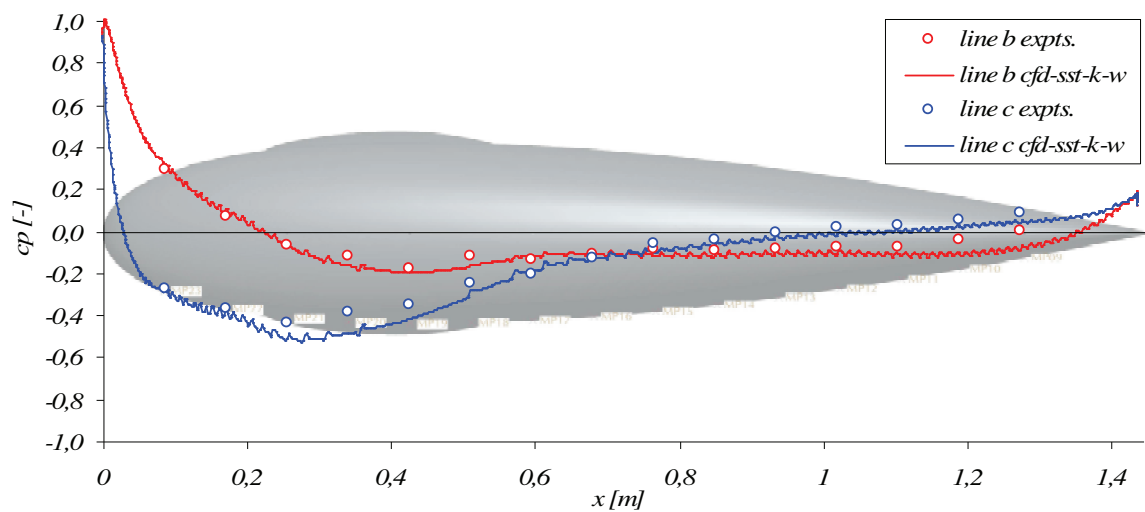
Figure 85: pressure coefficient for α = 10° on upwind (line b) and downwind side (line c).
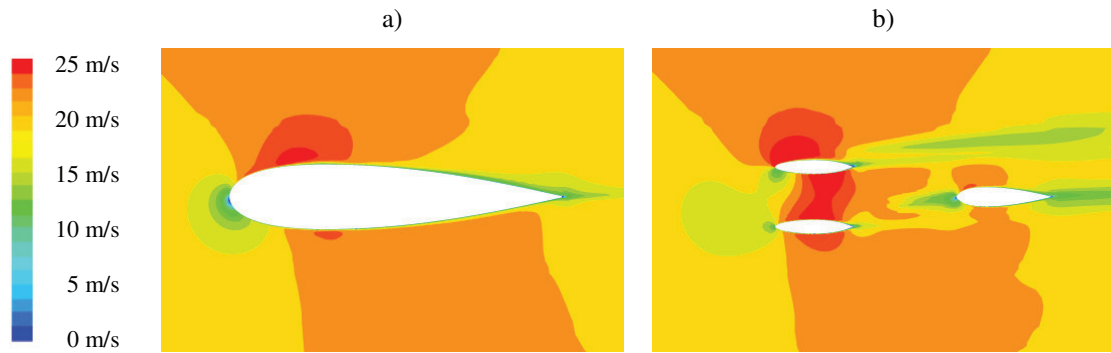
Figure 86: contours of velocity magnitude in m/s for α=10° on horizontal planes, a) at z=0,19m, and b) at z=0,05m.

In accordance with the comparatively small perturbed region around the rear wheel casing observed in Figure 86, the production of the turbulent kinetic energy on the downwind side is also less intense than in the cases with α=0° and α=5° (Figure 80 and Figure 84). On the upwind side the production is similar to that of the case with the two smaller incident flow angles.
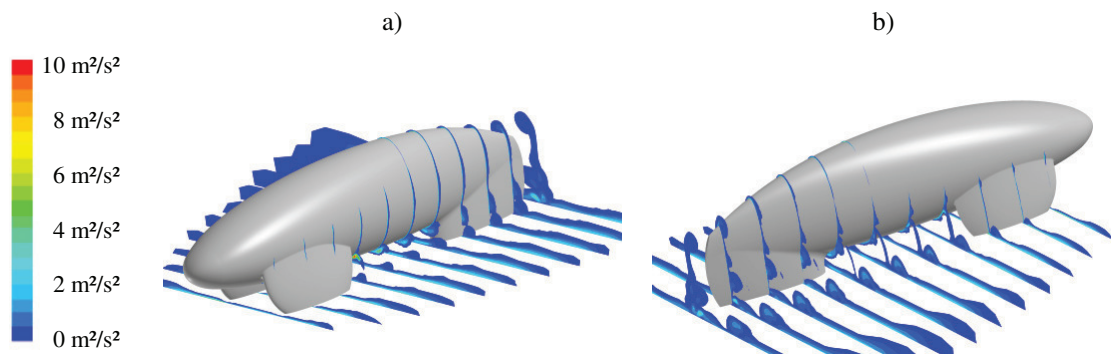
Figure 87: contours of the turbulent kinetic energy in m²/s² for α=10°, a) upwind side, b) downwind side.

Incident flow angle α = 15°:

It was observed in the wind tunnel measurements that the drag coefficient significantly increases for changing the incident flow angle from α=10° to α=15°. This significant increase of the drag coefficient can be mainly attributed to a strongly increased pressure drag due to flow separation in wake of the vehicle. As seen from the velocity contours in Figure 89, flow separation occurs mainly in the wake of the front wheel casing on the downwind side, while on the downwind side of the main body the flow separates only within a very confined region, and it reattaches further downstream. Accordingly, the pressure coefficients on the upwind and downwind side of the main body shown in Figure 88 do not differ markedly from those for α=10°. The simulations agree fairly well with the experiments, except on the downwind side in the region around x=0,6m, where the SST-k-ω produces underpredictions.

From the large wake region observed on the downwind side of the front wheel case in Figure 90 b, it can be concluded that the increased pressure drag, which finally leads to the markedly increased total drag coefficient, is mainly due to the strongly separated flow in this region.
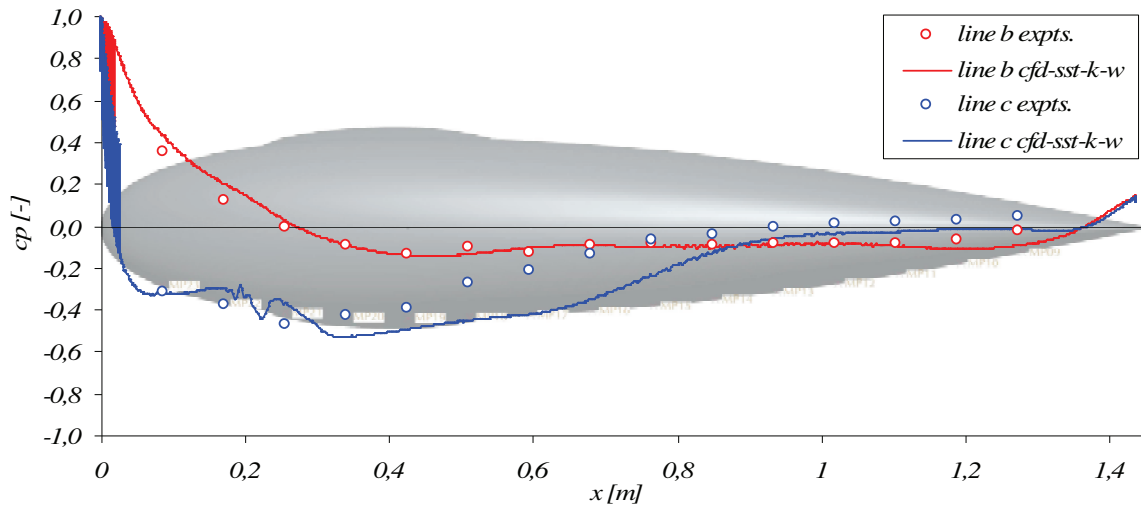
Figure 88: pressure coefficient for $\alpha = 15°$ on upwind (line b) and downwind side (line c).
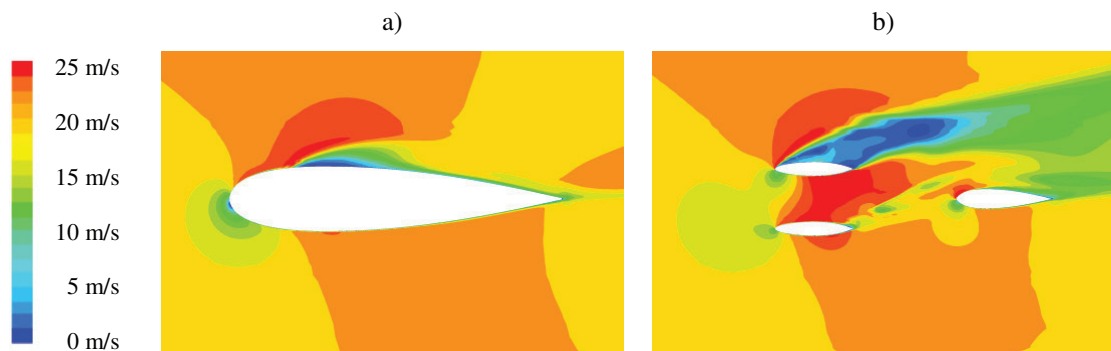
Figure 89: contours of velocity magnitude in m/s for $\alpha=15°$ on horizontal planes, a) at z=0,19m, and b) at z=0,05m.

The vorticity generated and convected further downstream is also well visible in the contours of the turbulent kinetic energy shown in Figure 90. The cross sections downstream of the downwind front wheel exhibit high levels of turbulent kinetic energy.
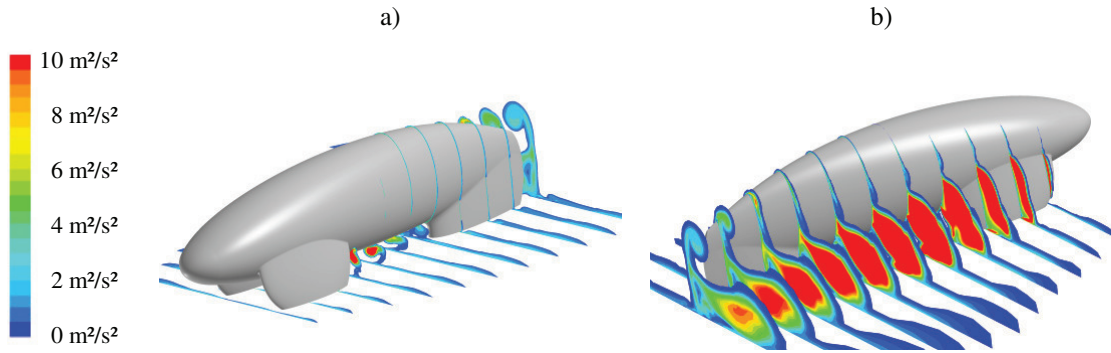
Figure 90: contours of the turbulent kinetic energy in m²/s² for α=15°, a) upwind side, b) downwind side.

Incident flow angle α = 20°:

The incident flow angle of α = 20° marks the maximum of the experimentally measured drag coefficients (see Figure 40). Therefore, the total wake region of this case is expected to be larger than for all other considered incident flow angles. Figure 91 shows the pressure coefficients along both equatorial lines of the test body for this case. On the upwind side the numerical results agree very well with the experiments. Notable deviations occur in the middle of the downwind side, where the SST-k-ω evidently not captures accurately the onset and extent of flow separation as it is indicated by the local minimum in the measured coefficients around x=0,4. Aside from these discrepancies the predictions of the SST-k-ω agree reasonably well with the experiments also on the downwind side.
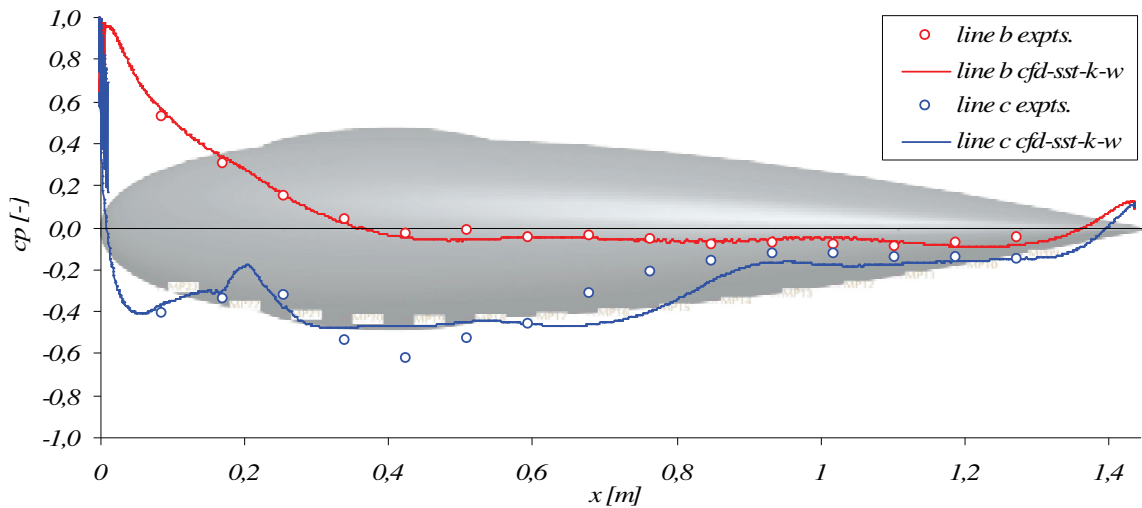
Figure 91: pressure coefficient for α = 20° on upwind (line b) and downwind side (line c).

The velocity contours shown in Figure 92 a exhibit a larger separated flow region on the downwind side of the main body as compared to the case with α=15°. The flow reattaches at the downstream end of the body as well. The wake region on the downwind side of the front wheel casing shown in Figure 92 b extends further downstream than for α=15°, which indicates a comparatively larger region of separated

flow. It is interesting to note that in contrast to the strong separation occurring downstream of the front wheel casing, the flow follows the geometry of the rear wheel casing very well and remains attached.

a)   b)
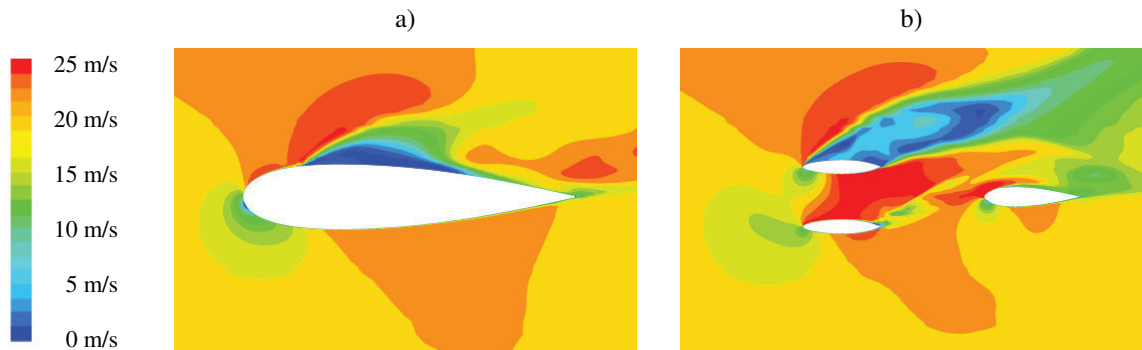
Figure 92: contours of velocity magnitude in m/s for α=20° on horizontal planes, a) at z=0,19m, and b) at z=0,05m.

The wake region associated with separated flow is also seen in Figure 93 displaying cross-sectional contours of the turbulent kinetic energy, which reaches high levels on the downwind side of the vehicle.

a)   b)
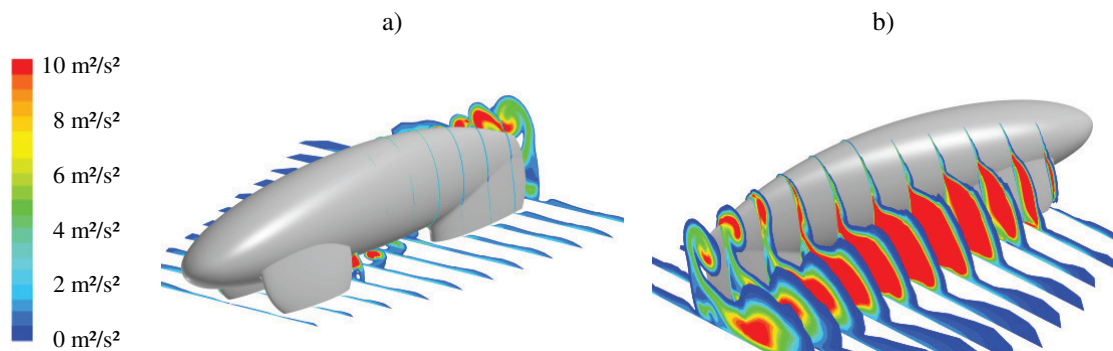
Figure 93: contours of the turbulent kinetic energy in m²/s² for α=20°, a) upwind side, b) downwind side.

Incident flow angle α = 25°:

The case with the maximum considered incident flow angle, α = 25°, was simulated with the SST-k-ω model as well as the DES method. Since the separated flow region in the wake of the test body is expected to be the largest in this case, the concept of DES is supposed to yield more accurate predictions than the steady RANS concept of SST-k-ω. The main focus of the comparison of the results produced by the two model concepts is therefore on the wake area.

Figure 94 shows the pressure coefficients along the upstream equatorial line b compared against the measurements. The open triangles denote the temporal averages obtained with the DES. The error bars representing the standard deviations from the temporal averages are added to show the average range of the instantaneous fluctuations around the mean values. On the upwind side facing the incident flow, no separation occurs, and the results of both models are in good agreement with the experiments.
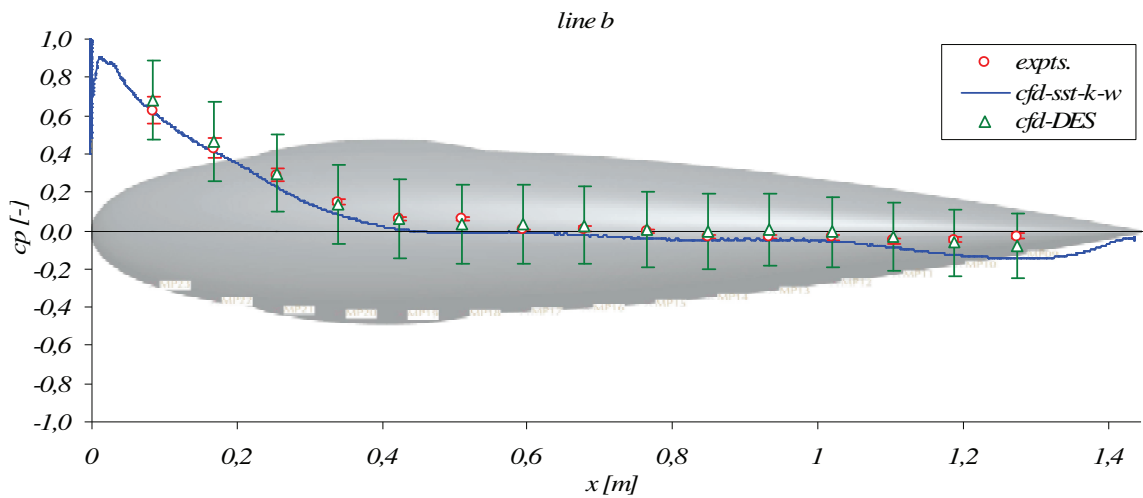
Figure 94: pressure coefficient along line b on the upwind side for α = 25°

In contrast, as indicated by the pressure coefficient along line c in Figure 95, the flow is strongly influenced by separation on the downwind side of the body. The strong oscillations in the predictions of the SST-k-ω model clearly demonstrate the limits of this basically steady RANS approach. As such these steady model approach is conceivably not capable to capture the strongly unstationarily vortical motion in the separated flow region occurring on the downwind side for this high incident flow angle. The DES results show a much better overall agreement with the experiments. The capability of DES to resolve the temporal evolution of the unsteady large vortical structures convected downstream in the wake region leads evidently to better predictions on the downwind side of the body.
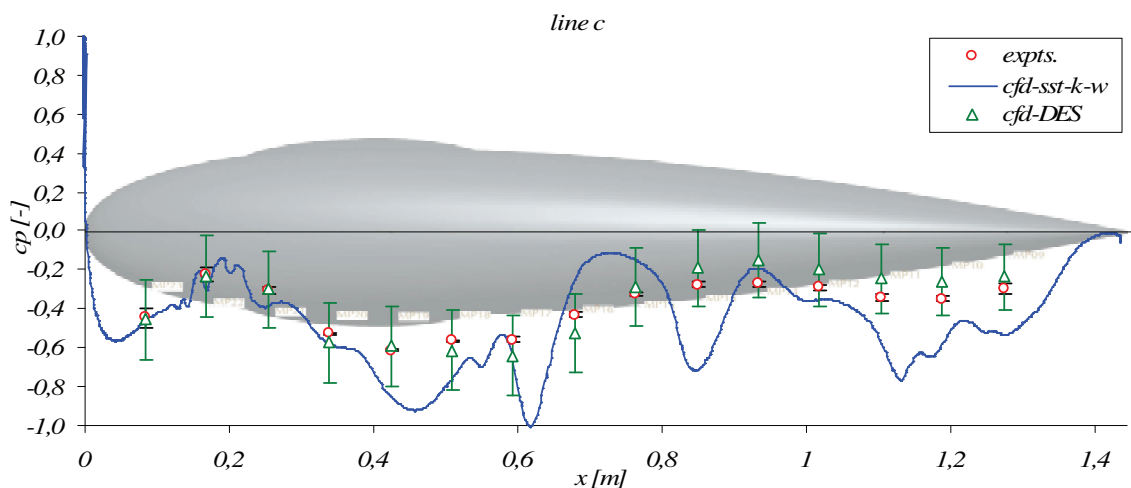
Figure 95: pressure coefficient along line c on the downwind side for α = 25°

The velocity contours shown in Figure 96 can help to further explain the observed differences in the predicted pressure coefficients. As expected the separated flow region downstream of the test body makes the main difference between the predictions of the models. The SST-k-ω turbulence exhibits

comparatively large wake regions especially downstream of the rear wheel casings, while DES predicts a mostly attached flow in this region, as seen from Figure 96 d.
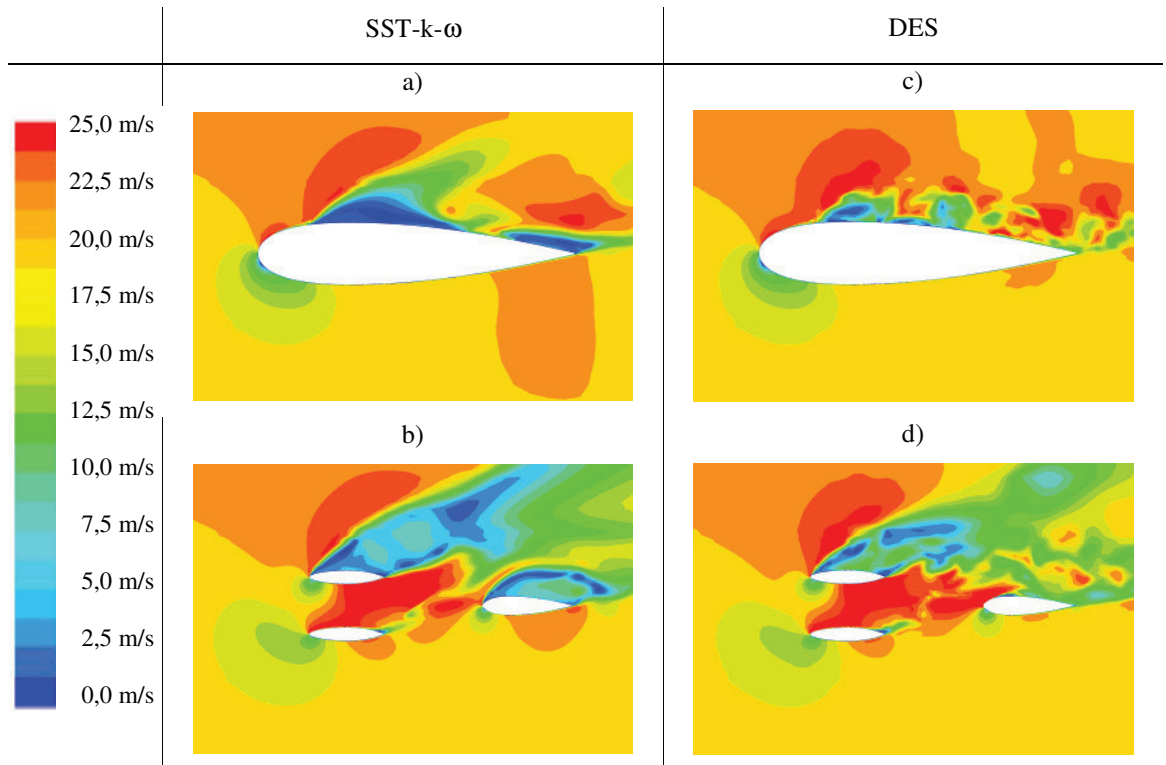
Figure 96: velocity contours in m/s for incident flow angle α=25° on horizontal planes a), c) at z=0,19m, and b), d) at z=0,05m, respectively.

The predicted pressure coefficients near the trailing edge at the body shown in Figure 97 confirm quantitatively the observed differences in the extensions of the wake flow region. DES evidently captures more accurately the increase of the pressure on the downwind side.
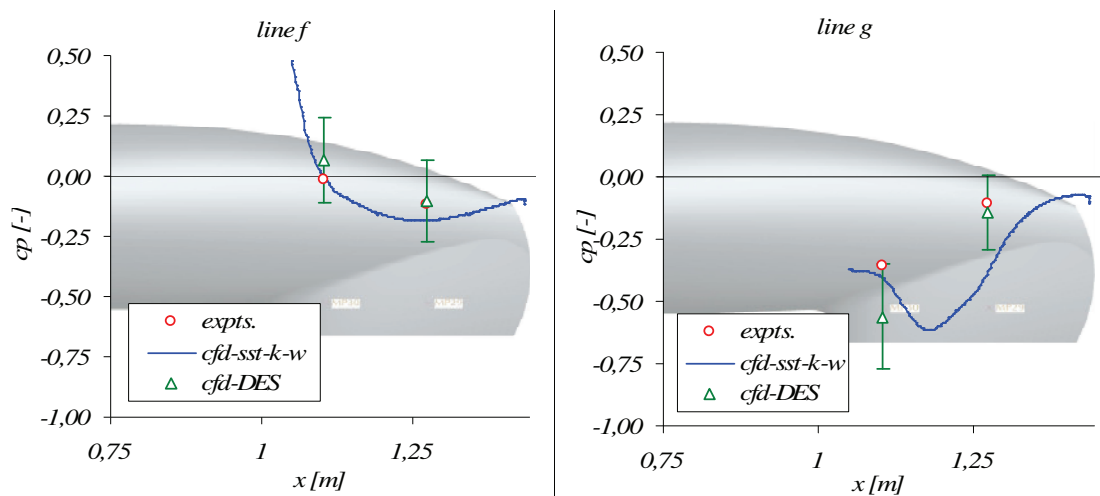
Figure 97: pressure coefficients near the trailing edge of the body for α=25° on the upwind side (line f) and the downwind side (line g).

The cross-sectional contours shown in Figure 98 give a global view on the distribution of the turbulent kinetic energy in the wake region. It becomes evident that the DES predicts more turbulence near the surface on the downwind side, which keeps the flow longer attached than in the SST-k-ω results. In accordance with the smaller wake region DES predicts a less intense turbulent motion, which is convected downstream with the vortices shed from the surface, as it is indicated in Figure 98 d by the comparatively confined spots of high turbulence intensity in the wake region. In contrast, the SST-k-ω model predicts generally much higher levels of turbulence in the separated flow region.
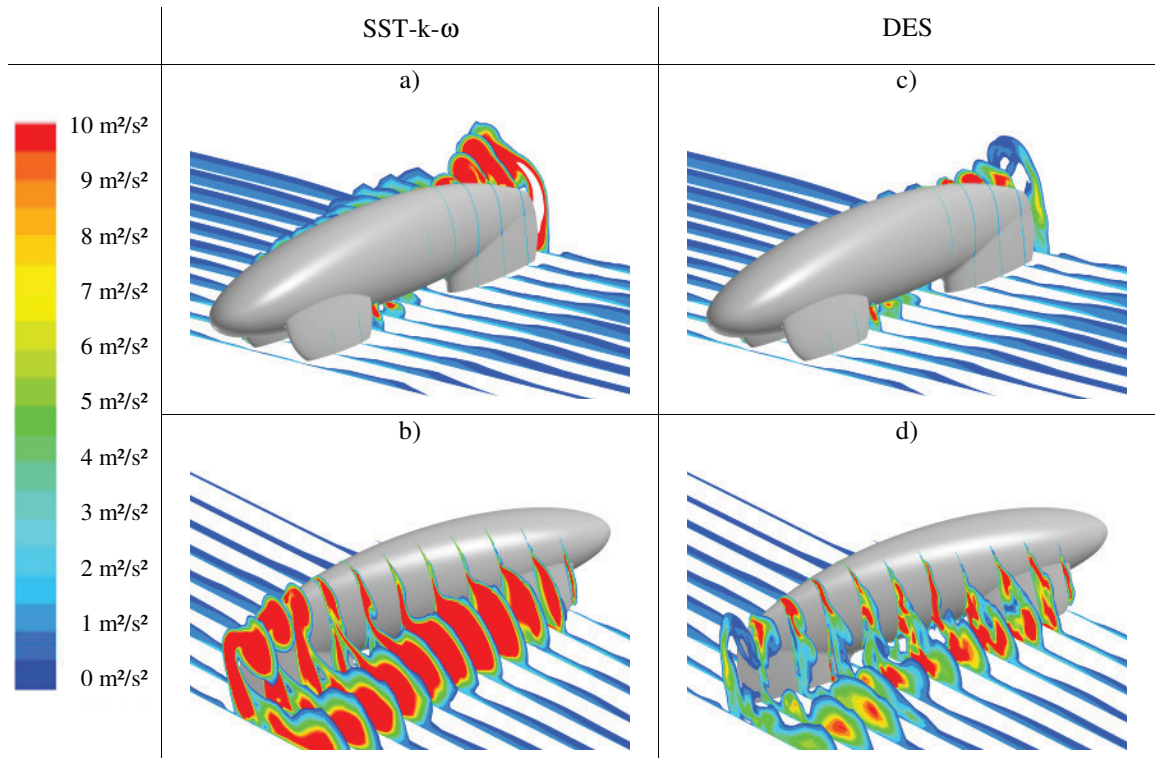
Figure 98: contours of the turbulent kinetic energy in m²/s² for α=25°, a) and c) upwind, b) and d) downwind side.

Predicted force and momentum coefficients

An overview on the predictions for the global coefficients for the aerodynamic forces and moments compared against the experimental values shall be given in the following. Figure 99 shows the drag coefficients obtained for the different angles of incident flow. As already mentioned in the analysis of the measurements, the drag coefficient rises abruptly when incident flow angle exceeds 10°, which can be basically attributed to the increase of the projected surface in this range of α (see Figure 41). The SST-k-ω model could reproduce the increase of the drag coefficient and the peak for α=20° very well. For incident flow angles greater the 20° the separation is evidently overpredicted, and hence, the SST-k-ω yields a too high drag coefficient. As already mentioned above, the DES approach was used only for two incident flow angles, α=0° and α=25°. For the zero incident flow angle, the DES approach shows the

same result as the SST-k-ω model. For α=25°, the DES underpredicts the drag coefficient. This indicated that the capability to resolve the unsteady large vortical structures in time does no straight forwardly lead to most accurate predictions for the total drag. Nontheless, more accurate predictions can be expected for the mainly pressure-induced forces and moments, as it will be shown for the lift and side forces, pitch and yaw moments.
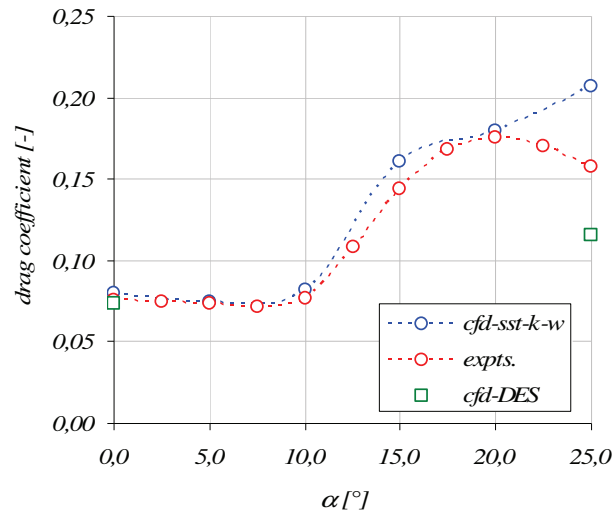
Figure 99: measured and calculated drag coefficient for varying incident flow angles

In Figure 100 the variation of the lift coefficient with the incident flow angle is plotted. The accurate prediction of the lift coefficient is always a very challenging task, as many examples of simulations of the flow around generic automotive test bodies have shown. The predicted lift coefficients of the SST-k-ω model agree fairly well with the experiments as long as separation has a minor effect on the pressure-induced surface forces, i.e. for $0 \leq \alpha \leq 10°$. Beyond this range significant deviations are observed.
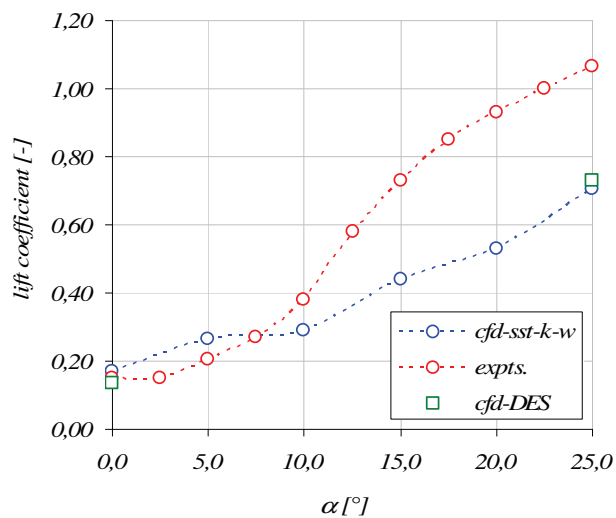
Figure 100: measured and calculated lift coefficient for varying incident flow angles

The best agreement of all measured and simulated forces and moments has the side force. Figure 101 shows the good agreement of the side force coefficient for the experiments and the SST-k-ω model. The DES approach shows a higher side force coefficient, indicating almost attached flow on the downwind side of the rear wheel casing (see Figure 96 d) The attached flow is also visible in Figure 96 from the pressure predictions (line g) where the DES exhibits lower static pressure coefficients than the measurements. As explained for the drag coefficient the wake area could not be resolved sufficiently for the α=25° flow. The more interesting it is that the side force coefficient for this case has a good agreement with the experiments.
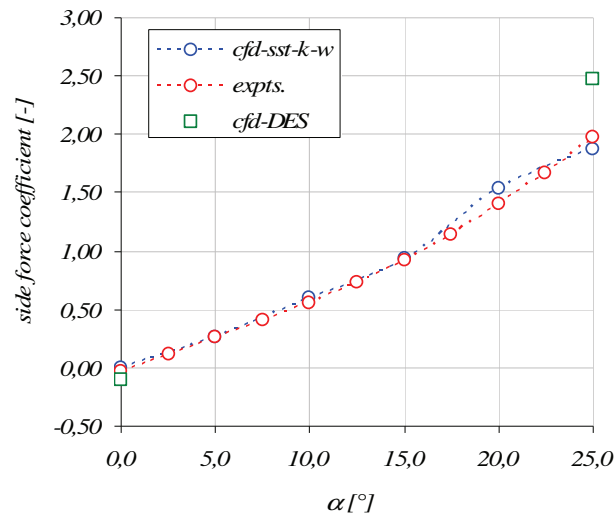
Figure 101: measured and calculated side force coefficient for varying incident flow angles

Figure 102 through Figure 104 show the comparison of the calculated moment coefficients against the measured values. The roll moment which is directly connected to the side force has the best agreement, while the pitching and the yaw moment show only the trend of the measured values.
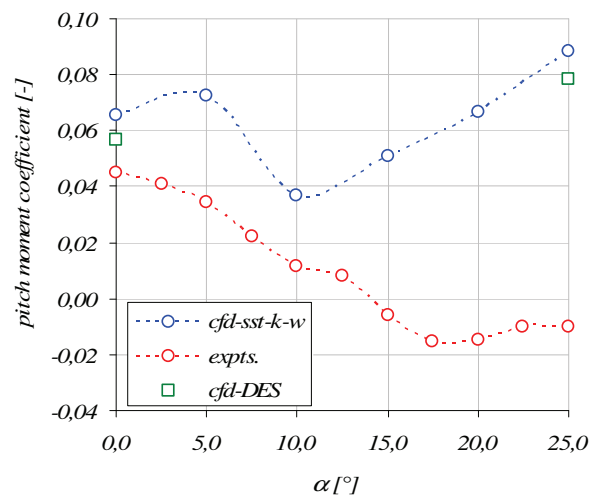
Figure 102: measured and calculated pitching moment coefficient for varying incident flow angles
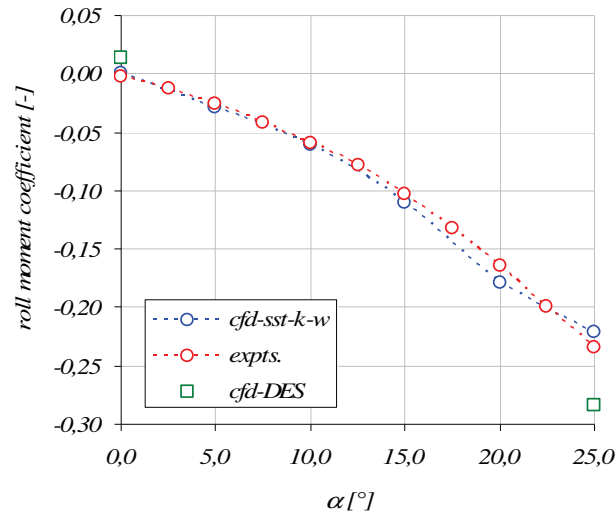
Figure 103: measured and calculated roll moment coefficient for varying incident flow angles
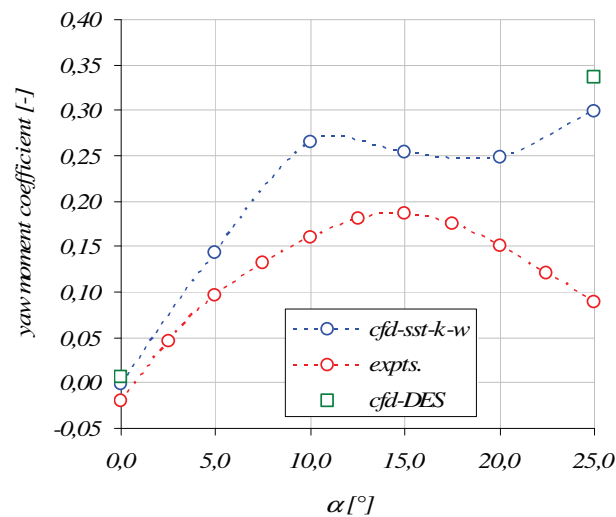
Figure 104: measured and calculated yaw moment coefficient for varying incident flow angles

4.3. CFD as analysis and optimization tool

Computational methods can greatly help to improve the shape of a body to minimize the aerodynamical losses. This often requires to identify those areas, where aerodynamical losses are generated. The wind tunnel experiment deliver in general forces and moments, but without any distinction between viscous and pressure forces. Even though the visualization of the wake is not very difficult to realize, and the measurement of the pressure at selected points on the surface has become a standard technique in wind tunnel experiments, the big advantage of computational fluid dynamics is the comprehensive and detailed description of the actual flow conditions. All kinds of flow quantities can be analyzed at any location in the fluid domain, global forces and moments can be easily derived. As such CFD represents a powerful analysis tool. In the present work the post processing software of ANSYS FLUENT as well as the flow field analysis software Fieldview (Fieldview 2010) were used. The usefulness of CFD for gaining a

deeper insight into the aerodynamic performance of a considered geometry shall be exemplarily shown in the following analysis of the drag and side forces.
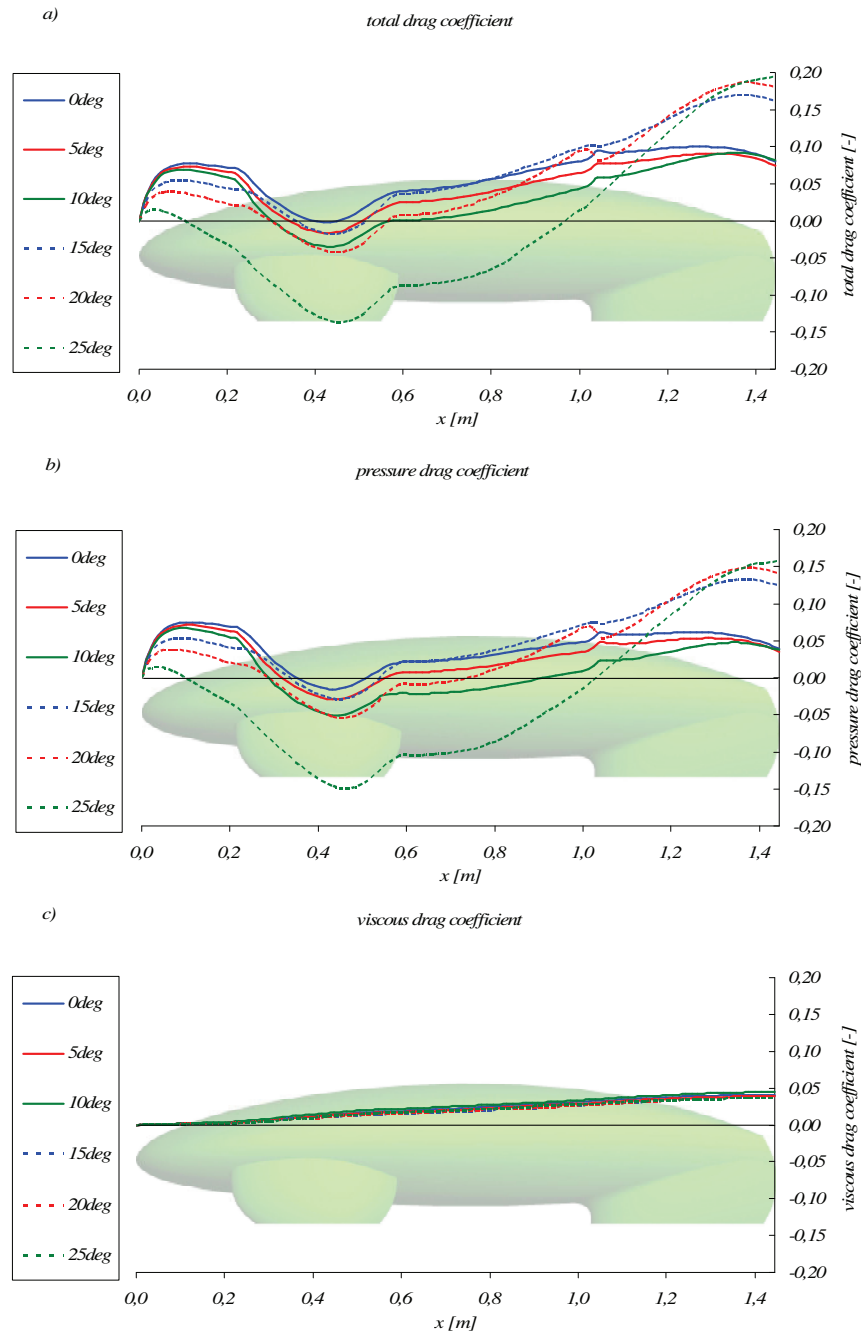
Figure 105: pressure drag coefficient and viscous drag coefficient accumulated along the test body for varying incident flow angle α.

Figure 105 shows the variations of the drag coefficient accumulated over the axial length starting from the upstream end of the vehicle. The total accumulated drag is shown in Figure 105 a, the pressure and the viscous components are shown in Figure 105 b and c, respectively. The depicted curves are obtained from the simulations for all considered incident flow angles using the SST-k-ω turbulence model. It becomes evident that the increase of the drag coefficient for higher incident flow angles α=15/20/25°, (see also

Figure 99) is mainly caused by the pressure losses at the downstream end of the body, while the viscous drag is nearly the same for all incident flow angles. The viscous drag is even somewhat higher for zero and small incident flow angles, which is not surprising, as the flow remains mostly attached to the surface in these cases.

The variations of the side force coefficient accumulated from the front end of the body are shown in Figure 106. The total side force coefficient almost monotonously increases for the higher flow angles, becoming largest for α=25°. The viscous contribution to the side force is almost negligible as seen from Figure 106 c.
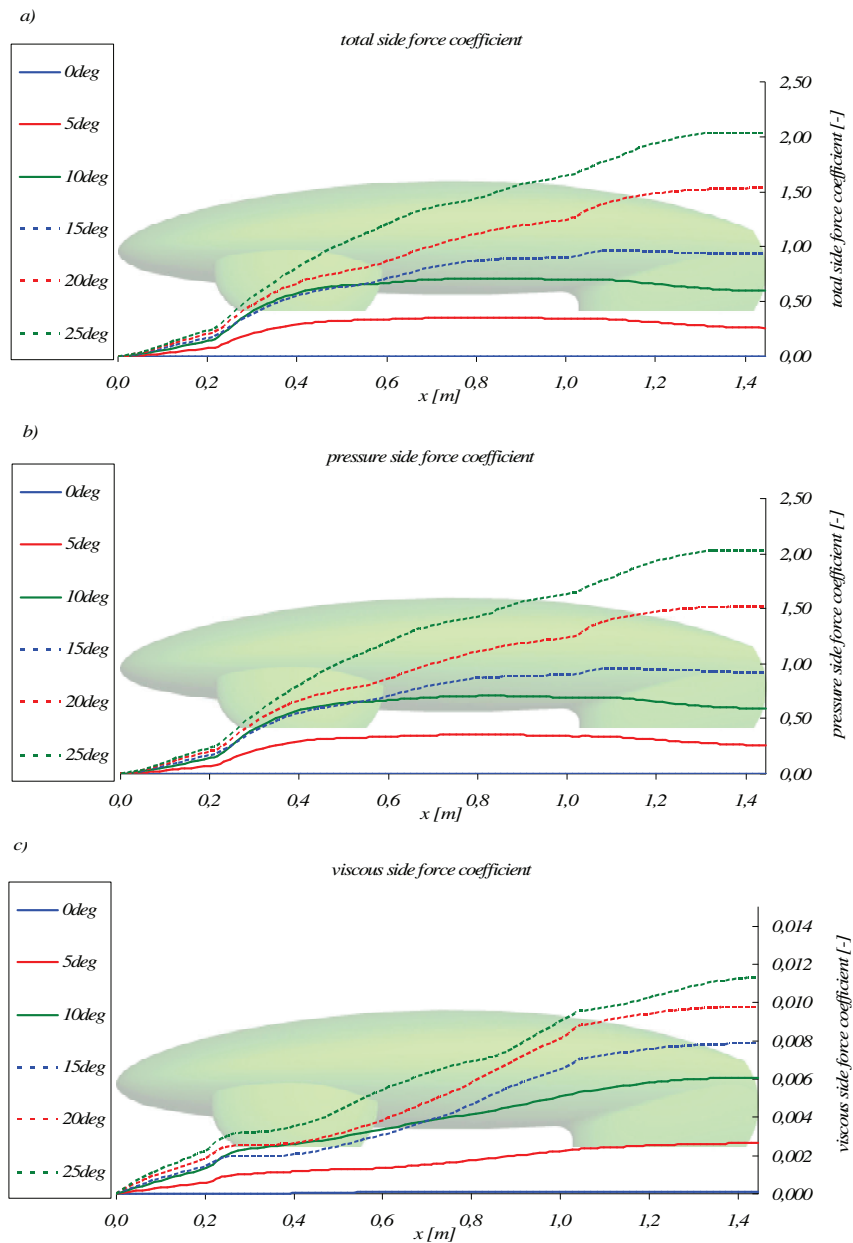
Figure 106: pressure side force coefficient and viscous side force coefficient accumulated along the test body for varying incident flow angle α.

In order to gain more insight into the effect of the wheel casings on the aerodynamics of the test body, a simulation with only the main body was carried out for zero incident flow angle. The motivation to this additional simulation was to highlight the potential for a reduction of the drag achievable with a further optimization of the wheel casings. The accumulated drag coefficients obtained from the simulation with only the main body are shown in Figure 107. The total drag coefficient of the main body without wheel casings (indicated by the end value of the red line) is evidently about 0,035, which is less than half the value of the test body with wheel casings. This means that the wheel casings generate more than the half of the total drag, even though they are very small in comparison to the main body. The main body basically behaves like a slender airfoil causing almost no separation. This is very conceivable, because the main body is essentially composed of NACA airfoil geometries. In Table 13 the decompositions of the total drag into the pressure and the viscous contributions are compared for the two geometries. Most part of the total drag on the main body without wheel casings is evidently due to viscous forces. It is also obvious that the strong increase of the total drag coefficient for the whole test body can be mainly attributed to the increased pressure losses due to the presence of the wheel casings.
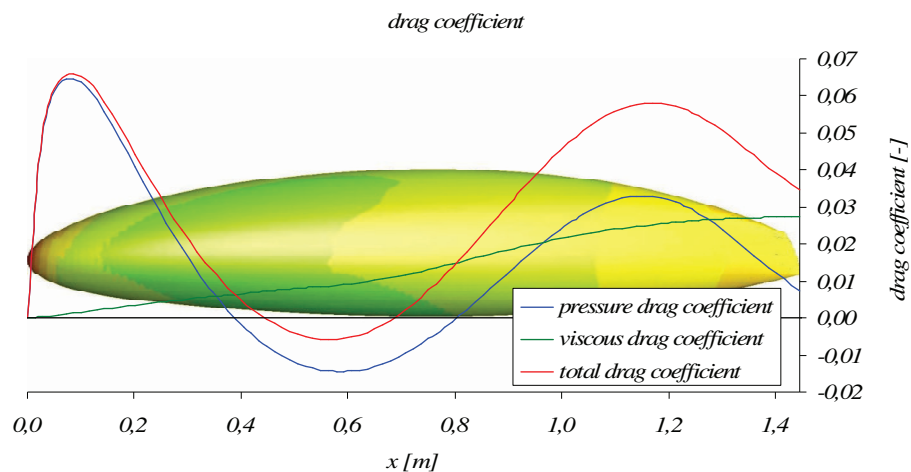
Figure 107: pressure, viscous and total drag coefficients accumulated along the main body without wheel casings

Table 13: decomposition of drag on the main body without wheel casings and the whole test body including wheel cases; SST-k-ω results for zero incident flow angle.

	total drag coefficient	pressure contribution		viscous contribution
main body without wheel casings	0,035	21%		79%
test body (with wheel casings)	0,080	49%		51%

The possibility to separate the total force into a viscous and pressure contribution, provides evidently valuable information, where areas of greatest loss are located and improvements could be made.

A qualitative insight into the vortical structures evolving in the wake region is given by the iso-surfaces of the second invariant of the velocity gradient. This invariant, which is defined as

$$Q = -\frac{1}{2}\frac{\partial \overline{u_i}}{\partial x_j}\frac{\partial \overline{u_j}}{\partial x_i}, \tag{4.6}$$

visualizes nicely the size and the distribution of the large coherent vortices emerging in the separated flow region. Figure 108 shows iso-surfaces for Q=5 coloured with the velocity magnitude for six different incident flow angles. For the smallest angles, narrow vortex tubes emerge from the trailing end of the body evolving further downstream aligned with the direction of the free stream velocity, as it is typically featured by attached flow past slender bodies.
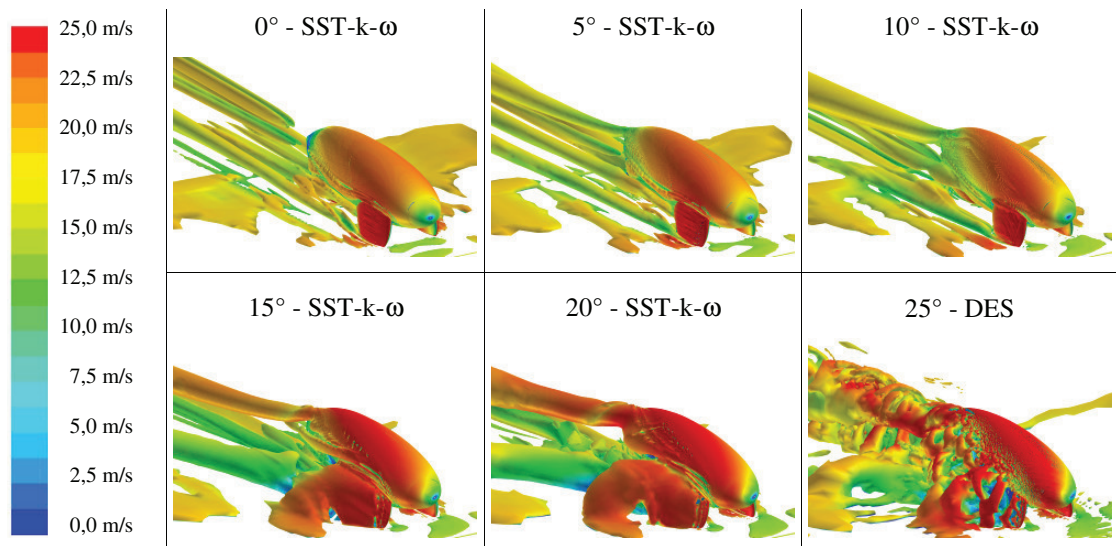
Figure 108: iso-surface of second velocity invariant Q=5 coloured with velocity magnitude in m/s.

In contrast, for the higher flow angles, additional vortical structures appear particularly in the wake of the wheel casings. They are larger in size than those observed for small flow angles, and they show no distinct orientation. The formation of these vortices also explains the strong increase of the pressure drag observed for these higher incident flow angles.

A further useful method to analyse the flow structure near the wall is displaying the streamlines obtained in the first near-wall computational cells. These lines are shown in Figure 109, where they are coloured by the magnitude of the local wall shear stress, in order to show the exact position of separation and reattachement. Accordingly, the onset of flow separation is visualized at those points, where the colour of the streamlines turns into blue indicating zero local wall shear stress, which is associated with separation and reattachement. The latter phenomenon is well visible in Figure 109 for α=0° and α=5°, where the change of the wall shear stress to positive values is indicated by an abrupt change of the line colour from blue to green occurring on the upper surface of the body. Furthermore, the transition from laminar to

turbulent flow becomes visible as well. The marked increase of the wall shear stress associated with this transition can be seen in Figure 109 from a fast change in the line colour from green to red.
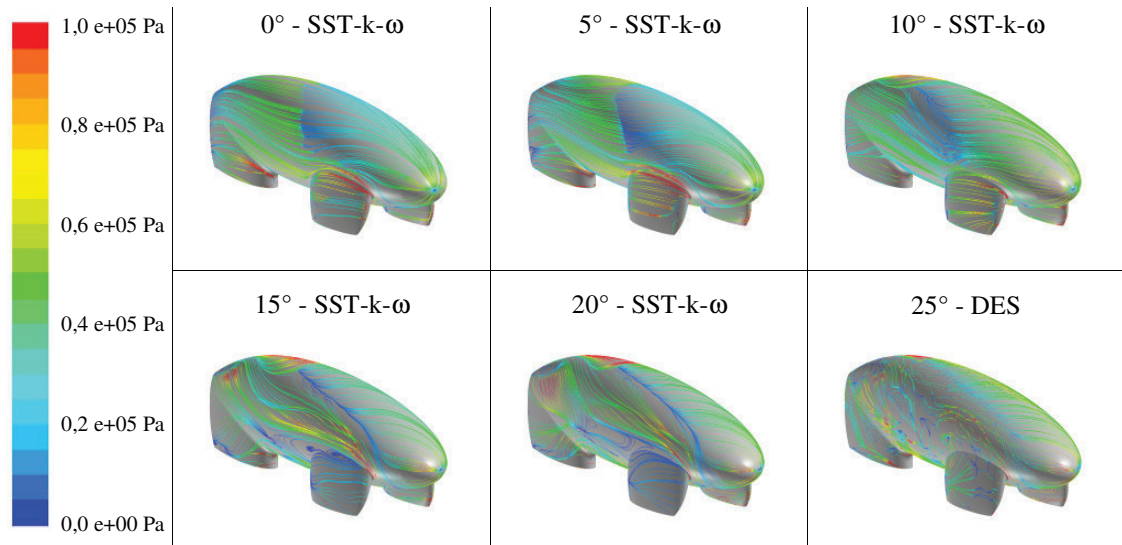
Figure 109: surface restricted flow: separation and reattachment lines coloured with wall shear magnitude

In summary, it can be said, that the combination of the presented analysis tools provide highly valuable information for the development and aerodynamical optimization of low drag bodies in the future.

5.   Conclusions

The aerodynamic performance of the low-fuel-consumption vehicle TERA Fennek was investigated experimentally as well as numerically. The wind tunnel measurements, which were carried out with a model on a scale 1:2 for varying incident flow angles, provided a comprehensive data base for a validation of the computational results. The experiments turned out a relatively sharp increase of the drag and lift forces as the incident flow angle exceeds $\alpha \approx 10°$. It was found that the here observed sharp increase follows essentially the marked increase of the body's projected area facing the oncoming flow, which occurs in this range of angles of incidence. While the measured lift and side force coefficients monotonically increase with the incident flow angle, the drag coefficient first increases to a maximum around $\alpha = 20°$, decreases further beyond, e.g. for $\alpha = 25°$, it to a somewhat lower level. The influence of the Reynolds number, which was varied in the measurements by imposing three different inflow velocity magnitudes, turned out to be very small.

The numerical simulation used the SST-k-ω turbulence model for all considered incident flow angles α. For zero and the maximum considered flow angle, $\alpha = 0°$ and $\alpha = 25°$, respectively, a Detached Eddy Simulation was carried out as well in order to assess the predictive capabilities of this unsteady hybrid, computationally much more expensive, approach as compared to the steady RANS concept of SST-k-ω. The computationally cheaper SST-k-ω model was proven to predict fairly accurately the pressure distributions on the body surface and the drag coefficients. The strong increase of the drag force around $\alpha = 10°$ is reflected by the simulations as well. For the highest considered incident flow angle $\alpha = 25°$, the limits of this steady RANS concept becomes evident. The solution for the local pressure distributions on the downwind side of the body exhibit strong oscillations pointing at the significant unstationary large-scale motion occurring in the real wake of the body, which is not resolved by the steady SST-k-ω concept. In consequence, the SST-k-ω overpredicts markedly the drag coefficient at $\alpha = 25°$, and hence, the numerical results do not reflect the experimentally observed decrease of the drag coefficient as α increases from 20 to 25°. The tested alternative concept of DES gave somewhat improved predictions for the pressure distribution on the downwind side for $\alpha = 25°$, as it was expected from this unsteady hybrid approach. The better description of the separated wake flow region does however not automatically translate into highly accurate predictions for the global force and moment coefficients. The predictions of DES still exhibit notable deviations from the experiments, thus questioning the justification of the high computational costs associated with this method.

Despite the inaccuracies of the numerical predictions particularly observed for high incident flow angles, the numerical flow simulations were proven to serve as a powerful tool to analyze the aerodynamical performance of a tested geometry in more detail than experiments can do. As such the CFD-based analysis provides insight into the individual contributions of the pressure and viscous forces to the total drag. The CFD results also helps to identify those critical parts of the test body, where a great portion of the aerodynamic drag is generated. Thus, the CFD results provide useful information for a further optimization of the aerodynamics of the considered geometry.

6. List of Figures

7. List of Tables

8.   List of Literature

Literature sources

[Ahmed 1984]   Ahmed S.R., Ramm G., Some Salient Features of the Time-Averaged Ground Vehicle Wake, SAE-Paper 840300, 1984

[Ashley 1965]:   Ashley H., Landahl M.: Aerodynamics of Wings and Bodies, first Edition, 1965, Dover Publications, Mineola, ISBN 0-486-64899-0, pp. 71-73

[Bair 1989]:   Bair E.: Experimentelle Ermittlung von Geschwindigkeitsprofilen in Windkanalmessstrecken, Diplomarbeit, Institut für Strömungslehre und Wärmeübertragung, TU Graz, 1989, page 94

[Batchelor and Townsend 1948]:   Batchelor G.K., Townsend A.A.: Decay of Isotropic Turbulence in the Initial Period in Proceedings of the Royal Society of Lonodn. Series A, Mathematical and Physical Science, Vol. 193, No. 1035, The Royal Society, London, pp. 539-558

[Courand 1928]:   Courant R., Friedrichs K., Lewy H.: Über die partiellen Differenzengleichungen der mathematischen Physik, 1928, Mathematische Annalen 100, 32-74

[Drage 2008]:   Drage, P., Gabriel, A., Lindbichler, G., Hörmann, T., Brenn, G., Meile, W.: Efficient Use of Computational Fluid Dynamics for the Aerodynamic Development Process in the Automotive Industry, AIAA paper no. 2008-6735

[Ferziger 2002]:   Ferziger J. H., Peri´c M.: Numerische Strömungsmechanik, 3rd Edition, 2002, Springer Verlag, Berlin Heidelberg New York, ISBN 978-3-540-67586-0, p. 330

[Herwig 2008]:   Herwig H.: Strömungsmechanik – Einführung in die Physik von technischen Strömungen, 1. Auflage, 2008, Vieweg+Teubner Verlag, Wiesbaden, ISBN 978-3-8348-0334-4, page 17

[Hucho 2002]:   Hucho W.H., Aerodynamik der stumpfen Körper, 1. Auflage, 2002, Vieweg&Sohn Verlagsgesellschaft, Braunschweig Wiesbaden, ISBN 3-528-06870-1

[Hucho 2005]:   Hucho W.H., Aerodynamik des Automobils, 5. Auflage, 2005, Springer Verlag, Berlin Heidelberg New York, ISBN 978-3-528-03959-2

[Lücke 1997]:   Lücke, J.R., Turbulenzmodellierung zur Berechnung abgelöster Strömungen in Turbomaschinen, Dissertation, Institut für Strahlantriebe und Turboarbeitsmaschinen, RWTH Aachen, 1997

[Menter 1993]:   Menter F.R., Zonal two-equation k-ω turbulence model for aerodynamic flows. AIAA, Paper 1993-2906, 1993.

[Menter 1994]:   Menter F.R., Two-Equation Eddy-Viscosity Turbulence Models for Engineering Applications, AIAA-Journal, 32(8), pp. 269-289, 1994.

[Menter 2003]   Menter F. R., Kuntz M., and Langtry R.: Ten Years of Experience with the SST Turbulence Model. In Hanjalic K., Nagano Y., and Tummers M., editors, Turbulence, Heat and Mass Transfer 4, pages 625–632. Begell House Inc., 2003

[Nitsche 2006]:   Nitsche W., Brunn A.: Strömungsmesstechnik, 2. Auflage, 2006, Springer Verlag, Berlin Heidelberg New York, ISBN-10 3-540-20990-5

[Schlichtling 2001]:   Schlichtling H., Truckenbrodt E.: Aerodynamik des Flugzeuges – erster Band, 3. Auflage, 2001, Springer Verlag, Berlin Göttingen Heidelberg, page 119

[Spalding 1972]   Spalding D B, Launder B E: Lectures in Mathematical Models of Turbulence, Academic Press, London, England, 1972

[Strouhal 1878]:   Strouhal V.: Ueber eine besondere Art der Tonerregung, Annalen der Physik und Chemie, Neue Folge. Band V, 1878, Verlag von Johann Ambrosius Barth, Leipzig, pages 216-251

[Versteeg 2007]:   Versteeg H K, Malalasekera W: An Introduction to Computational Fluid Dynamics - The Finite Volume Method, second Edition, 2007, Pearson Education Limited, Edinburgh, ISBN 978-0-13-127498-3, page 280

[Wilcox 1998]   Wilcox D C: Turbulence Modeling for CFD, DCW Industries, Inc., La Canada, California, 1998.

Internet sources

[CFD-Wiki 2010, SST-k-omega]:   http://www.cfd-online.com/Wiki/SST_k-omega_model, 26.07.2010

[DEWESoft 2010]:   http://www.dewesoft.com/, 26.07.2010

[FLUENT Theory Guide 2009]:   https://secure.fluent.com/sso2/login.htm, 2009, ANSYS Inc

[Natec 2010]:   http://www.allsensors.com/datasheets/J2/AmpLow/amp_low_mil.pdf, 27.07.2010

[Sensortechnics 2010]:   http://www.sensortechnics.com/download/DS_Standard-HCLA_E_11629.pdf, 27.07.2010

[Spiderview 2010]:   http://www.meshing.at/Spiderhome/Home.html, 27.07.2010

9. Appendix

A   Wind tunnel model

B   Wind tunnel mounting

C   Work Flow

D   Analysis

   α=0° SST-k-ω

   α=5° SST-k-ω

   α=10° SST-k-ω

   α=15° SST-k-ω

   α=20° SST-k-ω

   α=25° SST-k-ω

   α=0° DES

   α=25° DES

   α=0° SST-k-ω / main body

A Wind tunnel model
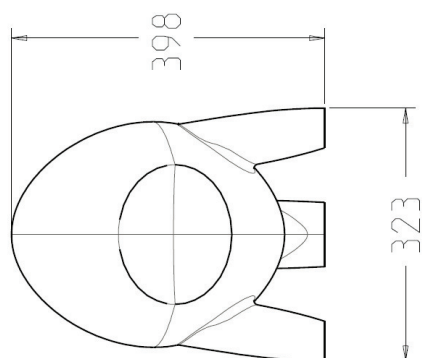
Aproj = 0.09746 m^2
surface area = 1.34712 m^2
volume = 0.07291 m^3

398

323

800

375

1445

399

1444

Y

Y

Z

Z

200

300

Z-Z

270

Y-Y

270
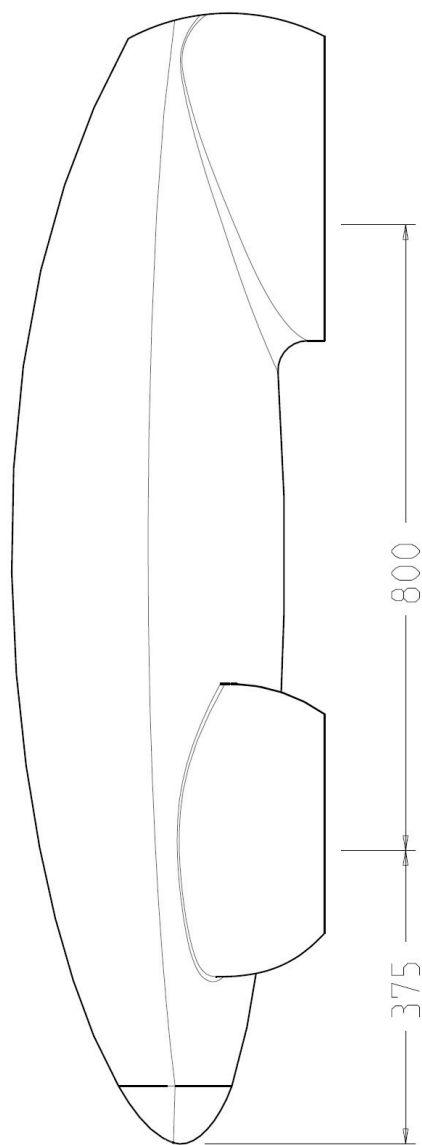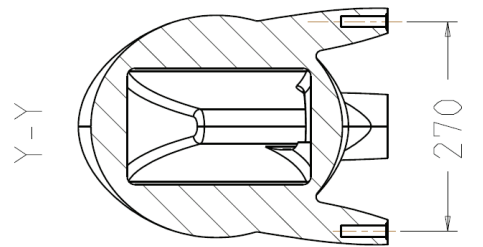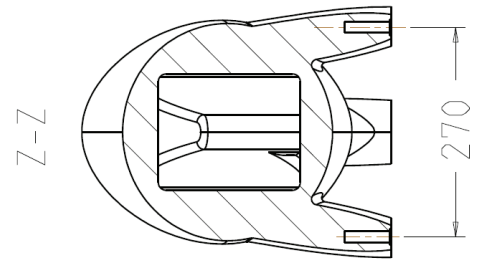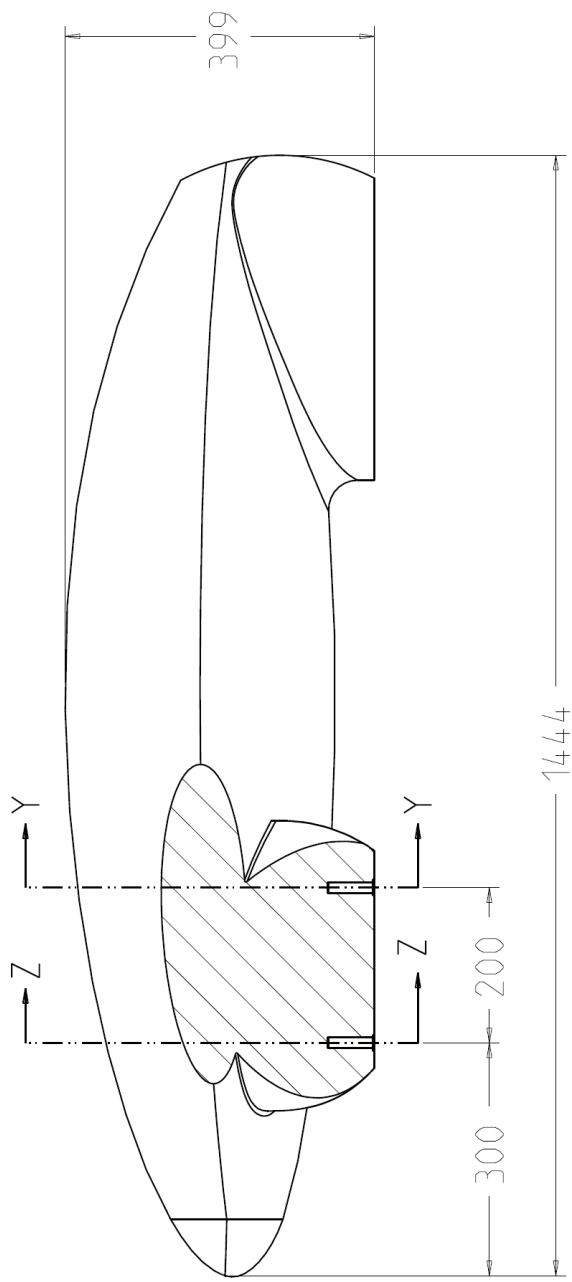
B Wind tunnel mounting
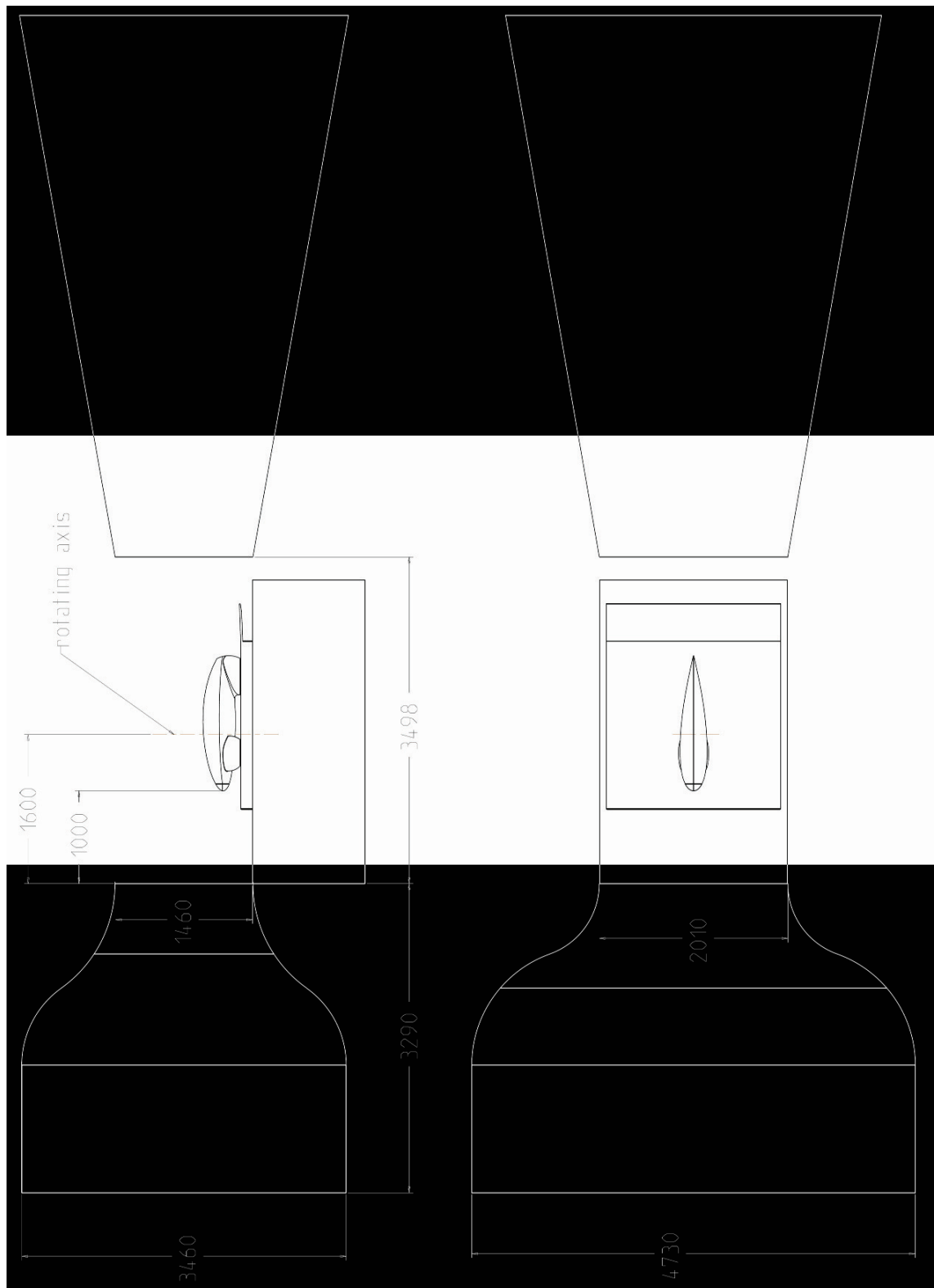
C   Work Flow

Due to consideration of all made experiences during the work on the diploma thesis the following working process is a recommendation for the simulation of low drag bodies. The notices A-3 to A-6 are in the appendix and contain detailed information about the single settings.
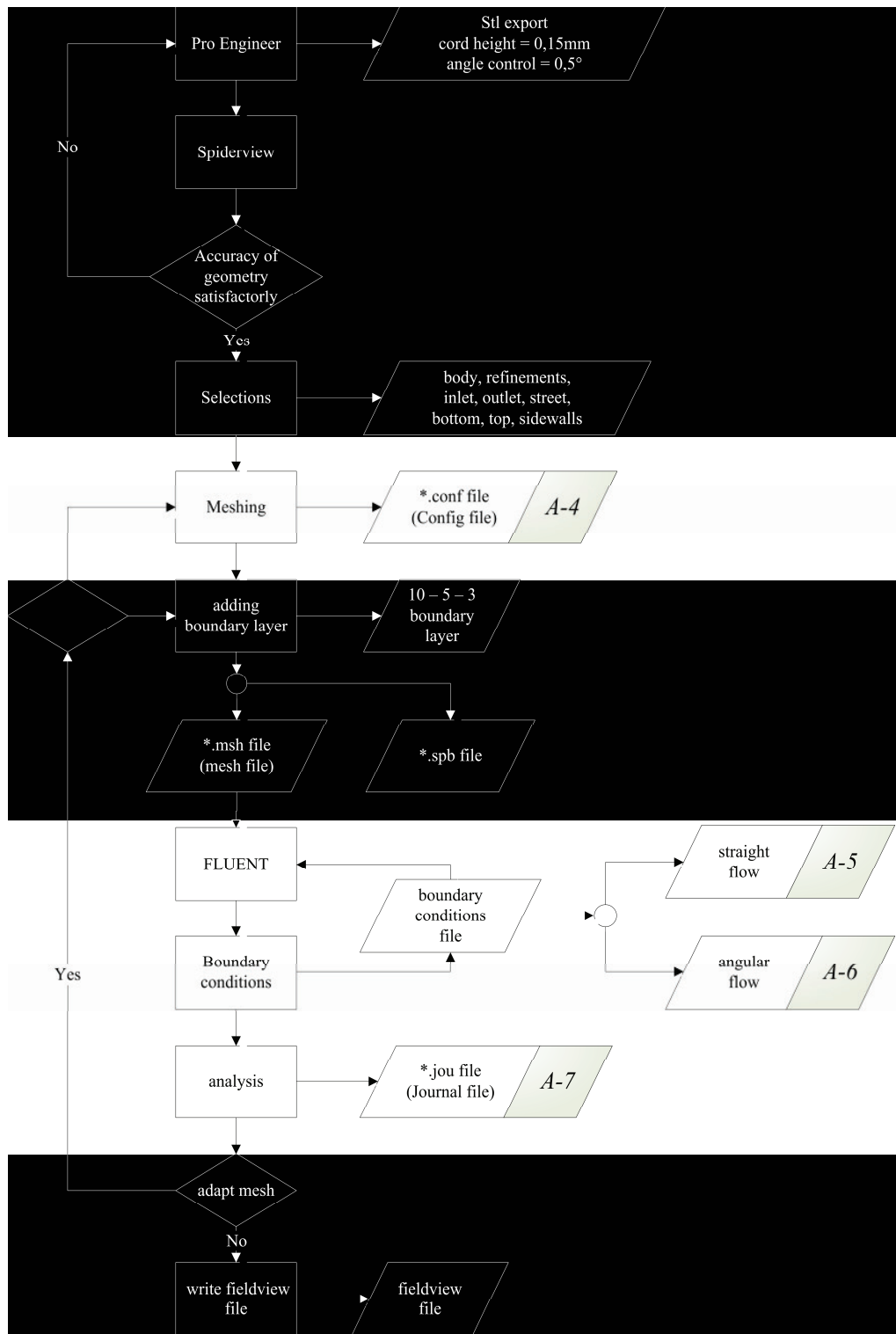
D   Analysis

The following table gives an overview of all made simulations with the incident flow angle, the used turbulence models and the calculated forces. Detailed information on the single simulations are on the following pages. The identification of the single simulations was made via the date (Year Month Day).

case name	incident flow angle [°]	turbulence model
100707	0,0	SST-k-ω
100714	5,0	SST-k-ω
100622	10,0	SST-k-ω
100712	15,0	SST-k-ω
100729	20,0	SST-k-ω
100702	25,0	SST-k-ω
100805	0,0	DES
100812	25,0	DES
100709 (main body)	0,0	SST-k-ω

$\alpha = 0° / SST\text{-}k\text{-}\omega$

force and moment coefficients

|	windtunnel	cfd	tolerance	press. ratio	visc. ratio
c_w	0,075830	0,079919	5,12%	49%	51%
c_a	0,147892	0,169350	12,67%	99%	1%
c_s	-0,034309	-0,001044	-3185,58%	91%	9%
c_r	-0,003191	-0,000191	-1570,68%	100%	0%
c_n	0,045107	0,065338	30,96%	92%	8%
c_g	-0,019617	-0,000322	-5992,24%	100%	0%

pressure coefficients

line a and h

line d and e
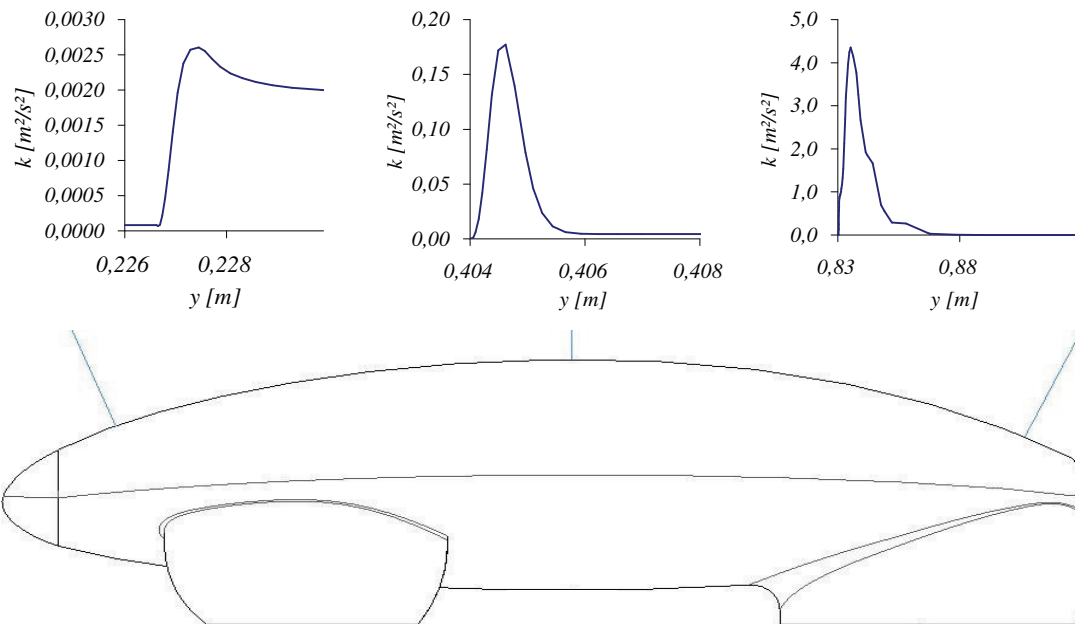
line b and c

line f and g

turbulent kinetic energy [m²/s²] in boundary layer on three positions in the symmetry plane

$\alpha = 5° / SST\text{-}k\text{-}\omega$

force and moment coefficients
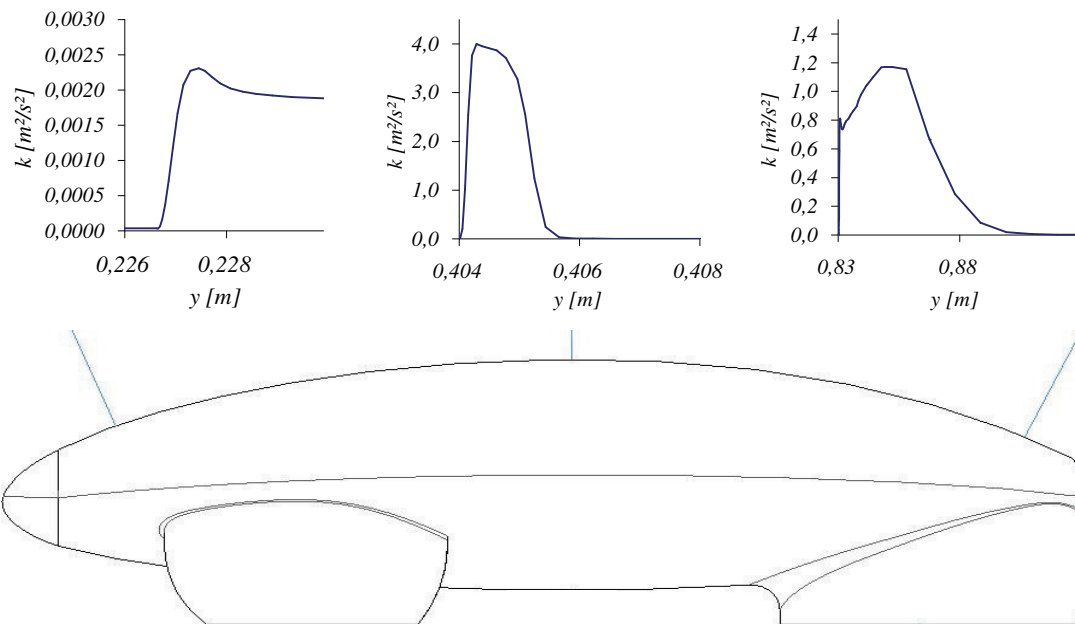
	windtunnel	cfd	tolerance	press. ratio	visc. ratio
c_w	0,073302	0,074510	1,62%	48%	52%
c_a	0,203178	0,266344	23,72%	99%	1%
c_s	0,258389	0,260725	0,90%	99%	1%
c_r	-0,025725	-0,028564	9,94%	98%	2%
c_n	0,034304	0,072510	52,69%	93%	7%
c_g	0,096599	0,143806	32,83%	100%	0%

pressure coefficients

line a and h

line d and e

line b and c

cp [-]

x [m]

- ○ line b expts.
- — line b cfd-sst-k-w
- ○ line c expts.
- — line c cfd-sst-k-w

line f and g

cp [-]

x [m]

- ○ line f expts.
- — line f cfd-sst-k-w
- ○ line g expts.
- — line g cfd-sst-k-w

turbulent kinetic energy [m²/s²] in boundary layer on three positions in the symmetry plane

k [m²/s²]   y [m]

k [m²/s²]   y [m]

k [m²/s²]   y [m]

$\alpha = 10° / SST\text{-}k\text{-}\omega$

force and moment coefficients
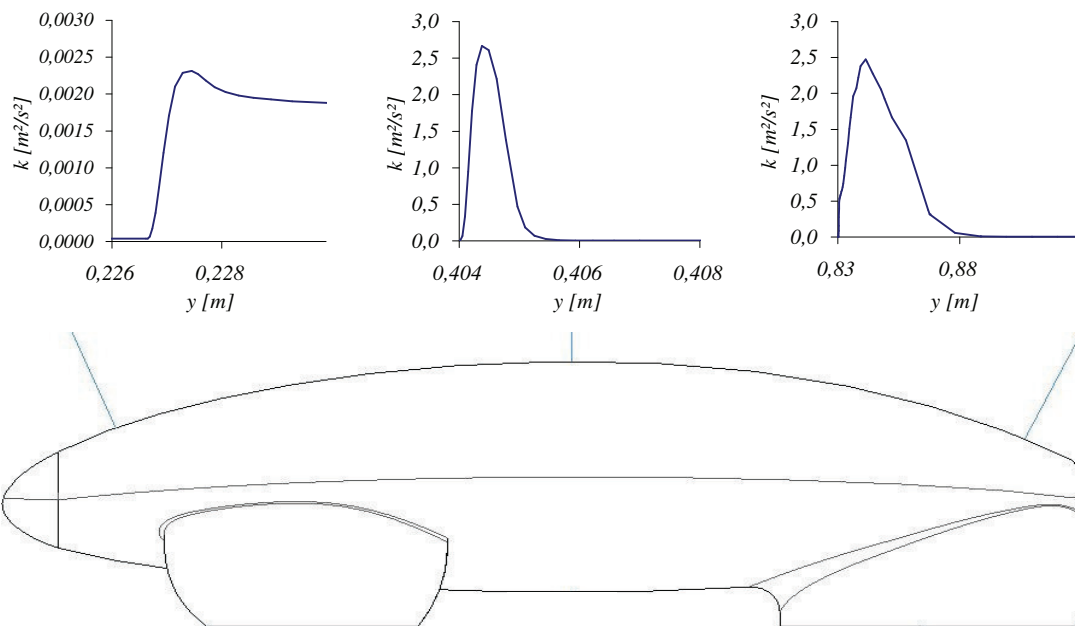
	windtunnel	cfd	tolerance	press. ratio	visc. ratio
c_w	0,076350	0,082295	7,22%	45%	55%
c_a	0,382348	0,291286	-31,26%	100%	0%
c_s	0,557324	0,601601	7,36%	99%	1%
c_r	-0,059335	-0,060874	2,53%	98%	2%
c_n	0,011572	0,036874	68,62%	85%	15%
c_g	0,159932	0,264793	39,60%	100%	0%

pressure coefficients
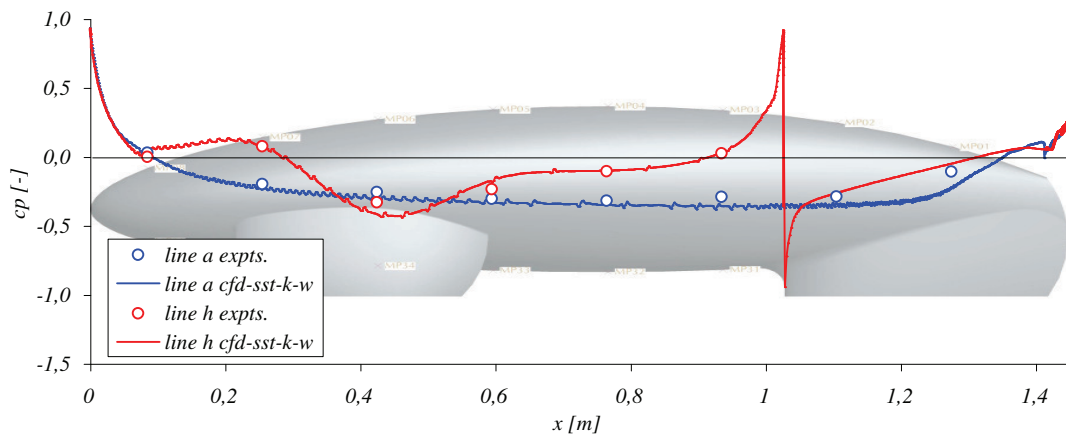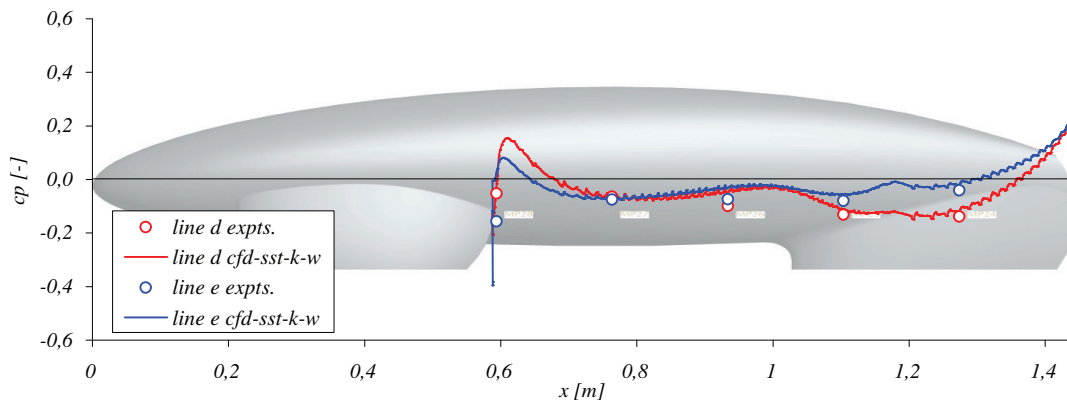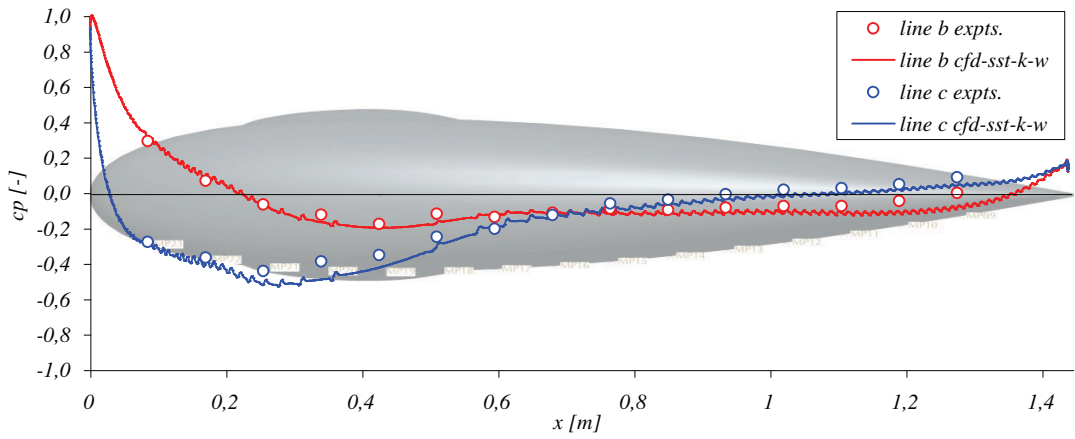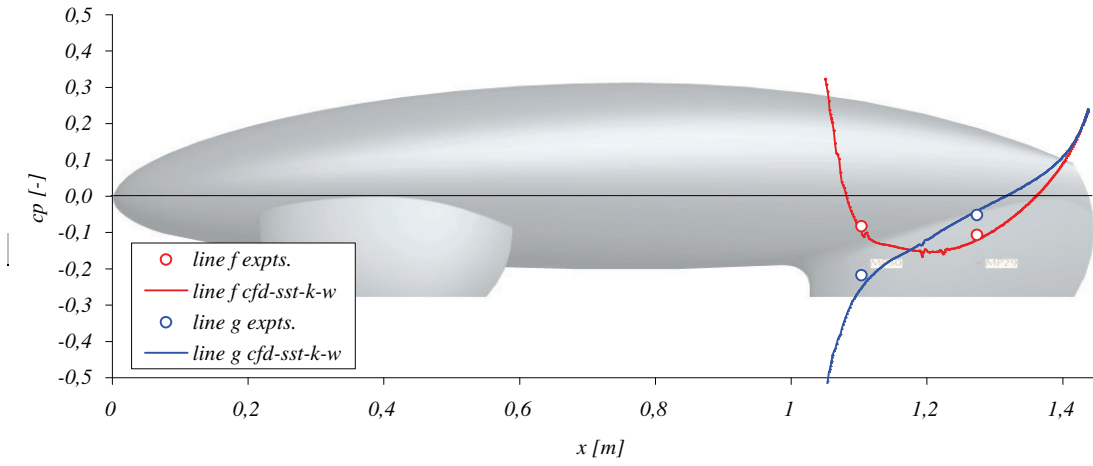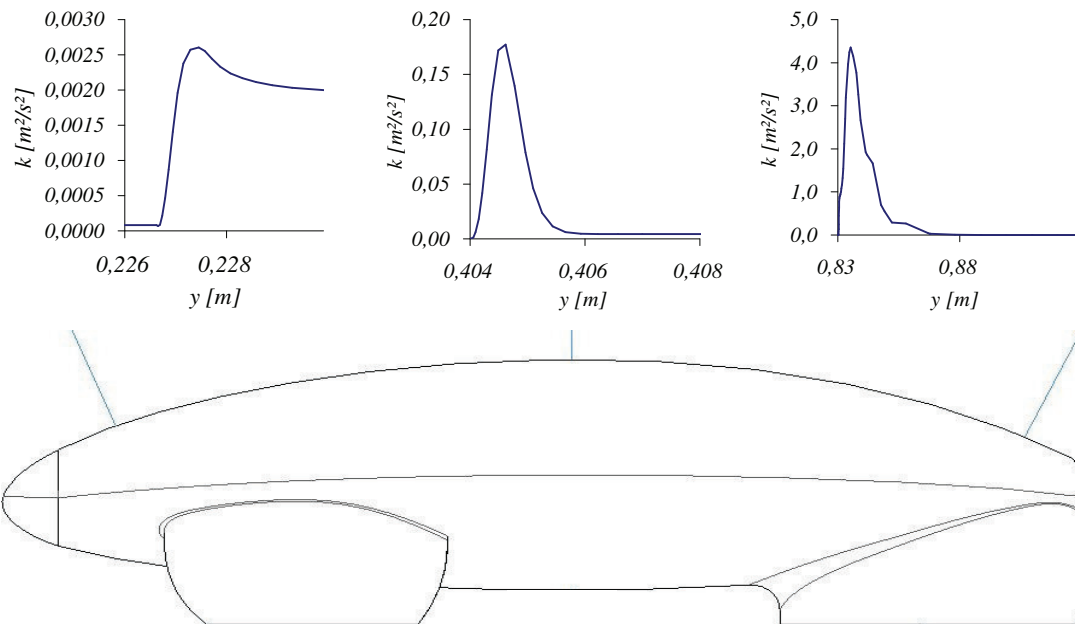
line a and h

line d and e

line b and c

line f and g
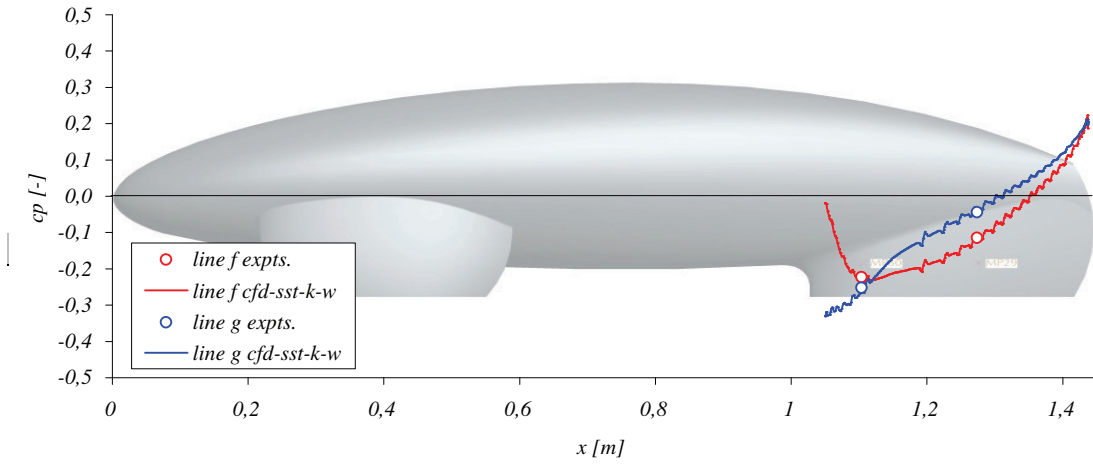
turbulent kinetic energy [m²/s²] in boundary layer on three positions in the symmetry plane

$\alpha = 15° / SST\text{-}k\text{-}\omega$

force and moment coefficients
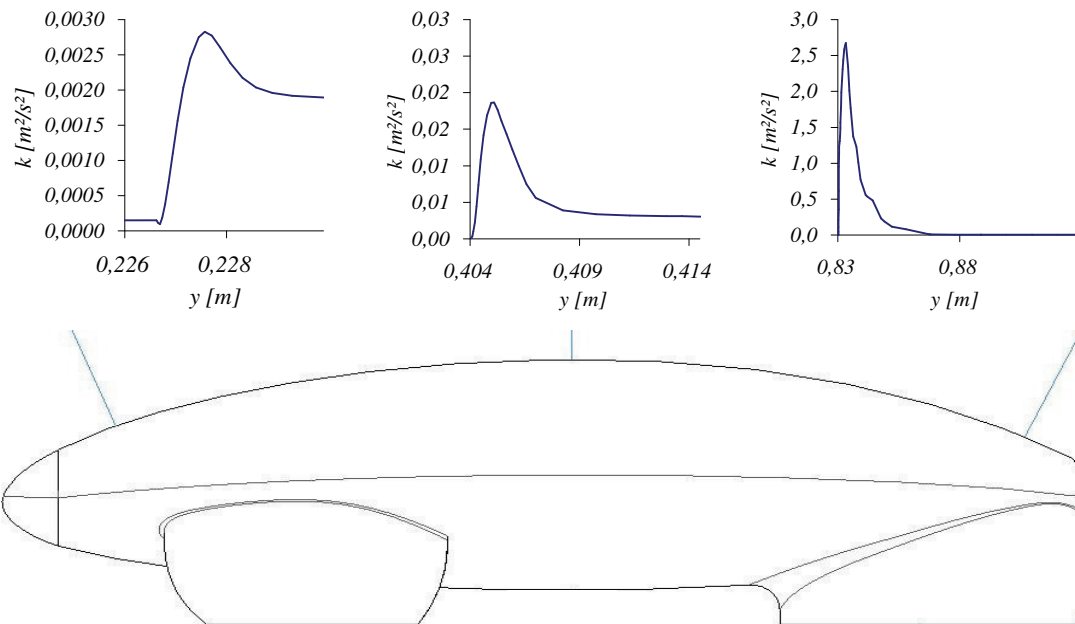
	windtunnel	cfd	tolerance	press. ratio	visc. ratio
c_w	0,143741	0,161080	10,76%	77%	23%
c_a	0,731317	0,441926	-65,48%	99%	1%
c_s	0,918489	0,930342	1,27%	99%	1%
c_r	-0,103191	-0,109914	6,12%	99%	1%
c_n	-0,005951	0,050753	111,73%	90%	10%
c_g	0,185797	0,254144	26,89%	100%	0%

pressure coefficients
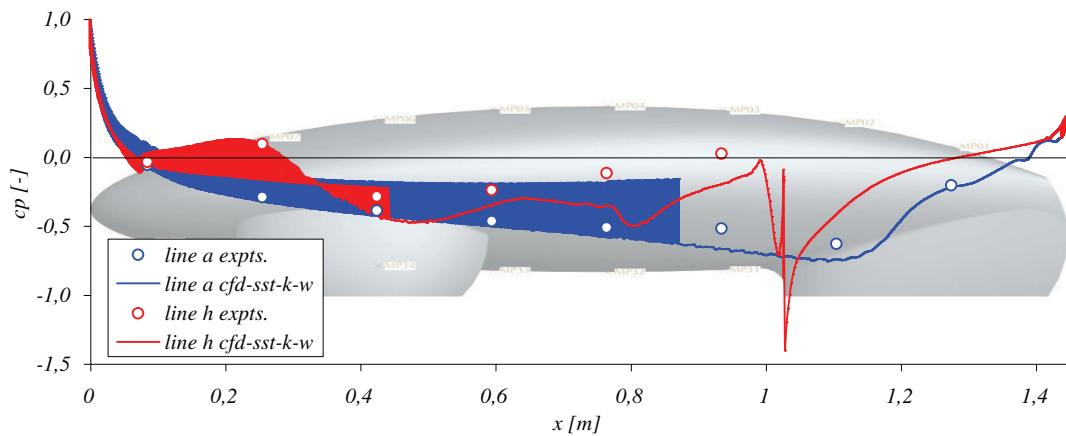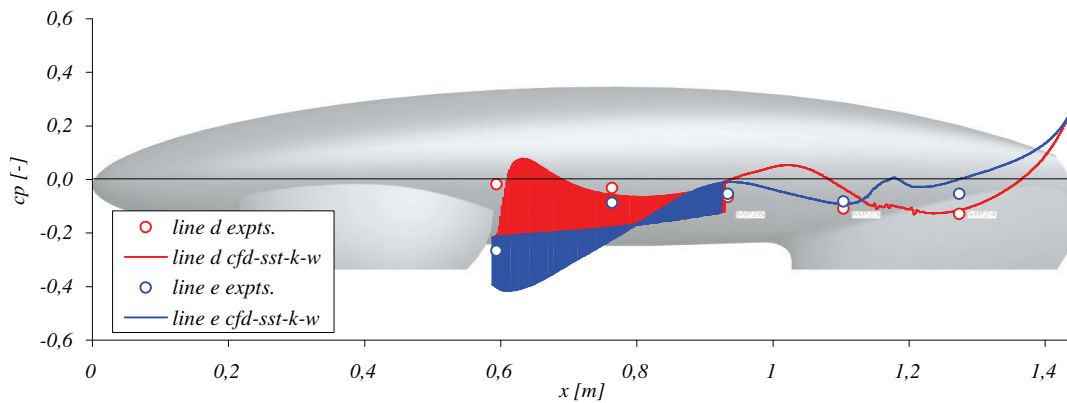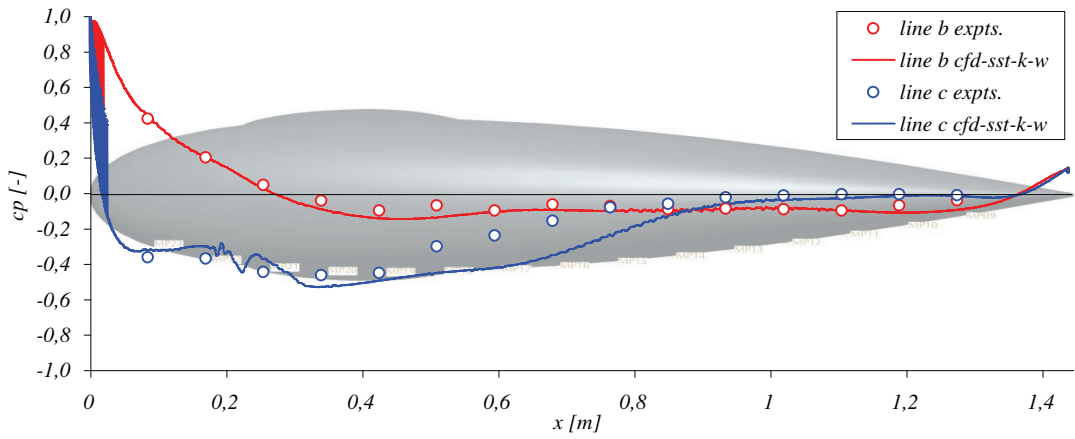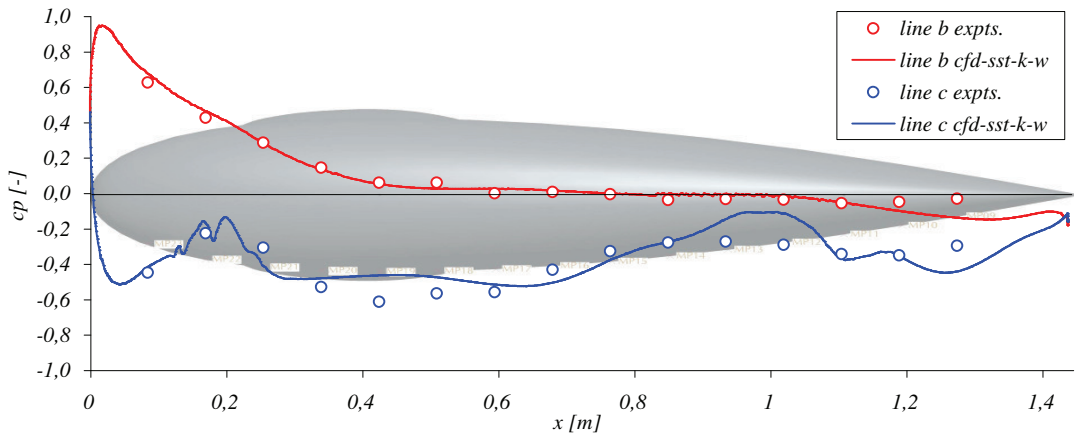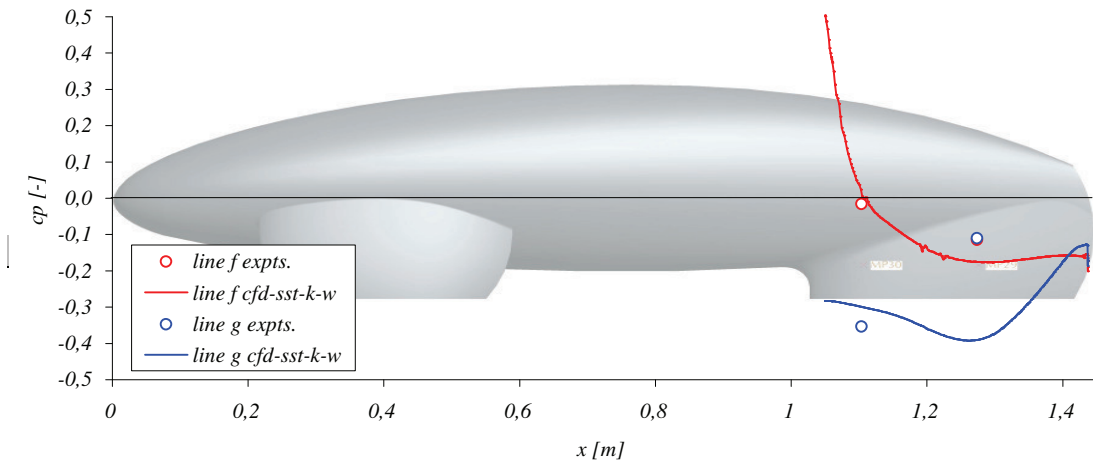
line a and h

line d and e

line b and c

line f and g
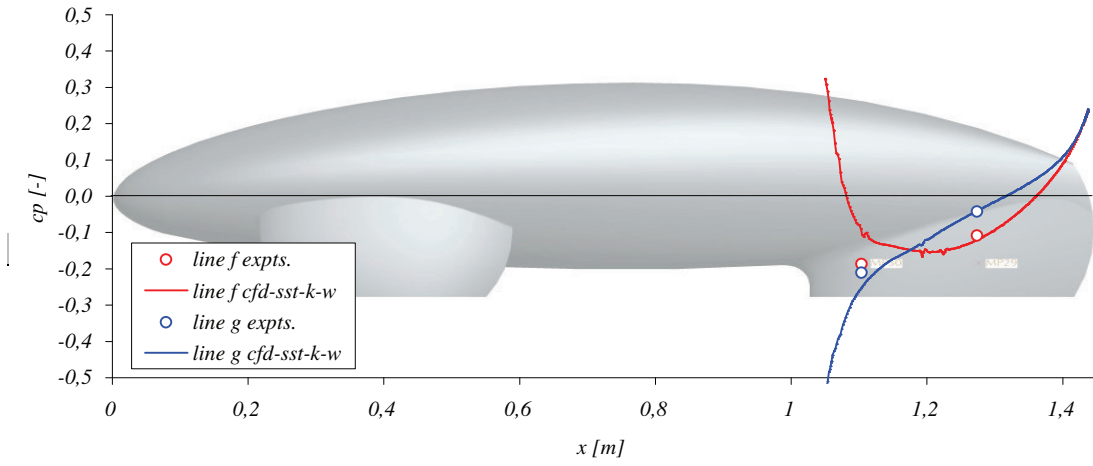
turbulent kinetic energy [m²/s²] in boundary layer on three positions in the symmetry plane

$\alpha = 20° / SST\text{-}k\text{-}\omega$

force and moment coefficients

	windtunnel	cfd	tolerance	press. ratio	visc. ratio
c_w	0,175798	0,161080	-9,14%	77%	23%
c_a	0,931283	0,441926	-110,73%	99%	1%
c_s	1,396853	0,930342	-50,14%	99%	1%
c_r	-0,164363	-0,109914	-49,54%	99%	1%
c_n	-0,014853	0,050753	129,27%	90%	10%
c_g	0,151208	0,254144	40,50%	100%	0%

pressure coefficients

line a and h

line d and e

$\alpha = 25° / SST\text{-}k\text{-}\omega$

force and moment coefficients

	windtunnel	cfd	tolerance	press. ratio	visc. ratio
c_w	0,157680	0,206638	23,69%	82%	18%
c_a	1,062691	0,704742	-50,79%	99%	1%
c_s	1,976147	1,878145	-5,22%	99%	1%
c_r	-0,233839	-0,221033	-5,79%	99%	1%
c_n	-0,010048	0,088174	111,40%	95%	5%
c_g	0,088990	0,297901	70,13%	100%	0%

pressure coefficients
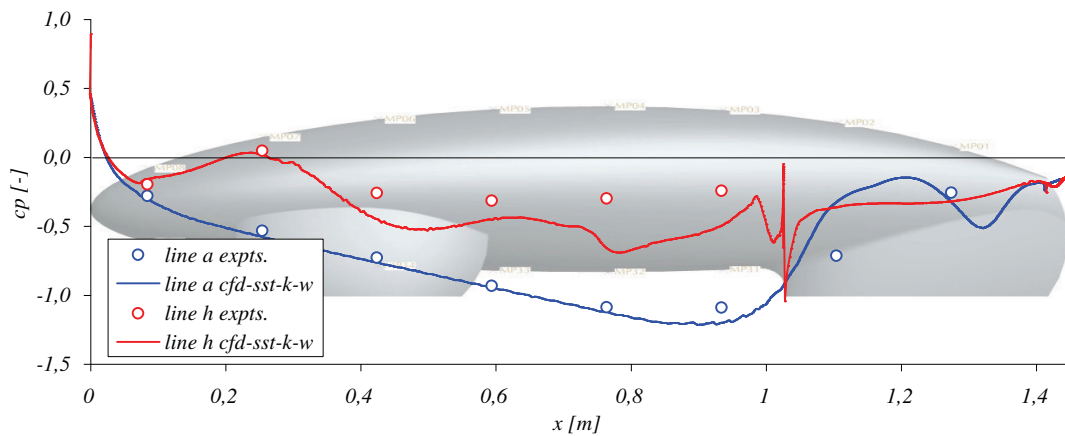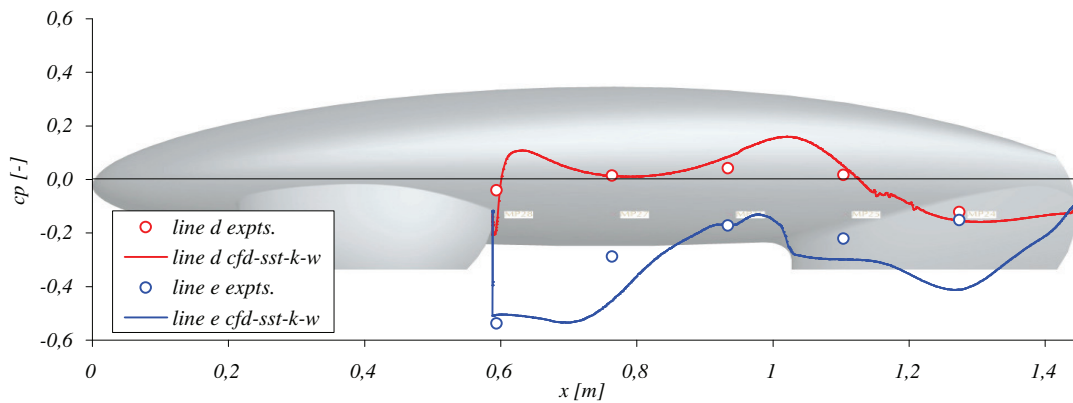
line a and h

line d and e

line b and c

line f and g

turbulent kinetic energy [m²/s²] in boundary layer on three positions in the symmetry plane
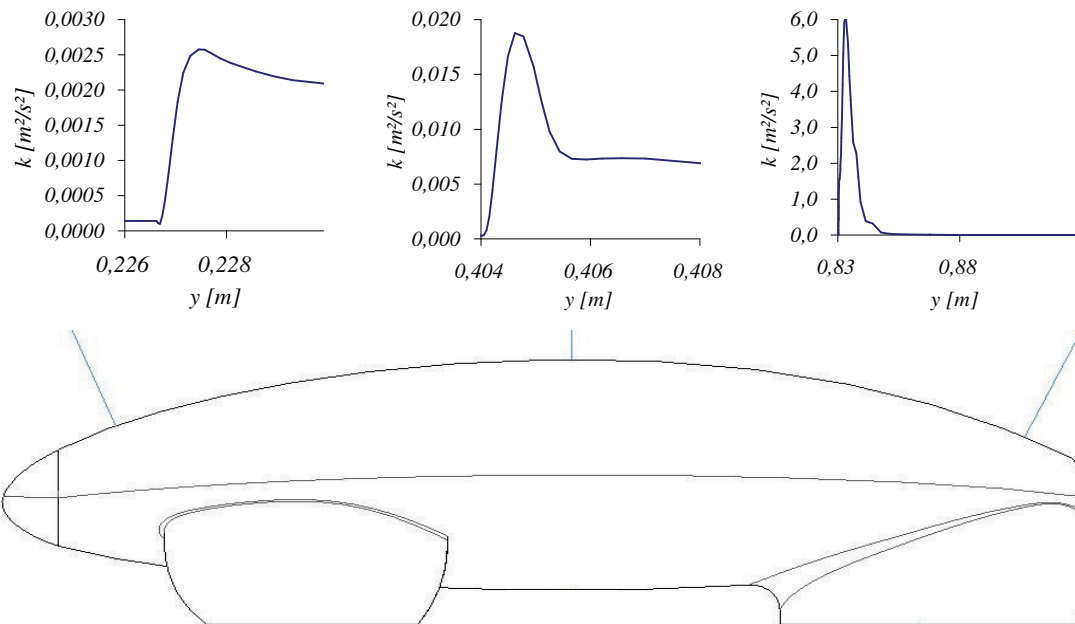
$\alpha = 0° / DES$

input data

date	05.08.2010		
flow angle	0 °		
flow velocity	20 m/s		
turbulence model	DES		
turbulent intensity	0,13 %		
turbulent length scale	0,0086 m		
number of cells	15.735.777 #		
meshname	eco_modell_100531_1.spm		
number of iterations	2.500 #		
time steps	331 a	5,0E-05 s	0,01655 s
Iterations per time step	20 #	6620 Iterations	

force and moment coefficients

	windtunnel	cfd	tolerance	press. ratio	visc. ratio
c_w	0,075830	0,073300	-3,45%	85%	15%
c_a	0,147892	0,136545	-8,31%	99%	1%
c_s	-0,034309	-0,107701	68,14%	100%	0%
c_r	-0,003191	0,013226	124,13%	100%	0%
c_n	0,045107	0,056524	20,20%	95%	5%
c_g	-0,019617	0,006651	394,96%	100%	0%

pressure coefficients

line a and h
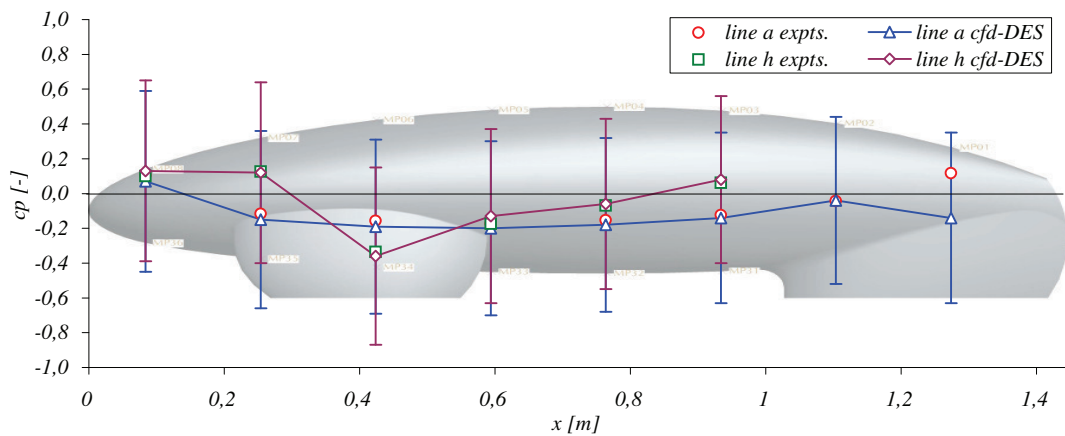
line d and e
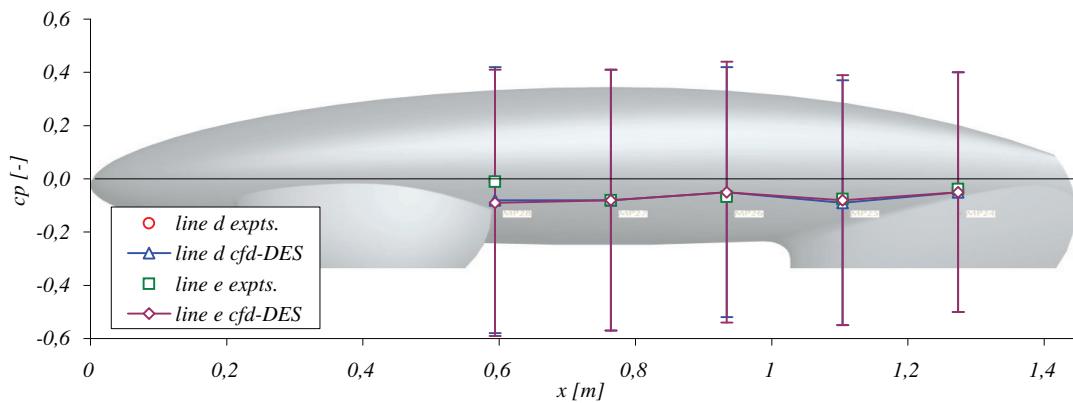
line b and c
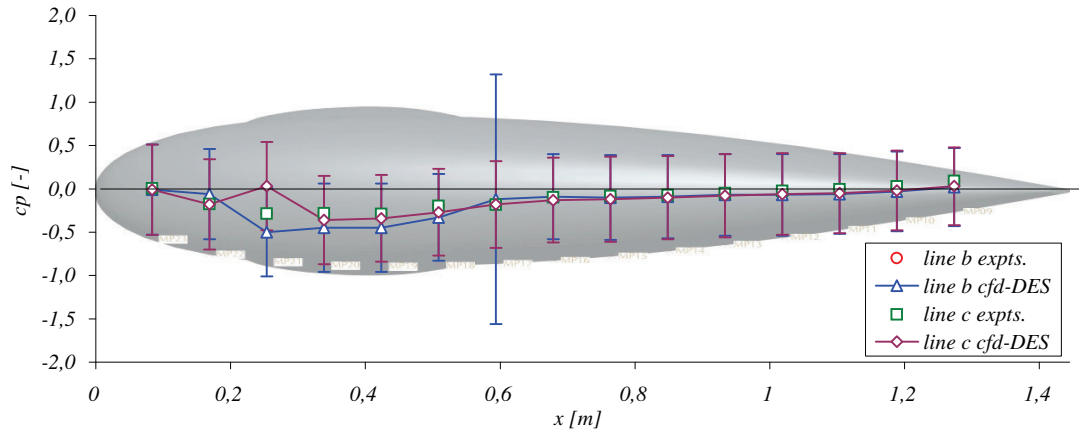
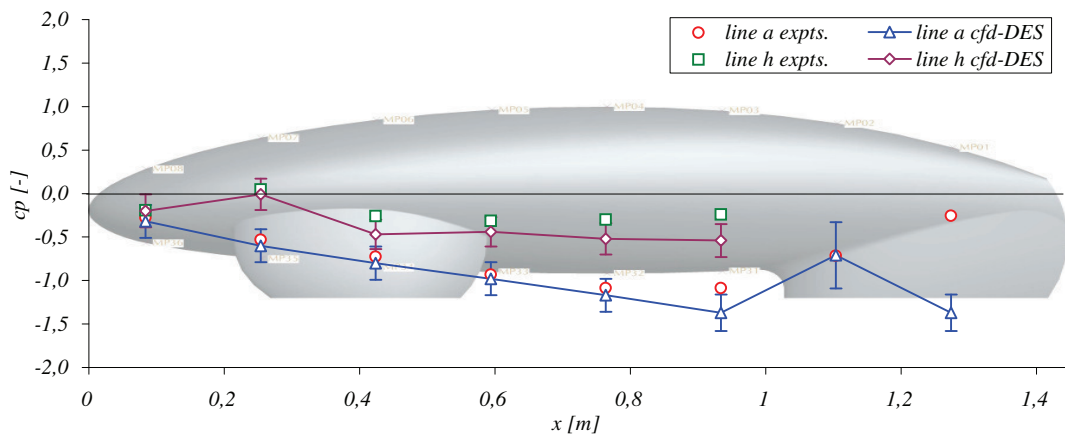line f and g
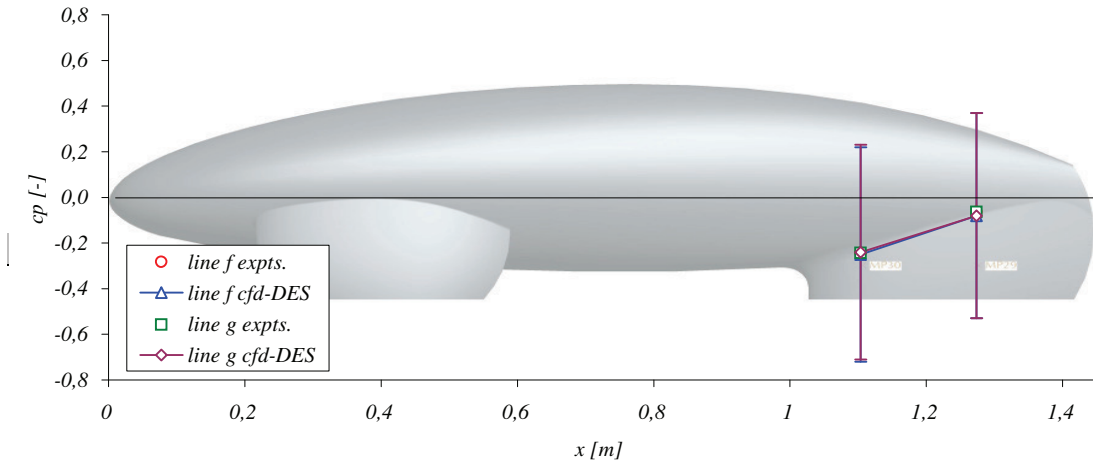
$\alpha = 25° / DES$

input data

date	12.08.2010			
flow angle	25 °			
flow velocity	20 m/s			
turbulence model	DES			
turbulent intensity	0,13 %			
turbulent length scale	0,0086 m			
number of cells	15.735.777 #			
meshname	eco_modell_100531_1.spm			
number of iterations	2.500 #			
time steps	1.300 a	5,0E-06 s		0,0065 s
Iterations per time step	20 #	26000 Iterations		

force and moment coefficients

	windtunnel	cfd	tolerance	press. ratio	visc. ratio
c_w	0,157680	0,115500	-36,52%	68%	32%
c_a	1,062691	0,731900	-45,20%	99%	1%
c_s	1,976147	2,467944	19,93%	99%	1%
c_r	-0,233839	-0,283336	17,47%	99%	1%
c_n	-0,010048	0,078400	112,82%	95%	5%
c_g	0,088990	0,335504	73,48%	100%	0%

pressure coefficients

line a and h

line d and e
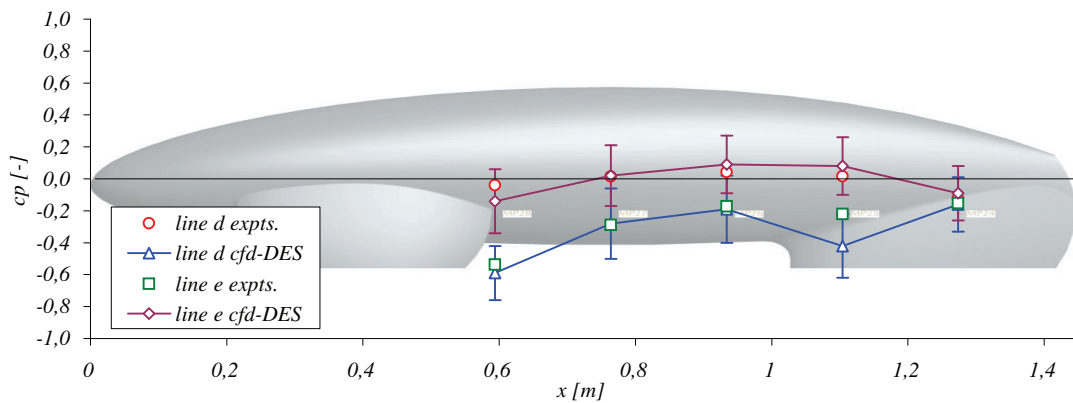
line b and c
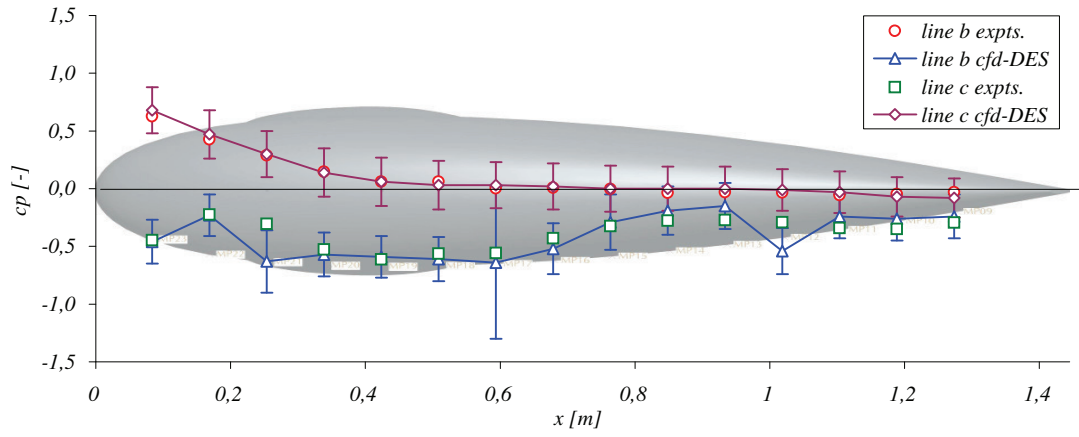
line f and g

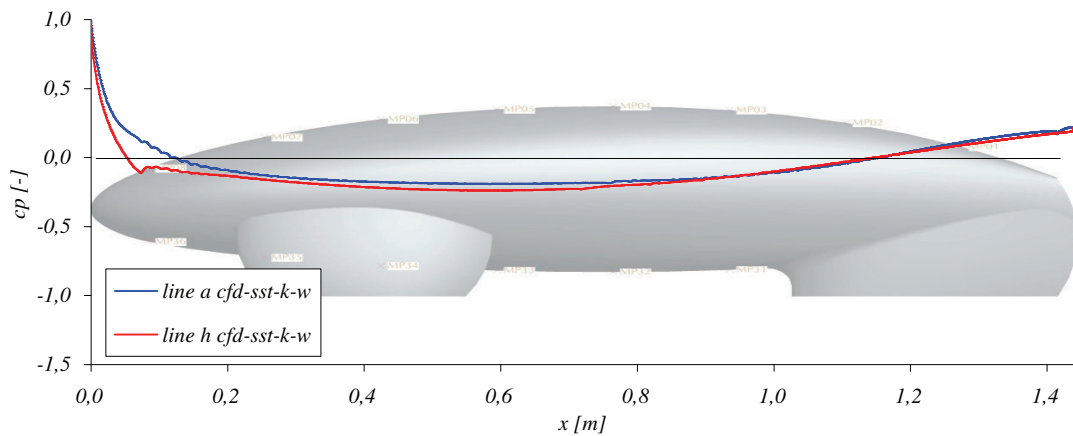# main body $\alpha = 0° / SST\text{-}k\text{-}\omega$

force and moment coefficients

	windtunnel	cfd	tolerance	press. ratio	visc. ratio
c_w	-	0,034784	-	21%	79%
c_a	-	-0,072494	-	100%	0%
c_s	-	-0,000035	-	93%	7%
c_r	-	0,000005	-	100%	0%
c_n	-	-0,019366	-	85%	15%
c_g	-	0,000042	-	98%	2%

pressure coefficients

line a and h

line d and e